First-Principles Study of Defects at the SiC/SiO$_2$ Interface through Hybrid Functionals

Fabien DEVYNCK

Master of Research in Nanomaterials, University of London, Royaume-Uni
et de nationalité française

Resumé

Les exigences actuelles des systèmes électroniques de puissance à haute performance dépassent la densité de puissance, le rendement, et la fiabilité des dispositifs à base de silicium. Le carbure de silicium (SiC) est un candidat de choix pour les applications à haute température, haute vitesse, haute fréquence et haute puissance: il posséde une grande bande interdite et une conductivité thermique, une vitesse de saturation électronique, et un champ électrique de rupture élevés. Le SiC est aussi dur, chimiquement stable et résistant aux dégâts créés par les rayonnements. Malgré ces très bonnes propriétés électroniques, les dispositifs à base de SiC sont encore confrontés à de nombreux défis en raison de la haute densité de défauts à l'interface SiC/SiO_2

Cette thèse est consacrée à l'étude des défauts à l'interface SiC/SiO_2 par le biais de méthodes de fonctionnelles hybrides. Nous avons d'abord généré une structure modèle fournissant une description réaliste de l'interface $4H(0001)$-SiC/SiO_2. La description de la structure électronique au moyen de fonctionnelles hybrides conduit à des valeurs de discontinuités de bande en parfait accord avec les valeurs expérimentales correspondantes. Nous avons ensuite étudié plusieurs défauts du semiconducteur et de l'oxyde par le moyen de fonctionnelles de densité hybrides polarisées en spin. Des défauts contribuant à la haute densité de défauts à l'interface dans la bande interdite du SiC ont été identifiés. Finalement, la possibilité de croissance épitaxiale de couches minces de silicate sur le SiC a été investiguée comme solution alternative afin de réduire grandement la haute densité d'états liée aux défauts à l'interface SiC/SiO_2.

Mots-clés: Carbure de silicium, modèle atomistique, interface, défauts, fonctionnelles hybrides.

Abstract

The requirements of present high-performance power electronic systems are exceeding the power density, efficiency, and reliability of silicon-based devices. Silicon carbide (SiC) is a candidate of choice for high-temperature, high-speed, high-frequency, and high-power applications: it has a wide band gap, high thermal conductivity, high saturated electron drift velocity, and high breakdown electric field. SiC is also hard, chemically stable, and resistant to radiation damage. Despite these desirable electronic properties, SiC-based devices are still facing many performance challenges due to the high density of defect states at the SiC/SiO_2 interface.

This thesis is dedicated to the first-principles study of defects at the SiC/SiO_2 interface through hybrid functionals. We first generate a model structure providing a realistic description of the majority bonding arrangements at the $4H(0001)$-SiC/SiO_2 interface. The description of the electronic structure of the model through hybrid functionals leads to band offsets in excellent agreement with their experimental counterparts. We then study several semiconductor and oxide defects using spin-polarized hybrid density functionals and identify candidate defects responsible for the high density of interface defects measured in the $4H$-SiC band gap. Finally, the possibility of growing epitaxial silicate adlayers on SiC is investigated as an alternative approach to greatly reduce the high density of defect states at the SiC/SiO_2 interface.

Keywords: Silicon carbide, atomistic model, interface, defects, hybrid functionals.

Contents

Chapter 1

Introduction

1.1 History of SiC

Silicon carbide (SiC) is naturally synthesized in the atmospheres of carbon rich red giant stars and by supernova remnants. No natural crystals can be found on Earth and therefore SiC never attracted man's interest as other crystals like diamond did.

Jöns Jacob Berzelius, also known for his discovery of silicon, was most probably the first to synthesize SiC. He published in 1824 a paper in which he assumed there was a chemical bond between silicon and carbon in one of the samples he had produced [1]. But it was not before 1892 that SiC came into focus as a useful material. E. G. Acheson was looking for a suitable material that could substitute expensive diamonds needed for grinding and cutting purposes. He mixed coke and silica in a furnace and found a crystalline product characterized by great hardness, refractability, and infusibility. This product was shown to be a compound of silicon and carbon and was caled "carborundum" [2].

In 1907, H. J. Round produced the first Light Emitting Diode (LED) based on SiC. He reported that "on applying a potential of 10 volts between two points on a crystal of carborundum, the crystal gave out a yellowish light" [3]. In 1912, H. Baumhauer used the word "polytype" to describe the ability of SiC to crystallize into different forms varying only in their stacking order in one direction. The evolution of SiC as an electronic material then took several decades. In 1955, Lely presented a new method to grow high quality SiC crystals. This triggered the development of SiC as a semiconductor material and SiC became even more popular than Si and Ge. However, the difficulty in obtaining high-purity SiC wafers and the rapid success of the Si technology caused a drop in the interest in SiC. In

1978, Tairov and Tsvetkov then managed to produce high purity SiC substrates by seeded sublimation growth [4]. The first SiC wafer had been made. Another major step forward was made in 1983 when Nishino, Powell, and Hill realized the first heteroepitaxy of SiC on Si [5]. In 1987, this technique was further improved and the next stage of SiC evolution started when high-quality heteroepitaxy was performed at low temperatures on off-axis substrates using "step-controlled epitaxy" [6]. Cree Inc. was founded the same year and two years later, the company introduces the world's first blue LED and began to sell SiC wafers. Along with better epitaxy, the improvement of the diameter and quality of the wafers continued until the production of 4 inch SiC single crystals was reached in 1999. SiC Schottky diodes and high-frequency MESFETs (MEtal Semiconductor Field Effect Transistor) are now commercially produced but research on electronic SiC-based devices is still active in view of many possible applications.

1.2   Applications of electronic SiC-based devices

The requirements of present high-performance power electronic systems are exceeding the power density, efficiency, and reliability of silicon-based devices. Conventional silicon devices require heavy and bulky heat sinks to reach their operational temperature limits at approximatively 350 °C, are highly susceptible to harsh environments such as intense radiations, and have a switching limit in the range of a few gigahertz (GHz). On the other hand, SiC devices could operate at temperatures up to 600 °C, at switching frequencies in the 10-100 GHz range and at increased power densities. These lighter, more compact high density power devices operating in harsh environments or at high temperatures would meet the requirements spanning many areas of both the military and civilian sectors.

While very few SiC devices are currently commercially available, the field of *power electronics* attracts a lot of interest. For example, high-power converters and motor drives able to operate in harsh environments are key components in the U.S. military project of developing hybrid-electric armed robotic vehicles. NASA is also interested in SiC power converters for spacecraft and satellite applications to increase the payload capability in lightweight solar arrays. These SiC power converters would increase the operational temperature range while reducing the required but heavy and bulky heat exchangers. Energy companies and geological exploration instrumentation would also benefit from SiC improved motor drives and sensors' capabilities in deep earth drilling where hostile environ-

ments and extreme temperatures make the use of silicon electronics impossible.

Another area where SiC superior properties are desirable is *high-frequency electronics.* Most micro-wave communications and radar electronics systems currently use GaAs devices offering superior performance over silicon. However, fast-switching capability coupled with high power density and high operating temperature make SiC high-frequency devices ideal for military aircraft requiring lightweight high-performance electronic radar systems. Commercial communications industries such as air traffic control, weather radar stations and cell phone base stations, would also benefit from higher performance radio-frequency SiC devices.

Integrated circuits is yet another field where SiC is expected to play a major role. Nowadays, for example, sensor and control electronics used in conjunction with jet or rocket engines must be removed from the target area, carefully shielded, protected and cooled. SiC devices would offer for instance the possibility to mount electronic controls directly on or into a jet engine, therefore increasing reliability and performance while reducing complexity, costs, and weight. Landing long-term, fully operational probes in hostile high-temperature environments is another attractive aspect for space exploration.

Apart from these cutting-edge niche markets, domestic applications would also benefit from SiC devices' ability to work in harsch, high-temperature environments. In the computer industry, thermal issues are the main concerns when transferring technology from the desktop system to the laptop. With transistor junctions operating at 600 °C instead of 80 °C in the case of current commercial electronics, these issues would be greatly reduced. All the achievements in developing SiC technology in the case of military hybrid-electric combat vehicles could be directly applicable to domestic vehicles. And SiC devices would also allow sensor and control electronics to be mounted onboard directly on the engine block of automobiles without being shielded or kept away from the engine compartment because of thermal issues. All these possible applications rely on the superior physical properties of SiC.

1.3 Physical properties of SiC

SiC is the only known binary compound of silicon and carbon and possesses a one-dimensional polymorphism called polytypism. In a polytypic compound, similar sheets of atoms or symmetrical variants are stacked on top of each other.
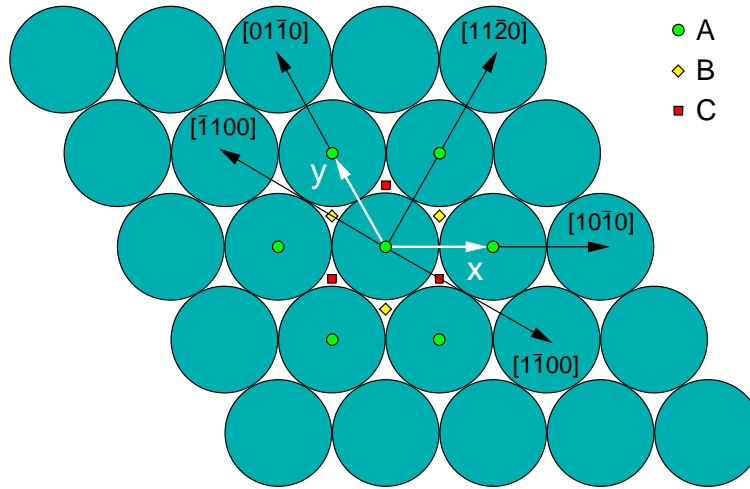
Figure 1.1:   A close-packed hexagonal plane of spheres centered on points A. A second identical plane can be placed on top of the first one, with the centers of spheres over either points B or C.

The differences between the polytypes arise only in the direction perpendicular to the sheets. In SiC, each sheet represents a bilayer of C atoms right atop Si atoms. The sheets can be represented as a close-packed array of Si-C units forming a two-dimensional pattern with sixfold symmetry. Using the notations for hexagonal crystal structures, the first sheet can be defined as the basal c-plane with Miller-indexed directions according to Fig. 1.1.

There are then two possibilities for arranging the second sheet on top of the first one in a close-packed configuration. The second sheet can be displaced along, for example, direction $[\bar{1}100]$ until the spheres lie on positions B or along, for example, direction $[1\bar{1}00]$ until the spheres lie on positions C. If a sheet is denoted A, B, C depending on the positions of its spheres, all polytypes can then
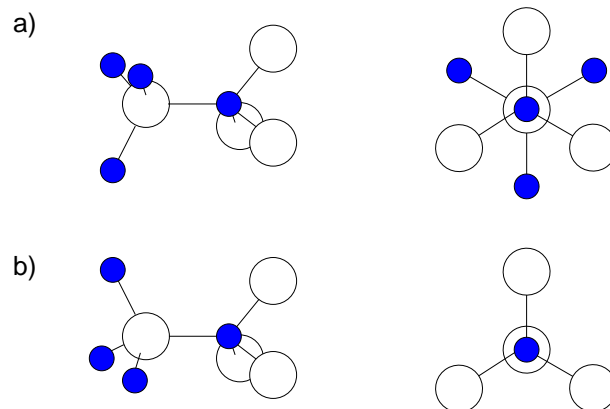
Figure 1.2:   Side view and view along the stacking direction for (a) the cubic ("k") type of bond where the bonds are rotated and (b) the hexagonal ("h") type where the bonds are aligned.
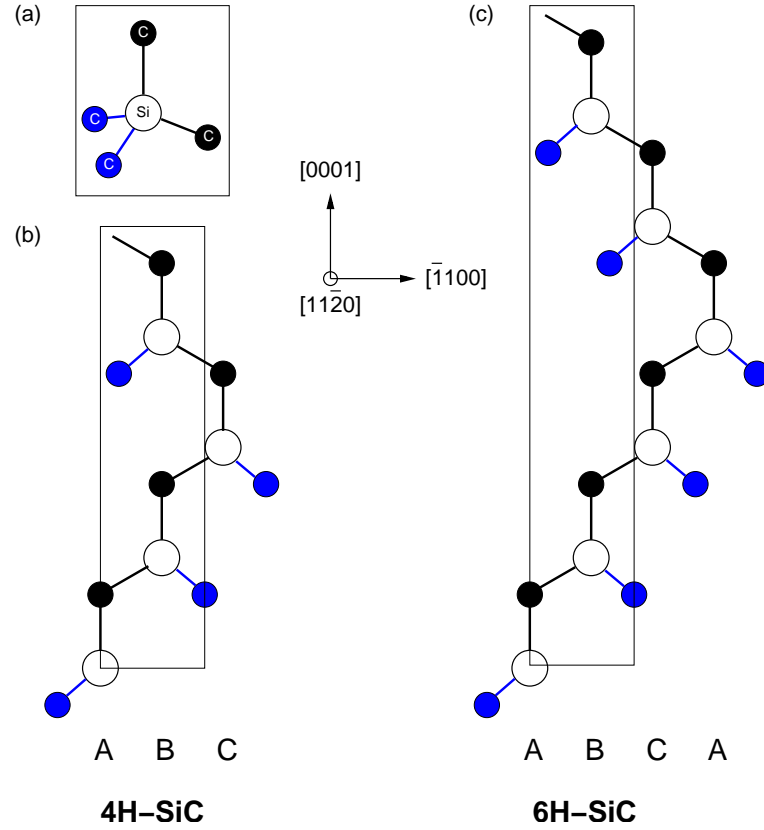
Figure 1.3: (a) The basic structural unit in SiC is a tetrahedron of four carbon atoms with a silicon atom in the middle. Stacking sequence of bilayers of Si and C atoms of (b) $4H$- and (c) $6H$-SiC. The blue disks are the projections of the blue C atoms in (a) and are shown to indicate the orientations of the tetrahedra. The projection of the unit cell on the $(11\bar{2}0)$ is also shown.

be described as different stackings of A, B, C sheets with the restriction that sheets with the same rotation cannot be stacked upon each other.

In the SiC polytypes, the basic structural unit consists of a primarily covalently bonded tetrahedron of four C (or Si) atoms with a Si (C) atom at the center. The bond length between the Si-C atoms is approximately 1.89 Å whereas the distance between the Si-Si or C-C atoms is approximately 3.08 Å. These tetrahedra join to each other at the corners to form the SiC crystals. The tetrahedra have threefold symmetry around the axis parallel to the stacking direction. A tetrahedra stacked upon a first one can then either have the same orientation (and be called "untwinned tetrahedra") or be rotated 180° around the stacking direction ("twinned tetrahedra"). This local arrangement defines a bilayer environment that can be either hexagonal (h) or cubic (k, from the german "kubisch") [7] depending on the surrounding bilayers (Cf. Fig. 1.2).

More than 250 SiC polytypes have been identified [8], with some having stack-

Table 1.1:   Main physical and electronic properties of bulk $4H$-SiC, $6H$-SiC and Si. The bulk moduli for $4H$-SiC and $6H$-SiC result from different ab-initio calculations and lead to a range of predicted values) [10, 11, 12].

	$4H$-SiC	$6H$-SiC	Si
Bulk modulus (GPa)	217-224	204-260	98
Thermal conductivity (W·cm^{-1}·K^{-1})	4.9	4.9	1.3
Band gap (eV)	3.26	3.02	1.12
Saturated electron drift velocity (10^7 cm·s^{-1})	2.0	2.0	1.4
Breakdown electric field (10^5 V·cm^{-1})	22	25	3

ing sequences of several hundreds of bilayers. The crystal structures of SiC can be cubic, hexagonal or rhombohedral. In this thesis, we focus on the two polytypes particularly suited for electronics, namely $4H$- and $6H$-SiC. These two polytypes are named according to Ramsdell's notation [9] where the number stands for the periodicity in the stacking direction (i.e. the number of letters A, B, C needed to define the unit cell) and the letter relates to the crystal structure, here H for hexagonal. Following the ABC notation, $4H$-SiC has a stacking sequence labeled ABCB and ABCACB for $6H$-SiC (Fig. 1.3). According to the notations for hexagonal crystal structures, the lattice parameter a along the [10$\bar{1}$0] is 3.08 Å for both $4H$-SiC and $6H$-SiC and c along [0001] is 10.06 Å and 15.11 Å for $4H$-SiC and $6H$-SiC, respectively (cf Ref. [10] for more details on structural parameters).

These two hexagonal polytypes share many desirable mechanical, thermal, and electronic properties. Table 1.1 compares these quantities of primary importance in electronics to those of conventional silicon and highlights why SiC is a candidate of choice for high-temperature, high-speed, high-frequency, and high-power applications: it has a wide band gap, high thermal conductivity, high saturated electron drift velocity, and high breakdown electric field. SiC is also hard, chemically stable, and resistant to radiation damage. For industrial purposes, SiC can be n-type doped using nitrogen or phosphorus as donors and p-type doped using boron, aluminium or gallium as acceptors.

Despite these desirable bulk properties, SiC-based devices are still facing many performance challenges.

1.4   The SiC/SiO$_2$ interface: recent progress and challenges

Among many polytypes of SiC, $4H$-SiC has been recognized as the most suitable for technological applications because of its wider band gap and higher bulk electron mobility [13]. Recently, a new method to produce ultrahigh-quality silicon carbide single crystals has been reported [14]. These virtually dislocation-free substrates were predicted to promote the development of high-power SiC devices and reduce energy losses of the resulting electrical systems. Since SiC shares SiO$_2$ as native oxide with Si, SiC-based power MOSFETs were expected to have great potential for high-speed and low-loss switching devices. However, low inversion-channel mobilities [15, 16, 17, 18, 19] have been reported for MOSFETS fabricated on (0001) Si-face $4H$-SiC substrates, despite their high bulk mobility. These low mobilities lead to much higher on-state resistances in $4H$-SiC MOSFETs [20, 21] than expected from bulk material properties. These poor electrical properties have been attributed to the large density of interface states (D_{it}) at the SiC/SiO$_2$ interface resulting in charge trapping and Coulomb scattering [22]. Whereas the D_{it} at the Si/SiO$_2$ interface is nowadays less than 10^{10} cm^{-2} eV^{-1}, it reaches $\sim 10^{11}$ cm^{-2} eV^{-1} in the middle of the band gap and $\sim 10^{13}$ cm^{-2} eV^{-1} or more at the band edges in $4H$-SiC [23].

1.4.1   Distribution of the defect state density

Through many studies of different goups, four main peaks or shoulders of D_{it} have been identified [23, 24, 25, 26, 27]. It should be noted that the positions of some of these interface states may slightly vary depending on the growth method, the applied measurement method, and the polytype under study. However, these differences remain small and all measurements generally agree with the picture given in Ref. [23]. A sketch based on measurements of D_{it} by admittance spectroscopy and constant capacitance deep level transient spectroscopy (DLTS) in n- and p-type $4H$-SiC/SiO$_2$ MOS devices [23] is presented in Fig. 1.4.

    Other different types of experiments also identify these features of the D_{it}. Internal photoemission (IPE) measurements carried out on $3C$-, $4H$-, $6H$- and $15R$-SiC confirm the occurence of interface states in the energy range up to 1.5 eV above the top of the valence band in all the investigated polytypes [28]. The peaks and shoulders D$_2$ and D$_4$ have also been observed by x-ray photoelectron
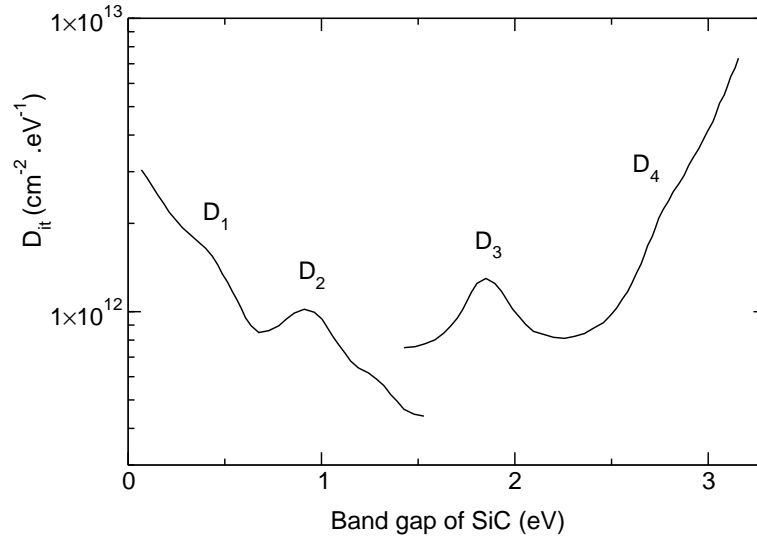
Figure 1.4:   Schematic overview based on experimental measurements of the D_{it} at the $4H$-SiC/SiO$_2$ interface (adapted from Ref. [23]).

spectroscopy (XPS) on $6H$-SiC/SiO$_2$ [26] and by the capacitance-voltage (C-V) technique on $4H$-SiC/SiO$_2$ [24, 25]. X-ray photoemission (XPS) studies on MOS devices under bias also revealed a peak of acceptor peak coinciding with D$_3$ [26] and photon stimulated tunnelling (PST) of electrons shows shallow electron traps just below the conduction band of $4H$-SiC [29, 30].

1.4.2   Identification of the defect states

The interface traps have been classified into fast and slow states. The fast states are in the lower part of the SiC band gap and should have their origin in the interface layer while the slow states near the SiC conduction band should be located in the oxide [23].   But the nature of the individual parts of the D_{it} is not clearly established.   Still, two main classes of potential defects emerge from the literature: *(i)* electrically active carbon clusters at the SiC/SiO$_2$ interface or interfacial defects formed in a transition region near the SiC/SiO$_2$ interface [31, 32, 33, 34, 35] and *(ii)* intrinsic defects in SiO$_2$ [28, 29, 30, 36, 37]. We show in Fig. 1.5 a schematic energy distribution of interface states from Ref. [23] illustrating C-related and intrinsic oxide defects believed to be responsible for most of the D_{it} [23, 38].
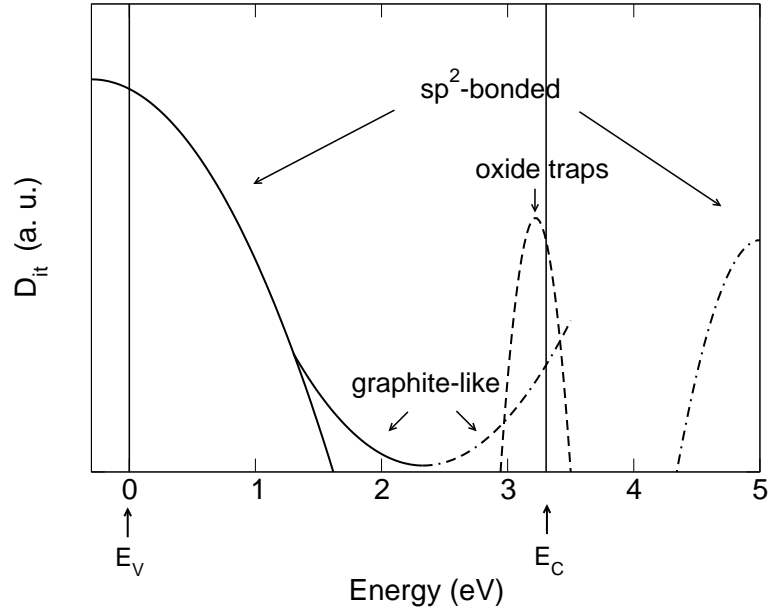
Figure 1.5: Schematic energy distribution of interface states originating from wide energy gap carbon clusters, graphite-like carbon clusters, and near-interfacial oxide defects. The zero point of the energy scale is placed at the bottom of the $4H$-SiC valence band; the arrows indicate the valence and conduction band edges of $4H$-SiC (adapted from Ref. [23]).

Carbon-related defects

During thermal oxidation of silicon carbide most of the excess carbon is believed to be removed from the interface through the formation and diffusion of CO molecules in the oxide. However, some of the carbon can remain in the oxide and form carbon clusters or graphitic regions. Carbon bonds as observed in amorphous carbon were therefore proposed to be responsible for the dominant part of interface states [23]. Atomic force microscopy experiments lend support to this interpretation revealing platelet-shaped inhomogeneities, which were assigned to carbon clusters [39]. However, several subsequent studies have questioned the occurrence of such clusters [40, 41, 42, 43, 44, 45]. Subsequently, surface sensitized Raman spectroscopy (SERS) measurements claimed the presence of nano-graphitic structures at the interface [46]. A deconvolution of the carbon-related signal on the oxidized C-face revealed the presence of ideal nano-graphitic flakes and polyenes on one hand, and of disordered or defective planar graphite structures on the other hand. The size of the graphitic structures was estimated to be ≤2 nm. A peak attributed to ideal nano-graphitic flakes was also detected on the Si-face of oxidized-SiC (with an intensity lowered by an order of magnitude compared to the C-face) but no defective two-dimensional graphite structures

could be identified. Considering the substantially greater interface state density for the C-face than for the Si-face on as-oxidized samples [41, 47], the authors suggested that graphitic flakes could account for this difference. However, Ref. [48] indicates that in the case of graphitic structures with a size less than 2 nm, defective two-dimensional graphite structures should be more present than ideal graphitic flakes, as opposed to measurements in Ref. [46]. X-ray photoelectron spectroscopy (XPS) also detected graphitic regions at the SiC surface prior to oxidation but these regions dissolved during *in situ* oxidation and no graphite could finally be found at the SiC/SiO$_2$ interface [49, 50]. Recent high resolution electron microscopy (HREM) and energy filtered transmission electron microscopy (EFTEM) on re-oxidized samples did not find any indication of graphitic regions at or near the SiC/SiO$_2$ interface or in the bulk silicon dioxide within a detection limit of 7 Å. In addition, no amorphous carbon accumulation was detected near the SiC/SiO$_2$ interface [51]. Similar EELS and EFTEM studies confirmed that enhanced C/Si ratios (by up to 35%) at certain spots on the interface of as-oxidized samples were reduced considerably with reoxidation [52]. It was also found that annealing in NO removed the carbon excess completely [53]. Further insight in the nature of the interface defects comes from electron spin resonance experiments on oxidized porous SiC [54, 55]. Carbon dangling bonds were identified [54] and their successful passivation by H$_2$ demonstrated [55]. This indicates that the interface defect states at SiC/SiO$_2$ do not result from carbon dangling bonds. Recent density-functional calculations provided insight on the nature of typical defects occurring at the SiC/SiO$_2$ interface. Knaup *et al.* studied the oxidation mechanism of 4H-SiC and typical defects occurring on the semiconductor side of the interface [35]. While the identified defects closely correspond to the D_{it} in the lower part of the SiC band gap, the defects responsible for the high D_{it} close to the conduction band remained unexplained. In a subsequent work, Knaup *et al.* then considered both intrinsic and C-related defects on the oxide side of the interface [34]. In particular, these authors identified Si interstitials and doubly bonded C=C dimers as possible defects in the oxide on the basis of their energy levels in the SiC band gap. Supporting this idea, XPS measurements on 4H-SiC surfaces prior to nitridation identified oxide-carbon bonds [32]. However, these defects could not fully account for the photon stimulated tunneling measurements indicating similar defect concentrations at Si/SiO$_2$ and SiC/SiO$_2$ interfaces [29, 30]. Very recently, Wang *et al.* therefore reconsidered possible origins of the high D_{it} in the SiC band gap [56]. Correlated C dangling bonds were

proposed as the primary cause for the observed D_{it}, their passivation by H_2 being hindered because of their opposed orientations [56].

Oxide defects

Intrinsic defects in SiO_2 [28, 29, 30, 36, 37] have been proposed to account for the D_{it} in the upper band gap. Using photon stimulated tunneling, Afanas'ev *et al.* found that the high D_{it} occurring near the SiC conduction band edge originates from oxide defects located close to the interface and suggested that these defects are responsible for the observed mobility degradation [29, 30]. These so-called near-interface traps (NITs) appeared to be fixed with respect to the conduction band of SiO_2, independent of the polytype and orientation of the SiC and, to a certain extent, of the oxidation conditions [51, 57, 58]. PST measurements on SiC-based MOS structures revealed a mean energy barrier of 2.8 eV, indicating that these negatively charged NIT levels are positionned 0.1 eV below the conduction band of $4H$-SiC. Similar experiments on Si-based MOS structures found NITs at the same energy level with respect to the conduction band of SiO_2 and with a density comparable to that found in the case of SiC. This gave further support to the attribution of these traps to defects of the oxide, probably related to (H-complexed) oxygen vacancy [28, 36]. Using constant capacitance DLTS it has been demonstrated that the electron capture cross sections of these interface traps are small and vary over several orders of magnitude, suggesting that a large portion of the traps is located not at the interface but at some distance into the oxide [33].

Treatments for defects removal

Numerous treatments have been applied to SiC/SiO₂ interfaces in order to improve their quality, with different outcomes and suggestions regarding the origin of the D_{it}. Reoxidation – a post-oxidation heat treatment in oxygen below oxidation temperature – was shown to have a double-fold effect: a significant decrease in the D_{it} in the lower half of the band gap but also a slight increase in the D_{it} in the upper part of the band gap [24]. In contrast with Si/SiO₂ interfaces, annealing in H_2 up to 400° C does not lead to any appreciable passivation of these interface defects, suggesting that dangling bonds give an insignificant contribution to the D_{it} [23, 59]. However, partial passivation of interface states could be achieved by nitridation, either by post oxidation annealing [24, 31, 32, 60, 61, 63]

or by oxidation in a gas mixture containing nitrogen [37, 64, 65]. NO has proven to be the most effective nitrogen precursor; because of safety reason N_2O is more often used, but its effectiveness is also attributed to its dissociation into NO. As NO itself can dissociate, atomic oxygen was also proposed to have an effect on the interface state density reduction. Oxidation in an ozone gas ambient containing O_3 molecules thermally dissociating into atomic oxygen led indeed to a significant reduction in the D_{it}. Atomic nitrogen was also shown to be effective in the form of a nitridation radical irradiation [66] or by nitrogen implantation prior to oxidation [67]. Recently, it was shown that a post oxidation anneal in nitric oxide followed by a post metallization anneal in hydrogen through a platinum gate known to catalyze atomic hydrogen formation resulted in a reduction of the trap density by over an order of magnitude near the conduction band [68, 69]. It was suggested that this treatment could eliminate either by hydrogen passivation or replacement by nitrogen the threefold coordinated atoms responsible for the high interface trap density [69, 70]. XPS investigations also proposed that nitrogen could dissolve carbon clusters and help the removal of carbon from the interface [53, 62]. Nitrogen could also saturate Si dangling bonds and replace oxygen in strained Si-O-Si bonds [62]. Overall, nitridation seemed to affect both the D_{it} in the lower and upper part of the band gap, with a more effective reduction of the latter [37]. Recently, oxidation in an alumina environment instead of conventional quartz was shown to enhance the mobility of the grown interfaces even further than nitridation [71]. It was first proposed that metallic impurities introduced during the growth in the alumina environment were responsible for this effect [72]; however, it was then demonstrated that the reduction of the NITs was correlated with enhanced oxide growth [73] due to sodium originating from sintered alumina [74]. However, the gate oxide of these devices contains metal impurities causing adverse effects, such as high threshold voltage shifts [73] and sensitivity to bias temperature stress [75].

Summary

To summarize, carbon-related structures at the interface are generally considered to be at the origin of the defect states in the lower and mid part of the band gap (D_{1-3} in Fig. 1.5). Reoxidation, nitridation, post oxidation treatments by atomic oxygen or hydrogen are found to be effective in reducing the density of these

states. The presence of large carbon clusters at the interface could not be firmly established, thereby questionning their possible contribution to the D_{it} near the band edges as proposed in Ref. [23]. But carbon-only structures may not fully account for the D_{it} in the lower and mid part of the band gap, and Si-O-C [49, 76] and Si-Si bonds [77], as well as vacancies surrounded by oxygen [78] could be present in the interfacial layer, as revealed by XPS [76, 77].

Less is known about the NITs responsible for the detrimental D_{it} in the upper part of the band gap. Reoxidation is known to increase them even further. Nitridation reduces them more effectively than the deep states, suggesting that they do not originate from carbon-related defects generally associated with the deep states. Indeed, the NITs are believed to be acceptor defects intrinsic to the oxide, which is supported by their detection in Si/SiO₂ systems. Level positions of oxygen defects are characterized by a wide distribution of formation energies and structural configurations [79], suggesting theyc could contribute to the broad bump D_4 in the upper band gap rather than the sharp peak detected by TDRC. Also, the occurence of C atoms or complexes in the oxide can not be excluded [51, 70] and seem to correlate with electron trapping in the oxide [40]. Therefore, it is fair to assume that more than one type of oxide defect may contribute to the NIT.

1.4.3   The epitaxial approach for abrupt SiC/SiO₂ interfaces

As seen so far and despite the variety of applied pre- and post-oxidation treatments, the density of interface states at SiC/SiO₂ interfaces has remained 1 to 2 orders of magnitude larger than at Si/SiO₂ interfaces, preventing the development of SiC-based MOSFETs [23, 37, 56, 59, 60, 80]. To circumvent this problem, experimental research has also explored an alternative approach consisting in the formation of epitaxial silicate adlayers on SiC [81, 82]. Bernhardt *et al.* have been the first to report the formation of an epitaxial silicate adlayer on hexagonal SiC(0001) surfaces prepared by hydrogen plasma or etching in hydrogen flow [81]. This epitaxial adlayer has an atomically abrupt SiC/silicate interface and is expected to be an ideal seed for the epitaxial growth of SiO₂ layers. However, this interface presents one Si dangling bond per unit cell known to produce interfacial states in the band gap [83, 84]. Following this spirit, Shirasawa *et al.* reported very recently on the formation of an epitaxial silicon oxynitride (SiON) layer on a 6*H*-SiC(0001) surface [82]. According to the proposed atomic structure, this

epitaxial layer is attached to an abrupt SiC(0001) surface, without showing any dangling bond. The measured scanning tunneling spectroscopy (STS) current-voltage characteristic on the SiON layer exhibits a band gap of ~9 eV, comparable to that of bulk SiO_2 [82]. This electronic property appears particularly intriguing since the silicate layer only extends over ~4 Å [82]. By growing a thicker dielectric layer on the SiON while maintaining the atomically abrupt SiC/SiON interface, the interface problems of the devices are expected to be greatly improved [82].

1.5 Outline of the thesis

In this thesis, we first set out to generate a model structure of the interface between $4H$-SiC(0001) and amorphous SiO_2. We here focus on the generation of an abrupt interface model. Such an abrupt model provides a realistic description of the interfacial bonding pattern at SiC/SiO_2 interfaces obtained through the oxidation of 3×3 or $\sqrt{3}\times\sqrt{3}R30°$ reconstructed SiC(0001) surfaces [85, 86]. We then investigate the electronic properties of the generated model interface using hybrid density functionals, which incorporate a fraction of the Hartree-Fock exchange interaction. The use of such functionals is motivated by the necessity of accurately describing band gaps and band offsets, which are known to be poorly described by standard density functional schemes. Indeed, the identification of typical near interface defects is expected to mainly rest on the position of energy levels with respect to the relevant band edges. For our abrupt model interface, the band gap of the oxide is already fully recovered at a distance of 5 Å from the interface. This extent is in excellent agreement with internal photoemission measurements, thereby providing support for the abruptness of the actual $4H$(0001)-SiC/SiO_2 interface. A new scheme for the calculations of band offsets is presented. The calculated band offsets agree with their experimental counterparts within 0.1 eV.

We then study several semiconductor and oxide defects at the $4H$-SiC/SiO_2 interface using spin-polarized hybrid density functionals for identifying candidate defects responsible for the high density of interface defects measured in the $4H$-SiC band gap. Using the previously designed model structure of the $4H$-SiC(0001)/SiO_2 interface, we determine the energy levels of several defects expected to be created at the interface during oxidation. Focusing on the D_{it} in the upper part of the $4H$-SiC band gap, we identify the C-C pair involving sp^2 hybridized carbon atoms as a possible contributor. The hydrogen bridge defect in

the oxide also appears to have an energy level high in the SiC band gap close to the experimentally measured peak at 0.1 eV below the $4H$-SiC conduction band. However, these two defects feature broad level distributions and other defect levels in the mid/low part of the SiC band gap, which discard them as possible candidates at the origin of the sharp peak of the D_{it}. We then study the passivation of defects by hydrogen and nitrogen, finding that both species can effectively passivate carbon atoms involved in the C-C pair defect. This confirms the experimental D_{it} decrease at interfaces treated by atomic hydrogen and nitrogen.

The possibility of growing epitaxial silicate adlayers on SiC is then investigated as an alternative approach to greatly reduce the D_{it}. Our calculations confirm that epitaxial silicon oxynitride adlayers can have atomically abrupt SiC/silicate interfaces and be expected to be ideal seeds for the epitaxial growth of SiO_2 layers. In accord with experiment, it was shown that the band gap in the thin silicate layer at the surface is close to that of bulk SiO_2. This effect was identified as resulting mainly from the presence of nitrogen atoms that repel the semiconductor states and cause an early band gap opening in correspondence of the last substrate planes.

The present thesis is organized as follows. In Chapter 2, we give a description of the methods and techniques used in this thesis. The generation of the abrupt model structure of the $4H(0001)$SiC/SiO_2 interface is reported in Chapter 3. The structural and electronic properties are also described. In Chapter 4, candidate defects for the high density of defect states near the SiC conduction band are examined through the study of their energy levels and charge transition levels. The passivation of the C-C pair defect by hydrogen and nitrogen is also studied. The electronic properties of a recently grown epitaxial silicon oxynitride structure are under scope in Chapter 5, where an explanation for their origin is provided. Finally, we draw the conclusions of this thesis.

Chapter 2

Methods

The goal of this chapter is to give a concise summary of the methods used in this work. For completeness, see the references in the text.

2.1 Classical molecular dynamics

2.1.1 Model for particle interactions

In classical molecular dynamics, the atoms are most often described by point-like centers which interact through pair- or multibody interaction potentials. In the absence of external force fields, the system (of N atoms) is completely determined through its Hamiltonian

$$\mathcal{H} = \sum_{i=1}^{N} \frac{\mathbf{p}_i{}^2}{2m_i} + \sum_{i<j}^{N} V(\mathbf{r}_i, \mathbf{r}_j) + \sum_{i,j<k}^{N} V^{(3)}(\mathbf{r}_i, \mathbf{r}_j, \mathbf{r}_k) + \dots, \tag{2.1}$$

where $\mathbf{p}$ is the momentum, m the mass of the particles, V and $V^{(3)}$ are the pair and three-body interaction potentials, respectively. In the classical model, the highly complex description of electron dynamics is replaced by an effective picture where the main features like the hard core of a particle, electric multipoles or internal degrees of freedom are modeled by a set of parameters and analytical functions which depend only on the mutual position of the particles in the system. As shown in Eq. (2.1), multibody potentials can be incorporated in the Hamiltonian expression to refine the description of interactions but the workload of the calculation increases with the counting of interacting neighbors.

Depending on their spatial extent, the potentials in Eq. (2.1) can be referred to as short or long ranged. If the potential falls to zero faster than r^{-d}, where r

is the separation between two particles and d is the dimension of the problem, it is called short ranged, and otherwise, it is long ranged. Short range interactions can then be estimated by taking into account only neighboring particles up to a certain cutoff radius r_c. If needed, long range corrections can be introduced to compensate for discarded interactions with remote particles. There are basically two components to the short range potential. First, the excluded volume of a particle is represented by a steep potential repulsive at short distances. Second, the van der Waals forces take into account interactions between permanent dipoles, between permanent and induced dipoles (polarization), and between instantaneous dipoles due to electron fluctuations in molecules (London forces). The short range potential can be written in the Buckingham form as

$$U_{\text{SR},\alpha\beta}^{B}(\mathbf{r}_{ij}) = A_{\alpha\beta}e^{-B_{\alpha\beta}\mathbf{r}_{ij}} - \frac{C_{\alpha\beta}}{\mathbf{r}_{ij}^{6}}, \tag{2.2}$$

where α and β indicate the species of the particles, and A, B, C are parameters for intra-species interactions ($\alpha = \beta$) and cross-species interactions ($\alpha \neq \beta$).

In the case of long range potentials, like the Coulomb potential, and when periodic boundary conditions are applied, interactions with all the particles in the central cell but also with all periodic images must be taken into account and a lattice sum has to be evaluated

$$U_{LR} = \frac{1}{2} \sum_{i,j=1}^{N} \sum_{\mathbf{n}}' \frac{q_i q_j}{|\mathbf{r}_{ij} - \mathbf{n}L|}, \tag{2.3}$$

where $\mathbf{n}$ is a lattice vector and $\sum_{n}'$ means that for $\mathbf{n} = 0$, $i \neq j$. This type of lattice sum is known to be conditionally convergent [87] and a method to overcome this problem invented by Ewald [88] must be used. The Ewald summation relies on the separation of Eq. (2.3) into a short-range and a long-range term that sums up quickly in real space and in Fourier space, respectively (for more details on the derivation of the Ewald sum, see Refs. [89, 90]).

Finally, the total Hamiltonian reads:

$$\mathcal{H} = \sum_{i=1}^{N} \frac{\mathbf{p}_i^2}{2m_i} + \sum_{i<j}^{N} A_{\alpha\beta}e^{-B\alpha\beta\mathbf{r}_{ij}} - \frac{C_{\alpha\beta}}{\mathbf{r}_{ij}^{6}} + \frac{1}{2} \sum_{i,j=1}^{N} \sum_{\mathbf{n}}' \frac{q_i q_j}{|\mathbf{r}_{ij} - \mathbf{n}L|}. \tag{2.4}$$
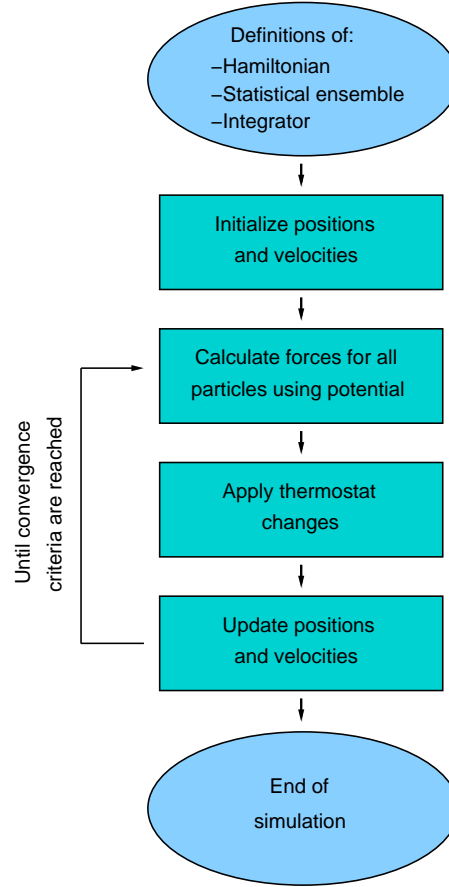
Figure 2.1: Flow chart of the major steps involved in a classical molecular dynamics simulation.

2.1.2 The Verlet integrator

The dynamical evolution of the system can be deduced from this Hamiltonian and the integration of the canonical Hamilton equations. During the energy minimization step, the total energy of the system in the initial state at time t is calculated. Then an integrator is used to predict all new vectors at the next time step $t + \delta t$. Beacause of its simple implementation and modest storage requirements, the Verlet algorithm is a commonly used integrator. The positions at $t + \delta t$ and $t - \delta t$ can be approximated by a Taylor series expansion:

$$
\begin{aligned}
\mathbf{r}(t + \delta t) &= \mathbf{r}(t) + \mathbf{v}(t)\delta t + \frac{1}{2}\mathbf{a}(t)\delta t^2 + \dots, & (2.5) \\
\mathbf{r}(t - \delta t) &= \mathbf{r}(t) - \mathbf{v}(t)\delta t + \frac{1}{2}\mathbf{a}(t)\delta t^2 + \dots. & (2.6)
\end{aligned}
$$

Summing these two equations, one obtains:

$$
\mathbf{r}(t + \delta t) = 2\mathbf{r}(t) - \mathbf{r}(t - \delta t) + \mathbf{a}(t)\delta t^2. \tag{2.7}
$$

The Verlet algorithm uses positions and accelerations at time t and the positions at time $t - \delta t$ to calculate the new positions at $t + \delta t$.

2.1.3 The Langevin thermostat

The velocities or accelerations of the particles can then be modulated by a thermostat to maintain the system temperature at a set value. In the Langevin thermostat, all particles receive at each time step a random force and have their velocities lowered using a constant friction [91]. The average magnitude of the random forces and the friction are related in such a way that the fluctuation-dissipation theorem is obeyed [92, 93], thereby guaranteeing canonical ensemble statistics. In this formalism, the equation of motion for each particle i is modified as

$$m\mathbf{a}_i = -\nabla_i U - m\Gamma\mathbf{v}_i + \mathbf{W}_i(t)\,, \tag{2.8}$$

where Γ is the friction coefficient, and $\mathbf{W}_i$ is a random force whose variance is a function of temperature and time step. The random force is therefore balanced with the frictional force and maintains the system temperature at the set value. Fig. 2.1 sums up the major steps involved in a classical molecular dynamics simulation. For further information on clasical molecular dynamics we refer to Refs. [94, 95].

2.2 Density functional theory

Density functional theory is a quantum mechanical theory used to investigate the ground state of many-body systems. The Hamiltonian describing such systems can be written as

$$\mathcal{H} = -\sum_I \frac{\hbar^2}{2M_I}\nabla_I^2 - \sum_i \frac{\hbar^2}{2m_e}\nabla_i^2 + \sum_{i<j} \frac{e^2}{|\mathbf{r}_i - \mathbf{r}_j|} - \sum_{I,i} \frac{e^2 Z_I}{|\mathbf{R}_I - \mathbf{r}_i|} + \sum_{I<J} \frac{e^2 Z_I Z_J}{|\mathbf{R}_I - \mathbf{R}_J|}\,, \tag{2.9}$$

for the electronic $\mathbf{r}_i$ and nuclear $\mathbf{R}_I$ degrees of freedom. The contributions to the Hamiltonian are the kinetic term associated with the nuclei, the kinetic term related to the electrons, and the electron-electron, electron-nuclear, and nuclear-nuclear Coulomb interactions. The description of the system is provided by the time-independent Schrödinger equation

$$\mathcal{H}\Psi(\mathbf{r}_i, \mathbf{R}_I) = E\Psi(\mathbf{r}_i, \mathbf{R}_I)\,, \tag{2.10}$$

whose exact solution becomes rapidly extremely difficult in many-body systems.

2.2.1 Born-Oppenheimer approximation

The adiabatic Born-Oppenheimer approximation which relies on the significant difference between the mass of the electrons and those of ions brings a first simplication. In this picture, the nuclei of the system are seen as fixed, generating a static external potential V_{ext} in which the electrons are moving. The total wave function in Eq. (2.10) can then be separated into the product of a nuclear part and an electronic part $\psi(\mathbf{r}_i, \mathbf{R}_I)$ and the Hamiltonian in Eq. (2.9) rewritten as

$$\mathcal{H} = -\sum_I \frac{\hbar^2}{2M_I}\nabla_I^2 - \sum_i \frac{\hbar^2}{2m_e}\nabla_i^2 + \sum_{i<j} \frac{e^2}{|\mathbf{r}_i - \mathbf{r}_j|} + V_{ext}(\mathbf{r}_i) \tag{2.11}$$

$$= -\sum_I \frac{\hbar^2}{2M_I}\nabla_I^2 + \mathcal{H}_e(\mathbf{r}_i, \mathbf{R}_I)\,. \tag{2.12}$$

The problem has therefore been simplified to a system of electrons interacting with each other in the external potential $V_{ext}(\mathbf{r}_i)$ generated by the nuclei and a stationary electronic state is described by the wavefunction $\psi(\mathbf{r}_i, \mathbf{R}_I)$ satisfying the many-electron Schrödinger equation

$$\mathcal{H}_e\psi(\mathbf{r}_i, \mathbf{R}_I) = E\psi(\mathbf{r}_i, \mathbf{R}_I)\,, \tag{2.13}$$

with

$$\mathcal{H}_e = -\sum_i \frac{\hbar^2}{2m_e}\nabla_i^2 + \sum_{i<j} \frac{e^2}{|\mathbf{r}_i - \mathbf{r}_j|} + V_{ext}(\mathbf{r}_i). \tag{2.14}$$

2.2.2 Hohenberg-Kohn theorems and Kohn-Sham formalism

Hohenberg-Kohn theorems

The main objective of density functional theory is to replace the many-body electronic wave function with the electronic density as the basic quantity. The density being a function of only three variables, it is a much simpler variable to deal with than the many-body wave function depending on $3N$ variables (where N is the number of electrons in the system).

Hohenberg and Kohn [96] showed that *(i)* the external potential and hence the total energy is a unique functional of the electron density $n(\mathbf{r})$ and that *(ii)* the ground-state energy can be obtained variationally, i. e. the density that minimizes the total energy is the exact ground-state density.

The energy functional can be written in terms of the external potential V_{ext} as

$$E[n(\mathbf{r})] = \int V_{ext}(\mathbf{r})n(\mathbf{r})d\mathbf{r} + F[n(\mathbf{r})]\,, \tag{2.15}$$

where $F[n(\mathbf{r})]$ is an unknown universal functional of only the electron density $n(\mathbf{r})$, representing the kinetic and electron-electron repulsion energies. The variation of the total energy leads to the Euler equation

$$\mu = \frac{\delta E_v[n(\mathbf{r})]}{\delta n(\mathbf{r})} = V_{ext}(\mathbf{r}) + \frac{\delta F[n(\mathbf{r})]}{\delta n(\mathbf{r})}\,, \tag{2.16}$$

where the Lagrange multiplier μ is introduced to impose $\int n(\mathbf{r})d\mathbf{r} = N$.

In principle, the ground-state electron density can be determined by solving Eq. (2.16). However, we do not know the exact form of the functional $F[n(\mathbf{r})]$.

Kohn-Sham formalism

Kohn and Sham proposed to consider a non-interacting system of electrons moving within an effective Kohn-Sham single particle potential $V_{KS}(\mathbf{r})$. In that case, the functional $F[n(\mathbf{r})]$ can be written as

$$F[n(\mathbf{r})] = T_S[n(\mathbf{r})] + E_H[n(\mathbf{r})] + E_{XC}[n(\mathbf{r})]\,, \tag{2.17}$$

where $T_S[n(\mathbf{r})]$ is the kinetic energy of a non-interacting electron gas of density $n(\mathbf{r})$, $E_H[n(\mathbf{r})] = \frac{1}{2} \int \int \frac{n(\mathbf{r})n(\mathbf{r}')}{|\mathbf{r}-\mathbf{r}'|}d\mathbf{r}d\mathbf{r}'$ is the classical electrostatic Hartree energy of the electrons, and $E_{XC}[n(\mathbf{r})]$ is the exchange-correlation energy which contains the non-classical contributions to the electron-electron interactions as well as the difference between the exact and non-interacting kinetic energies.

Equation (2.16) can then be rearranged as

$$\mu = V_{KS}(\mathbf{r}) + \frac{\delta T_S[n(\mathbf{r})]}{\delta n(\mathbf{r})}\,, \tag{2.18}$$

where

$$V_{KS}(\mathbf{r}) = V_{ext}(\mathbf{r}) + V_H(\mathbf{r}) + V_{XC}(\mathbf{r})\,, \tag{2.19}$$

with

$$V_H(\mathbf{r}) = \frac{\delta E_H[n(\mathbf{r})]}{\delta n(\mathbf{r})} = \int \frac{n(\mathbf{r}')}{|\mathbf{r} - \mathbf{r}'|} d\mathbf{r}' \,, \tag{2.20}$$

and

$$V_{XC}(\mathbf{r}) = \frac{\delta E_{XC}(\mathbf{r})}{\delta n(\mathbf{r})} \,. \tag{2.21}$$

The density of the non-interacting Kohn-Sham system is then equal to the density of the exact ground-state density. The ground-state density is obtained by solving the N single-particle Schrödinger equations

$$\left[-\frac{\hbar^2}{2m_e} \nabla^2 + V_{KS}(\mathbf{r}) \right] \psi_i(\mathbf{r}) = \epsilon_i \psi_i(\mathbf{r}) \tag{2.22}$$

where ϵ_i are the Lagrange multipliers imposing the orthonormality of the N single-particle wavefunctions $\psi_i(\mathbf{r})$. The density is then constructed from

$$n(\mathbf{r}) = \sum_{i=1}^{N} |\psi_i(\mathbf{r})|^2 \,, \tag{2.23}$$

and the non-interacting kinetic energy deduced as:

$$T_S[n(\mathbf{r})] = -\frac{1}{2} \sum_{i=1}^{N} \int \psi_i^*(\mathbf{r}) \nabla^2 \psi_i(\mathbf{r}) d\mathbf{r} \,, \tag{2.24}$$

$V_{KS}(\mathbf{r})$ depending on the density through $V_{XC}(\mathbf{r})$ in Eq. (2.19). Equations (2.22) and Eq. (2.23) must be solved self-consistently.

2.2.3 Exchange-correlation functionals

The local-density approximation

The reliability of the Kohn-Sham theory directly depends on the quality of the approximation of the unknown exchange-correlation functional $E_{XC}(\mathbf{r})$. The simplest aproximation is known as the local density approximation (LDA) and assumes that the density can be treated locally as a uniform electron gas. The exchange correlation energy (E_{XC}) of a non-uniform interacting electron system is then replaced by the E_{XC} of a uniform interacting electron system with the same density. This approximation, first introduced by Kohn and Sham [97], holds for

systems with slowly varying electron densities. The LDA exchange correlation energy for a density $n(\mathbf{r})$ is given as

$$E_{XC}^{LDA} = \int n(\mathbf{r}) \epsilon_{XC}[n(\mathbf{r})] d\mathbf{r} \,, \tag{2.25}$$

where $\epsilon_{XC}[n(\mathbf{r})]$ is the exchange-correlation energy per particle of a uniform electron gas of density $n(\mathbf{r})$. $\epsilon_{XC}[n(\mathbf{r})]$ can be split into exchange and correlation energy: $\epsilon_{XC}[n(\mathbf{r})] = \epsilon_X[n(\mathbf{r})] + \epsilon_C[n(\mathbf{r})]$. The exchange energy is given by the Dirac functional [98]:

$$\epsilon_X[n(\mathbf{r})] = -\frac{3}{4} \left(\frac{3}{\pi}\right)^{\frac{1}{3}} n^{\frac{1}{3}}(\mathbf{r}) \,. \tag{2.26}$$

Accurate values for $\epsilon_C[n(\mathbf{r})]$ have been determined by quantum Monte Carlo calculations [99] of homogeneous electron gases at various densities and extrapolated to provide an analytic form [100].

As stated before, the local density approximation holds for slowly varying systems and could be questionable when applied to atoms, molecules, and solids. However, LDA gives surprisingly good results[1] compared to experiment [101]. The application of LDA to a large variety of systems was shown to reproduce satisfactorily many physical quantities such as ground-state atomic structures and vibrational properties of molecules and solids [101]. However, LDA overestimates the cohesive energies of solids while it often underestimates the lattice constants [103, 104, 105]. Also, the description of weak bonds like hydrogen bonds, intermolecular bonds, or adsorption bonds is often poor [101]. Finally, LDA drastically fails in the description of band gap of semiconductors and insulators. This aspect is a major drawback for the study of defects at semiconductor-oxide interfaces.

Generalized gradient approximations

A natural extension to improve upon the LDA is the generalized gradient approximation (GGA) in which E_{XC} depends not only on the density, but also on its gradient:

$$E_{XC}^{GGA} = \int f_{XC}(n(\mathbf{r}), \nabla n(\mathbf{r})) d\mathbf{r} \,. \tag{2.27}$$

In comparison with the LDA, GGAs tend to improve total energies [106], atomization energies [106, 107, 108], energy barriers, and structural energy differences

---

[1]See Refs. [101, 102] for a rationale on the success of LDA.

[109, 110, 111]. GGAs expand and soften bonds, thereby correcting [112] and sometimes overcorrecting [113] the LDA prediction.

While the exchange-correlation energy of a uniform electron gas is well established [114], the best choice for $f_{XC}[n(\mathbf{r}), \nabla n(\mathbf{r})]$ is still a matter of debate. Most of the GGAs are based on some combination of two limiting strategies: *(i)* fitting of some set of experimental data and *(ii)* fulfillment of a number of well known physical constraints. Semi-empirical GGAs can be remarkably successful for small molecules, but fail for delocalized electrons in the uniform gas and thus in metallic systems. A first-principles numerical GGA proposed by Perdew and Wang (and referred to as PW91) was constructed by starting from the second-order density-gradient expansion for the exchange-correlation hole surrounding the electron in a system of slowly varying density, then cutting off its spurious long-range parts to satisfy sum rules for the exact hole [115]. Perdew, Burke and Ernzerhof then proposed a simplification of PW91, deriving a GGA called PBE in which all the parameters (other than those in its LDA component) are fundamental constants [116]. Improvements over PW91 include an accurate description of the linear response of the uniform electron gas, correct behaviour under uniform scaling, and a smoother potential. Several benchmarks have already been published on this functional with remarkable results [117, 118, 119, 120, 121], and some modification of the parameters entering the definition of the exchange funtional has been suggested to further improve its accuracy [122]. In the GGA calculations in this work, the PBE functional will be used.

Hybrid functionals

Another avenue towards increased reliability is provided by hybrid functionals which include a part of the exact Hartree-Fock exchange energy[1]. They all rely on the rigorous *ab initio* formula for the exchange-correlation energy E_{XC} of Kohn-Sham density-functional theory known as the "adiabatic connection" formula [124]

$$E_{XC} = \int_0^1 E_{XC}^\lambda \, d\lambda \,, \tag{2.28}$$

where

---

[1] See Ref. [123] for comments on the exactness of the term "Hartree-Fock" theory in the Kohn-Sham density-functional context

$$E_{XC}^{\lambda} = \langle \Psi_{\lambda} | V_{ee} | \Psi_{\lambda} \rangle - \frac{1}{2} \int d\mathbf{r} \int d\mathbf{r}' \frac{n(\mathbf{r})n(\mathbf{r}')}{|\mathbf{r} - \mathbf{r}'|} , \qquad (2.29)$$

which connects the non-interacting Kohn-Sham reference system ($\lambda = 0$) to the fully interacting real system ($\lambda = 1$) through a continuum of partially interacting real systems, all sharing a common density.

The first simple approximation proposed by Becke for the λ dependence of the integrand in Eq. (2.28) was a linear interpolation called "half-and-half" theory [123] resulting in the following approximate exchange-correlation energy:

$$E_{XC} \simeq \frac{1}{2} U_{XC}^0 + \frac{1}{2} U_{XC}^1 . \qquad (2.30)$$

Here U_{XC}^0 is the exchange-correlation energy of the non-interacting system and U_{XC}^0 is the exchange-correlation energy of the fully-interacting system [123].

To go beyond several deficiencies of this "half-and-half" theory [125], Becke proposed to incorporate gradient corrections for exchange and correlation in the exchange-correlation approximation [125]. Three empirical paramaters are introduced to rule the mixing of Hartree-Fock (HF) exchange and density-functional (DF) exchange and correlation [125]. The expression for the exchange-correlation approximation underlying the ACM3 (Adiabatic Connection Method) hybrid schemes reads:

$$E_{XC}^{ACM3} = E_{XC}^{LDA} + a_0(E_X^{HF} - E_X^{LDA}) + a_X \Delta E_X^{GGA} + a_C \Delta E_C^{GGA} . \qquad (2.31)$$

More recently, Becke suggested that only one coefficient is enough to rule the HF/DF exchange ratio [126] according to:

$$E_{XC}^{ACM1} = E_{XC}^{GGA} + a_X(E_X^{HF} - E_X^{GGA}) . \qquad (2.32)$$

These methods, referred to as ACM1, are quite succesful [127, 128, 129] and it has been shown that non-empirical hybrid schemes employing a system- and property-dependent mixing coefficient can be accurately approximated by Eq. (2.32) [129].

Perdew *et al.* then provided a rationale for the optimum value of a_X based on fourth-order perturbation theory in the case of molecular systems [130]. Because no additional adjustable parameters other than their GGAs constituents appear, this family of adiabatic connection functionals are referred to as ACM0:

$$E_{XC}^{ACM0} = E_{XC}^{GGA} + \frac{1}{4}(E_X^{HF} - E_X^{GGA}) . \qquad (2.33)$$

PBE0, which is based on the Perdew-Burke-Ernzerhof (PBE) exchange-correlation functional, was shown to give very good predictions for molecular atomization energies [130]. The B0LYP functional (based on Becke exchange and Lee-Yang-Parr correlation functionals) was also shown to give results comparable to those of three-parameter hybrids like B3LYP [131, 132]. The *m*PW1PW functional [132] (based on an optimized Perdew-Wang exchange-correlation functional) is not only competitive with the B0LYP approach for covalent interactions, but also improves on the non-covalent description through a better representation of the low density and large gradient regions between the atoms [132, 133, 134].

In recent years, hybrid functionals have successfully been applied to solids to predict quite accurately band gaps, lattice parameters, bulk moduli, heats of formation [135, 136, 137, 138]. Hybrid functionals are particularly appealing due to their ability to overcome GGA's failure to reproduce experimental band gaps. This is of crucial importance in the study of defects and their level positions [34, 139, 140, 141, 142, 143]. In this work, the PBE0 functional will be used to further improve PBE results and allow more reliable comparisons with experiments.

Screened Coulomb hybrid density functionals

To reduce numerical load when calculating exact Hartree-Fock exchange in large molecules and solids, Heyd *et al.* introduced a hybrid scheme based on substitutional screened potential for the full $1/r$ Coulomb potential [144]. In this scheme, it is essential to treat the short- and long-range Coulomb interactions in a consistent way [144]. This approach yields an accuracy comparable to B3LYP and PBE0 while reducing the computational effort [137, 144, 145].

The screened Coulomb potential is achieved by splitting the Coulomb operator into short-range (SR) and longe-range(LR) components. In this work, we used a screened variant of the PBE0 functional in which the error function was used to accomplish the split:

$$\frac{1}{r} = \underbrace{\frac{\mathrm{erfc}(\beta r)}{r}}_{SR} + \underbrace{\frac{\mathrm{erf}(\beta r)}{r}}_{LR} \ . \tag{2.34}$$

In this equation the complementary error function $\mathrm{erfc}(\beta r) = 1 - \mathrm{erf}(\beta r)$ and β is an adjustable parameter. For $\beta = 0$, the long-range term becomes zero and the short-range term is equivalent to the full Coulomb operator.

The introduction of a screened Coulomb potential has an effect on the for-

mulation of the PBE exchange energy. The PBE exchange energy is defined as [146]

$$E_X^{PBE} = \int \rho(\mathbf{r})\epsilon_X^{PBE}(\rho(\mathbf{r}), s(\mathbf{r}))d\mathbf{r}\,, \tag{2.35}$$

where $\rho(\mathbf{r})$ is the electronic density, $s = |\nabla\rho|/(2k_F\rho)$, and $k_F = (3\pi^2\rho)^{1/3}$ is the reduced gradient. ϵ_X is defined as the product of the LDA exchange energy density and an enhancement factor F_X^{PBE} depending on the reduced gradient of the electron density:

$$\epsilon_X^{PBE}(\rho(\mathbf{r}), s(\mathbf{r})) = \epsilon_X^{LDA}(\rho(\mathbf{r})) \times F_X^{PBE}(s(\mathbf{r}))\,. \tag{2.36}$$

The exchange-hole based formulation of the PBE functional defines F_X^{PBE} as an integral over the PBE exchange hole $J^{PBE}(s,y)$

$$F_X^{PBE}(s(r)) = -\frac{8}{9}\int_0^\infty yJ^{PBE}(s,y)dy\,, \tag{2.37}$$

where $y = k_F u$ is the reduced interelectronic separation. In the short-range PBE exchange energy formulation, the exchange hole is screened by employing the short-range Coulomb potential defined in Eq. (2.34):

$$J^{\beta PBE,SR}(\rho, s, y) = J^{PBE}(s,y) \times \mathrm{erfc}\left(\frac{\beta y}{k_F}\right)\,. \tag{2.38}$$

The short-range exchange hole can be expressed with parameters and parametrized functions of the PBE exchange hole [146].

The βPBE long-range exchange contribution is then defined as:

$$E_X^{\beta PBE,LR} = \int \rho(\mathbf{r})\left[\epsilon_X^{PBE}(\rho(\mathbf{r}), s(\mathbf{r})) - \epsilon_X^{\beta PBE,SR}(\rho(\mathbf{r}), s(\mathbf{r}))\right]\,. \tag{2.39}$$

2.2.4 Implementation

Plane-wave expansion

The plane-wave formalism has been introduced in view of solving Eq. (2.22) in the case of an infinitely extended crystal by employing a cell-based approach and Born-von-Kármán periodic boundary conditions: plane waves of the form $\psi_{\mathbf{k}}(\mathbf{r}) \propto e^{i\mathbf{k}\cdot\mathbf{r}}$ with the wave vector k fulfilling Bloch theorem $\psi_{\mathbf{k}}(\mathbf{r}+\mathbf{R}) = e^{i\mathbf{k}\cdot\mathbf{R}}\,\psi_{\mathbf{k}}(\mathbf{r})$ for every lattice vector $\mathbf{R}$. The periodicity allows one to describe the crystal by considering only one unit cell and to expand the Kohn-Sham orbitals in a Fourier series:

$$\psi_i(\mathbf{r}) \equiv \psi_{n,\mathbf{k}} = \frac{1}{\sqrt{\Omega}} \sum_{\mathbf{G}} c_n(\mathbf{k} + \mathbf{G}) e^{i(\mathbf{k}+\mathbf{G})\cdot\mathbf{r}} , \qquad (2.40)$$

where the sum extends over the reciprocal lattice vectors $\mathbf{G}$, and Ω is the volume of the unit cell. Then, the electronic structure is characterized by the band index n and the wave vector $\mathbf{k}$ restricted to the first Brillouin zone.

The representation of the Kohn-Sham wave functions in the form of Eq. (2.40) allows for an easy control of the convergence behaviour by systematically increasing the number of Fourier coefficients $\mathbf{G}$. For Γ point sampling, the number of wavefunctions used is controlled by the largest wave vector $\mathbf{G}_{max}$ in the Fourier expansion which fixes the energy cutoff as $E_{cut} = \hbar^2 |\mathbf{G}_{max}|^2 / 2m_e$. Other advantages of using a plane wave formulation are that the same basis set can be used for all atomic species and that plane waves do not depend on nuclear positions so that correction terms are not needed for the calculation of forces, unlike in the case of localized basis sets [147].

The plane wave basis set formulation can also be applied to a non-periodic system. The system is then placed at the centre of a periodic supercell. If the supercell is large enough the interactions between systems in neighbouring cells become negligible.

Pseudopotentials

The electronic structure of an atom consists of core states and valence states. The inner orbitals are tightly bound to the nucleus and hardly influenced by the interaction with neighbouring species while the outer electrons lay at higher energies and are almost entirely responsible for the bonding properties of the system. Based on these properties, pseudopotentials (PPs) were introduced to simplify electronic calculations by replacing the nucleus and the "frozen" core with their combined effective influence on the valence electrons. The pseudopotentials used in this thesis are norm-conserving [148] and fulfill the following requirements:

- the ground-state pseudo valence eigenvalues match exactly the all-electron (AE) values;

- the pseudo wavefunctions and the AE orbitals are identical beyond a chosen core radius r_c;

- the integrals from 0 to r of the AE and pseudo charge densities agree for $r > r_c$ for each valence state (norm conservation);

- the logarithmic derivatives of the AE and pseudo wavefunctions, and their first energy derivatives agree for $r > r_c$.

The norm-conservation of the charge is an essential requisite for the accuracy of the pseudopotential and must be imposed to each angular momentum wave. To achieve high accuracy norm-conserving PPs are non-local, i.e. they contain a term which depends on the angular momenta l of the wavefunction they act on. They can be written as

$$V^{PP}(\mathbf{r}) = \sum_{lm} |lm\rangle V_l(r)\langle lm| \,, \tag{2.41}$$

where the $|lm\rangle$ are spherical harmonics, and V_l is the pseudopotential for angular momentum l. This formulation is expensive as the evaluation of Eq. (2.41) requires $N_{pw}N_k(N_{pw} + 1)/2$ projectors to be calculated for each angular momentum component l, where N_{pw} is the number of plane waves in the expansion and N_k is the number of points in the Brillouin zone.

In the Kleinman-Bylander form [149], this semi-local form is replaced by a fully separable non-local formulation:

$$V^{PP} = V^{local} + \sum_{lm} \frac{|\psi_{lm}\delta V_l\rangle\langle\delta V_l\psi_{lm}|}{\langle\psi_{lm}\,|\delta V_l|\,\psi_{lm}\rangle} \tag{2.42}$$

where V_{local} is an arbitrary local potential, ψ_{lm} are the pseudo wave functions for a reference state, and δV_l is defined through

$$\delta V_l = V_l - V_{local} \,, \tag{2.43}$$

where V_l is the l angular momentum component of the pseudopotential in its semi-local form [Eq. (2.41)]. Writing the pseudopotential in this form allows the number of integrals of V^{PP} for an energy-band calculation to be reduced to $N_{pw}N_k$. In this work we will use norm-conserving pseudopotentials in the Kleinman-Bylander form calculated within the Troullier and Martins scheme [150].

Divergence of the exchange energy

In hybrid functional schemes, the self-consistent band-structure calculation involves exchange matrix elements of the type [151]

$$\langle f|\Sigma_{HF}|g\rangle = -\sum_{m,\mathbf{q}} \int \frac{f^*(\mathbf{r})\phi_{m\mathbf{q}}^*(\mathbf{r}')\phi_{m\mathbf{q}}(\mathbf{r})g(\mathbf{r}')}{|\mathbf{r}-\mathbf{r}'|}d^3\mathbf{r}d^3\mathbf{r}'\,, \qquad (2.44)$$

where Σ_{HF} is the Hartree-Fock self-energy operator, the sum is over all occupied Bloch orbitals $\phi_{m\mathbf{q}}$, and f and g are basis functions. Using the decomposition of $\phi_{m\mathbf{q}}$ in plane waves

$$\phi_{m\mathbf{q}}(\mathbf{r}) = \frac{1}{\sqrt{\Omega}}\sum_{G} c_{m\mathbf{q}}(\mathbf{G})e^{i(\mathbf{q}+\mathbf{G})\cdot\mathbf{r}}\,, \qquad (2.45)$$

the exchange matrix element becomes:

$$\langle\mathbf{k}+\mathbf{G}|\Sigma_{HF}|\mathbf{k}+\mathbf{G}'\rangle = -\frac{4\pi}{\Omega}\sum_{m,\mathbf{q}}\sum_{G''}\frac{c_{m,\mathbf{q}}^*(\mathbf{G}'+\mathbf{G}'')c_{m,\mathbf{q}}(\mathbf{G}+\mathbf{G}'')}{|\mathbf{k}-\mathbf{q}-\mathbf{G}''|^2}\,. \qquad (2.46)$$

For calculations at the Γ point, Eq. (2.46) reduces to:

$$\langle\mathbf{G}|\Sigma_{HF}|\mathbf{G}'\rangle = -\frac{4\pi}{\Omega}\sum_{m}\sum_{G''}\frac{c_{m}^*(\mathbf{G}'+\mathbf{G}'')c_{m}(\mathbf{G}+\mathbf{G}'')}{|\mathbf{G}''|^2}\,. \qquad (2.47)$$

This sum contains a divergent term at $\mathbf{G}'' = 0$. In the spirit of Gygi and Baldereschi [151], we add and substract a term which has exactly the same divergence at $\mathbf{G}'' = 0$:

$$\langle\mathbf{G}|\Sigma_{HF}|\mathbf{G}'\rangle = -\frac{4\pi}{\Omega}\sum_{m}\sum_{G''}\left(\frac{c_{m}^*(\mathbf{G}'+\mathbf{G}'')c_{m}(\mathbf{G}+\mathbf{G}'')}{|\mathbf{G}''|^2} - c_{m}^*(\mathbf{G}')c_{m}(\mathbf{G})F(\mathbf{G}')\right)$$
$$-\frac{4\pi}{\Omega}\sum_{m}c_{m}^*(\mathbf{G}')c_{m}^*(\mathbf{G})\sum_{G''}F(\mathbf{G}'')\,. \quad (2.48)$$

The auxiliary function $F(x)$ is an auxiliary function that diverges like $1/x^2$ when $x \to 0$ and is smooth everywhere. The term in large parentheses is no longer divergent. The divergence of the last term of Eq. (2.48) disappears for very large systems where the sum can be changed into an integral over the $\mathbf{G}$ space

$$-\frac{4\pi}{\Gamma}\sum_{G''}F(\mathbf{G}'') \approx -\frac{1}{2\pi^2}\int F(\mathbf{G}'')d^3\mathbf{G}''\,. \qquad (2.49)$$

The exchange matrix element becomes

$$\langle\mathbf{G}|\Sigma_{HF}|\mathbf{G}'\rangle = -\sum_{m}\sum_{G''}c_{m}^*(\mathbf{G}'+\mathbf{G}'')c_{m}(\mathbf{G}+\mathbf{G}'')\phi(\mathbf{G}'')\,, \qquad (2.50)$$

with

$$\phi(\mathbf{G}) = \begin{cases} \frac{4\pi}{\Omega \mathbf{G}^2} & \text{for } \mathbf{G} \neq 0 \\ \beta & \text{for } \mathbf{G} = 0 \end{cases}, \tag{2.51}$$

and

$$\beta = \frac{1}{2\pi^2} \int F(\mathbf{G}) d^3\mathbf{G} - \frac{4\pi}{\Omega} \sum_{\mathbf{G} \neq 0} F(\mathbf{G}). \tag{2.52}$$

The auxiliary function F used in this work has the form

$$F(\mathbf{G}) = \frac{e^{-\gamma G^2}}{G^2}. \tag{2.53}$$

The $\mathbf{G} = 0$ term of the exchange potential then becomes:

$$\beta = \frac{1}{\sqrt{\pi\gamma}} - \frac{4\pi}{\Omega} \sum_{\mathbf{G}} \frac{e^{-\gamma G^2}}{G^2} \tag{2.54}$$

This approach can also be applied to screened exchange formalism.

The CPMD package [152] will be used in this work. For further details on first-principles methods, we refer to [153].

Chapter 3

Structural models of the SiC/SiO$_2$ interface

In most of the theoretical work conducted so far on defects at the SiC/SiO$_2$ interface simplified model systems were used to address the interface. It is notoriously difficult to describe the interfacial bonding arrangement [154]. Theoretical work on defects then generally starts from crystalline structures [34, 35, 45, 70]. The only attempt of directly modeling the interface has been made by Knaup *et al*, who attached two SiO$_2$ layers to the $4H$(0001)-SiC substrate saturating all bonds at the interface [35]. This interface model was later also used by Wang *et al* [56]. While this model provides a useful bonding arrangement to terminate the $4H$(0001)-SiC substrate, the connection to an extended SiO$_2$ layer does not appear realistic. Indeed, the proposed connection results in an oxide density of $\sim$3.2 g/cm^3, significantly overestimating the density of amorphous SiO$_2$ as obtained from the melt (2.2 g/cm^3). Therefore, constructing a SiC/SiO$_2$ model interface with a realistic interfacial bond pattern would not only provide insight in the majority bonding arrangements near the interface, but also give a fresh view on the issue of near interface defects.

In this chapter, we first study for comparison the two components of the interface in their respective bulk phases, i.e. crystalline $4H$-SiC and amorphous SiO$_2$. As the description of band gaps and band offsets are essential for an accurate representation of defect levels, the band gaps of the bulk materials are studied with respect to the amount of exact exchange energy and the screening parameter incorporated in the calculations. We then report the generation of an abrupt model structure of the $4H$(0001)-SiC/SiO$_2$ interface which describes
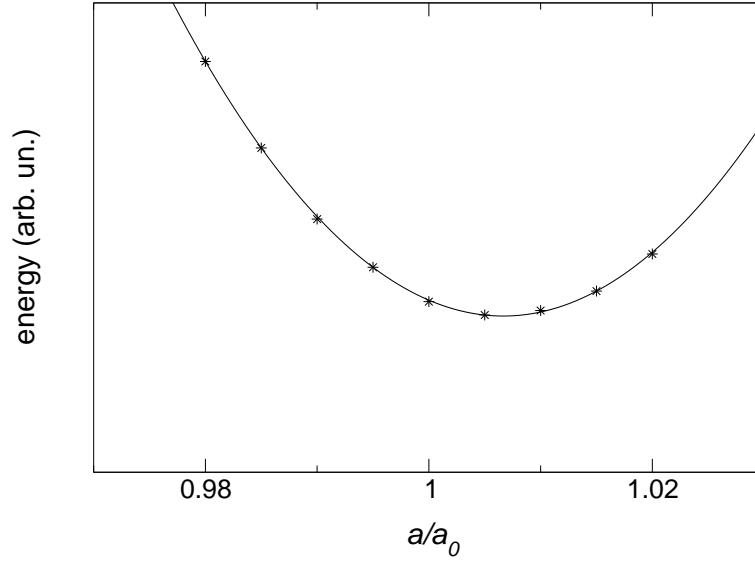
Figure 3.1: Determination of the $4H$-SiC equilibrium lattice constant a in PBE calculations [116] through the minimization of total energy vs lattice constant a. The stars represent the calculated energies, the solid line is a quadratic fit, and a_0 is the experimental equilibrium lattice constant.

the transition between crystalline SiC and amorphous SiO$_2$ without showing any coordination defect. The model interface is constructed through the sequential use of classical and *ab initio* simulation methods. The structural and electronic properties of the $4H$(0001)-SiC/SiO$_2$ interface are then examined. In particular, the band offsets are obtained through two different procedures: by evaluating the local density of states and by aligning the band extrema through the local electrostatic potential. Band offsets calculated with various functionals are compared to experimental values, and are found to be in very good agreement when the fraction α of Hartree-Fock exchange is tuned to reproduce the band gaps of the individual bulk materials and the band structures of the bulk components are then aligned to the electrostatic potential in the interface model.

3.1 The bulk models

3.1.1 The SiC bulk model

We modeled hexagonal $4H$-SiC using a 96-atom structure, taking the experimental value of 3.2714 for the c/a ratio [10]. The model contains 8 layers of alternating Si and C planes, and 3×4 atoms in the (0001) plane. To determine the equilibrium lattice constant a, we performed several relaxation calculations with the PBE functional [116] varying a around the experimental value. Figure 3.1 shows
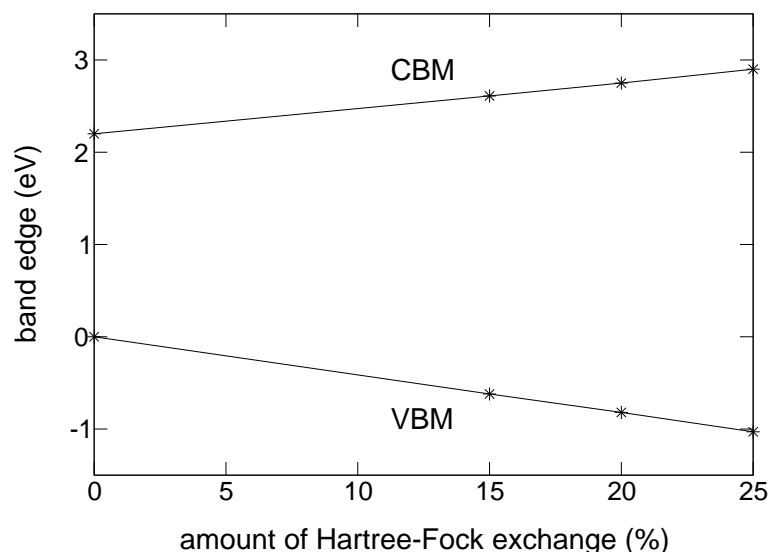
Figure 3.2: Band edges of bulk 4H-SiC vs amount of Hartree-Fock exchange included in the calculation. The positions of the band edges have been aligned to the average electrostatic potential. The solid line joins the stars representing the calculated band edges.

the calculated total energies vs the lattice constant a. A quadratic fit is applied to determine the equilibrium lattice constant a of 3.096 Å, in excellent agreement with the experimental value of 3.073 Å [10]. This value will also be used in subsequent hybrid functional calculations as the lattice parameters are not expected to vary significantly when incorporating a fraction of Hartree-Fock exchange. At variance with the very good agreement for the lattice constant, the corresponding Kohn-Sham band gap (2.2 eV) severely underestimates the experimental value (3.3 eV, Ref. [10]), as usual at this level of theory.

The hybrid density functional PBE0

One way to deal with the band gap problem common to standard density functionals is to use hybrid density functionals, which contain an explicit contribution of Hartree-Fock exchange. The PBE0 functional, in which 25% of the PBE exchange is replaced by Hartree-Fock exchange, has been proposed as a natural extension of PBE. However, the rationale for the optimum amount of Hartree-Fock exchange proposed by Perdew *et al.* [130] was based on a study of molecular systems so that this value may not be suitable for solid-state systems. We therefore studied the evolution of the valence and conduction bands in bulk SiC varying the amount of Hartree-Fock exchange in the calculations.

As shown in Fig. 3.2, the band gap of bulk 4H-SiC varies linearly with the
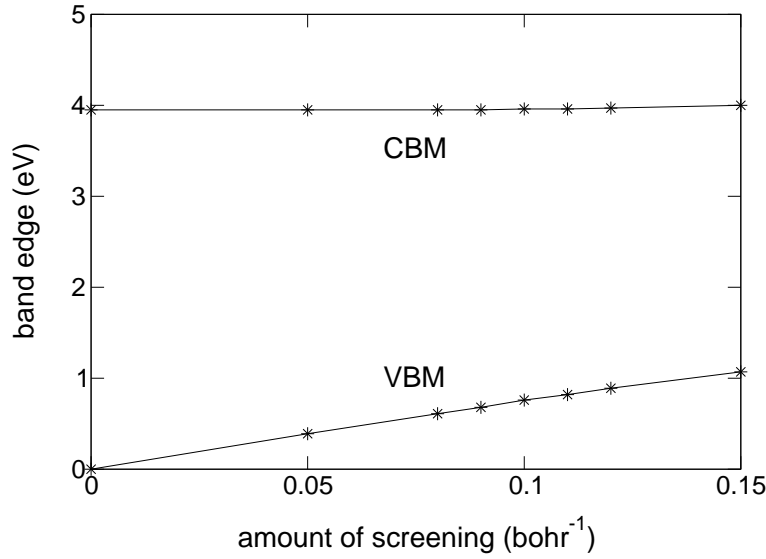
Figure 3.3: Band edges of bulk 4H-SiC vs inverse screening length included in the PBE0 (25% exact exchange) calculation. The positions of the band edges have been aligned to the average electrostatic potential. The solid line joins the stars representing the calculated band edges.

amount of Hartree-Fock exchange used in the calculation. However, the effect is not symmetric on the band edges: the valence band maximum is more strongly affected than the conduction band minimum. Using 25% of Hartree-Fock exchange overestimates the experimental band gap by 22%. This highlights the necessity of tuning the amount of Hartree-Fock exchange for each material. In the case of 4H-SiC, using 15% of Hartree-Fock exchange allows one to recover the experimental band gap (in the following, this hybrid functional will be referred to as PBE0[15]).

The screened hybrid density functional sPBE0

Hybrid density functional calculations are computationally expensive and become rapidly untractable in systems composed of a few hundred atoms. Screened exchange functionals were introduced to compute efficiently the long-range exchange interactions by shading their Hartree-Fock contributions. It was shown that in screened hydrid functionals a reduced k-point sampling compared to unscreened functionals is needed in the evaluation of the non-local exchange operator due to the presence of only short-range Hartree-Fock exchange [138]. We studied the effect of the amount of the screening length in the calculations on the evolution of the valence and conduction bands in bulk SiC. We performed calculations using a fixed 25% of Hartree-Fock exchange and varying the screening

length around a value used in a previous investigation [155] and close to values adopted in other hybrid density functional schemes [156].

In Fig. 3.3 the band gap is shown to decrease with increasing inverse screening length. However, a striking difference with Fig. 3.2 is the effect of the screening length on the description of the conduction band. The position of the conduction band does not vary with respect to the electrostatic potential and the change in the band gap is only due to the modification of the position of the valence band. Differences between screened and unscreened PBE0 calculations are also observed when calculating defect charge transition levels. Whereas the charge transition levels calculated at the PBE and PBE0 levels of theory locate at similar energy when aligned to the electrostatic potential, they noticeably differ when calculated with a screened Hartree-Fock exchange interaction [152]. We consider that this behavior is unphysical and attribute it to the neglect of the long-range exchange interaction in our formulation. Recently, Heyd *et al.* introduced a class of hybrid functionals in which the long-range exchange missed by the screening is accounted at the GGA level [144]. We expect that this formulation might restore the correct physical properties, but this conjecture has not further been pursued in this work. In this chapter, we present band offsets obtained with sPBE0 for comparison, but we will not use the screened Hartree-Fock interaction in the study of defects.

3.1.2 The SiO$_2$ bulk model

For amorphous SiO$_2$ used in subsequent band offset calculations and bulk oxide defect calculations, we took a 72-atom model obtained previously by *ab initio* molecular dynamics [157]. The model structure consists of a chemically ordered network of cornersharing tetrahedra at the experimental density of 2.2 g/cm^3. For this model, we obtained band gaps of 5.3, 7.1, 7.9, and 8.9 eV with the PBE functional, the sPBE0 functional, the PBE0 functional with 25% of Hartree-Fock exchange, and the PBE0 functional with 35% of Hartree-Fock exchange, respectively, to be compared with the experimental value of 8.9 eV. It should be noted that in the case of SiO$_2$, the 25% of Hartree-Fock exchange - optimum for molecular systems [130] - is not enough to recover the experimental band gap, as opposed to the case of SiC where this value already overestimates its experimental counterpart. Besides this difference, similar behaviours as in the case of bulk SiC were observed concerning the dependence of band gaps and band positions on the

amount of Hartree-Fock exchange and screening used in the hybrid functional.

3.2   Model generation of the SiC/SiO$_2$ interface

3.2.1   Methods

In this work, we used a sequence of different methodologies. To generate a model interface, we initially performed classical molecular dynamics with interatomic potentials derived from first-principles calculations [158]. For SiO$_2$, this method combines a low computational cost and an accurate structural description, allowing us to explore a large variety of bonding arrangements of the oxide in the vicinity of the interface.

To achieve structural properties of superior quality, we then turned to a density-functional approach in which the electronic structure is explicitly described. The exchange and correlation energy is given within the PBE generalized gradient approximation to density functional theory [116]. Core-valence interactions for all atoms were described by Troullier-Martins normconserving pseudopotentials [150] in the Kleinman-Bylander form [149]. For the valence electron wave functions, we used plane-wave basis sets with a cutoff energy of 70 Ry. The Brillouin zone was sampled at the Γ point. This approach also provides atomic forces that were used to carry out structural relaxations. We here used the implementation provided in the CPMD package [152, 159].

Standard density functionals, such as the PBE functional used here to refine the structural relaxation, fail in reproducing the experimental band gaps. One way to deal with this problem consists in using hybrid density functionals, which contain an explicit contribution of Hartree-Fock exchange. Recent studies showed that such functionals can lead to significant improvements in the description of band gaps of solids [135, 156]. In the present work, we consider hybrid density functionals, in which some amount of the PBE exchange interaction is replaced by either unscreened Hartree-Fock exchange (PBE0) [130] or screened Hartree-Fock exchange (sPBE0). In the case of the PBE0 functional, the integrable divergence was treated by adapting the scheme of Refs. [151] and [160] to Γ-point sampling. In the screened variant (sPBE0), we used a Coulomb operator of the form $\mathrm{erfc}(\alpha r)/r$, which avoids the divergence. This only accounts for the short-range Hartree-Fock exchange, in the same spirit of recent studies on condensed systems with hybrid functionals [156, 155]. In principle, the screening parame-

ter α could be used as a free parameter to tune some targeted physical property. Here, the effect of varying α was investigated in the case of bulk SiC, and was set to 0.1 bohr^{-1} for interface calculations as in a previous investigation [155] and close to values adopted in other hybrid density functional schemes [156]. Our scheme was obtained by further developing the implementation provided in CPMD [155].

3.2.2 Experimental data

While photoemission spectroscopy lacks sensitivity to study the interfacial defects contributing to the D_{it}, this technique is highly appropriate for providing information on majority bonding properties. The experimental literature has focused on the different oxidation states of silicon, which would directly bear implications on the degree of abruptness of the SiC/SiO₂ interface. When conventional oxidation procedures are applied to SiC, photoemission experiments generally show evidence for silicon oxycarbide species indicating the occurrence of an interfacial transition region with a thickness up to one nanometer [76, 161, 162]. Photoemission spectra have also been obtained for SiC/SiO₂ interfaces grown through the oxidation of the 3×3 (Refs. [85, 163, 164]) and $\sqrt{3}\times\sqrt{3}R30°$ (Refs. [49, 165]) reconstructed SiC(0001) surfaces. Upon oxidizing the SiC(0001)-3×3 surface, Amy *et al.* found a large variety of intermediate oxidation states [163]. However, starting from the same surface reconstruction, other authors found evidence for an abrupt interface with at most a single intermediate oxidation state between those of SiO₂ and SiC [85, 164]. The differences with respect to the earlier results of Amy *et al.* were explained by the silicon richness of the 3×3 reconstruction which would yield oxidation states typical of silicon surfaces upon initial oxidation [85, 86]. When the oxidation is started from the $\sqrt{3}\times\sqrt{3}R30°$ reconstructed SiC(0001) surface, the photoemission spectra can similarly be interpreted by invoking a single intermediate oxidation state [49, 86, 165]. Hence, photoemission investigations reveal that is possible to yield nearly abrupt interfaces by starting the oxidation from either 3×3 or $\sqrt{3}\times\sqrt{3}R30°$ reconstructed SiC(0001) surfaces [86, 85].

3.2.3 The SiC/SiO₂ model interface

In this work, we set out to generate a model structure of the interface between SiC(0001) and amorphous SiO₂. We here focus on the generation of an abrupt

interface model. Such an abrupt model provides a realistic description of the interfacial bonding pattern at SiC/SiO$_2$ interfaces obtained through the oxidation of 3×3 or $\sqrt{3}\times\sqrt{3}R30°$ reconstructed SiC(0001) surfaces [85, 86]. For SiC/SiO$_2$ interfaces obtained through standard processing procedures, an abrupt interface model lacks a transition region with silicon oxycarbide species and might therefore only be considered as a valid starting point for adressing interfacial bonding arrangements. Indeed, such an approach has successfully been applied to the Si(001)/SiO$_2$ interface which also presents a graded transition region [166, 167]. Furthermore, the availability of an atomistic model of the 4H-SiC/SiO$_2$ interface with good structural and electronic properties represents the first step towards the modeling of defect states at this interface. We determine interfacial bonding configurations using classical and density-functional molecular dynamics approaches in sequence. In the generated model, the structure evolves from crystalline SiC to amorphous SiO$_2$, without showing any coordination defect. Not only short-range structural parameters such as bond lengths and bond angles but also global properties such as the oxide density remain close to typical experimental values.

We modeled the $4H$(0001)-SiC substrate which is commonly used in SiC-based electronic devices. Our model substrate exposes a Si-terminated (0001)SiC surface and contains a periodic 3×4 repeat unit in the plane of the interface. The cell parameters were chosen to match the calculated equilibrium lattice constant a (Sec. 3.1.1). In order to find a suitable connection to amorphous SiO$_2$, it is necessary to account for a bond density reduction when going from SiC to SiO$_2$. In our unit cell, the SiC surface exposes 12 dangling bonds towards the oxide, but only 8 of these bonds can be saturated by SiO$_2$ at regular density [166].

To generate an atomistic model of the SiC/SiO$_2$ interface, we used a similar two-step procedure as applied previously to the Si(100)/SiO$_2$ interface [167]. In the first step, we used classical molecular dynamics to indentify suitable interfacial bonding patterns. The model was finally relaxed within a density-functional scheme to optimize structural parameters.

Using classical molecular dynamics, we started by searching for oxide structures satisfying structural constraints, as imposed by the bonds of the SiC substrate and by the lateral periodic boundary conditions of the simulation cell. We evolved Si and O atoms of the oxide at high temperatures (3000 K) in the neighborhood of the (0001)SiC surface and then slowly quenched the structure (at a rate of 15 K/ps) to low temperatures (300 K). Only the upper Si layer of the sub-
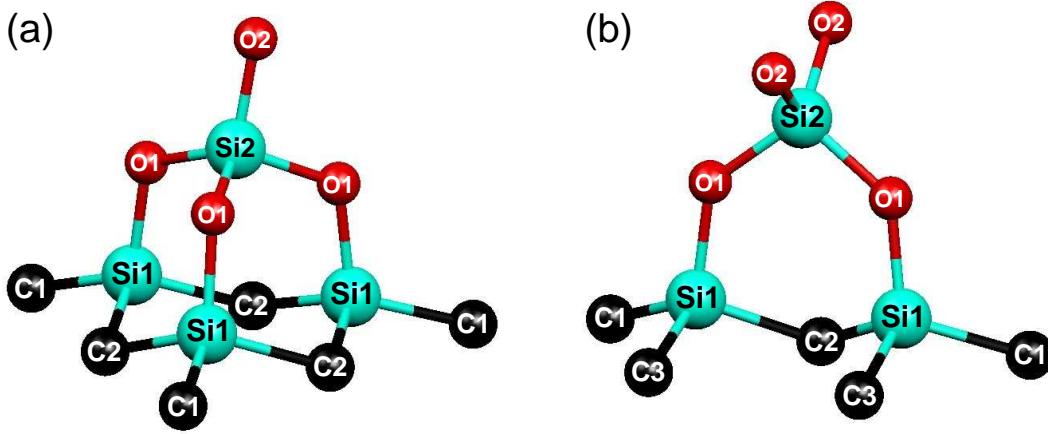
Figure 3.4:   (a) Interfacial oxide structure A involving three Si atoms of the SiC substrate and causing a bond reduction from 3 to 1. (b) Interfacial oxide structure B involving two Si atoms of the SiC substrate. No bond reduction is caused by this interfacial structure.

strate was included in the simulation cell with its Si atoms kept frozen. The structures generated in this way contained a large amount of Si-O-Si bridges, in which an O atom incorporates between two Si atoms of the surface template. These structures gave rise to unphysical bond lengths and bond angles at the interface, and occurred in this simulation because the directionality of the Si bonds is not accounted for by the adopted interatomic potentials [158].

The classical simulations also revealed two other interfacial oxide structures showing regular structural properties. These structures are illustrated in Fig. 3.4 and are denoted by A and B in the following. The interfacial structure A involves three Si atoms of the SiC substrate and accounts for a reduction of the number of exposed bonds from 3 to 1. The interfacial structure B involves only two Si atoms of the surface and does not give rise to any bond density reduction.

To connect our 3×4 SiC substrate to SiO₂, we chose to use twice structure A and three times structure B as shown in Fig. 3.5. By this construction all the exposed bonds of the (0001)SiC surface could be saturated without any coordination defect. Furthermore, we achieved the desired bond density reduction within the first few atomic layers of oxide. We note that the interface model proposed by Knaup *et al.* [34] only contains interfacial structures of type B, which do not yield any bond density reduction. The interfacial oxide density in their model is therefore correspondingly higher.

To further improve the structural properties of these very first oxide layers, we relaxed the atomic positions within the density-functional scheme [152]. For this
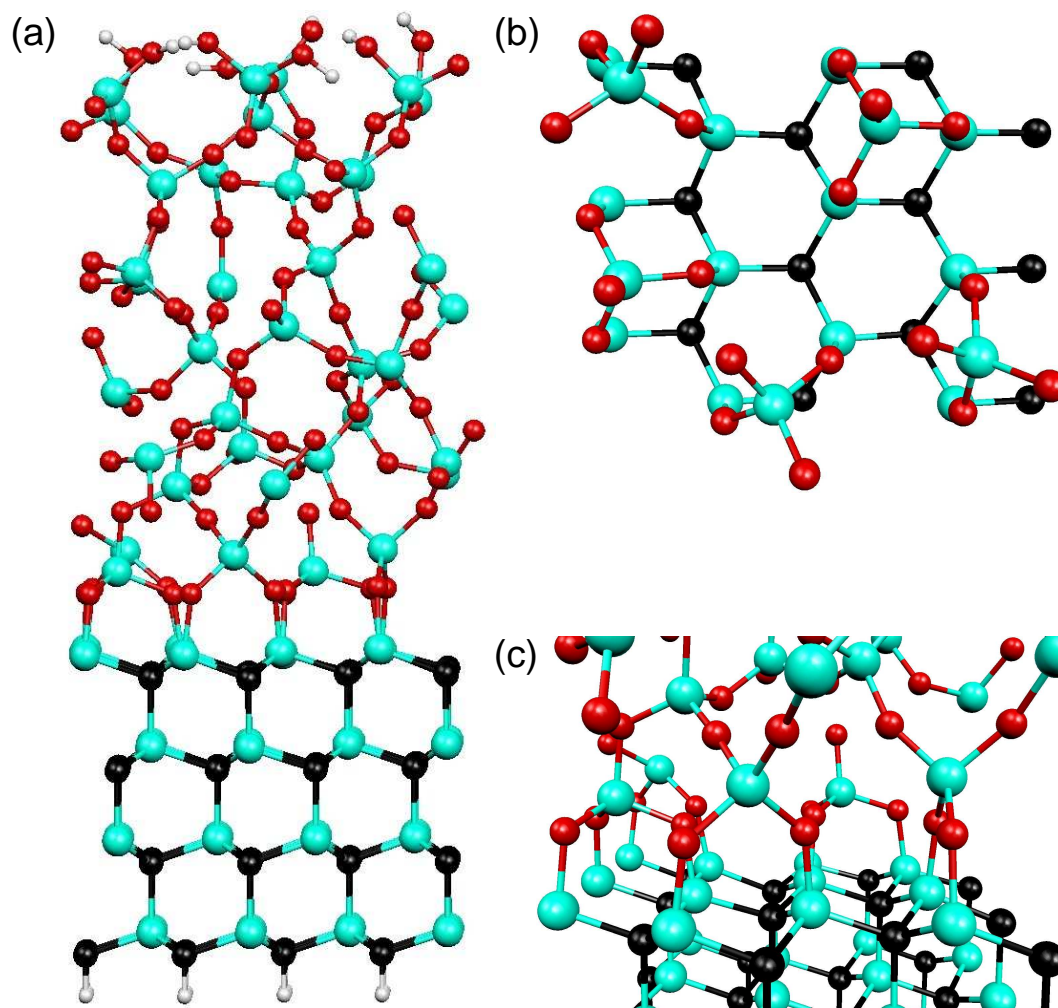
Figure 3.5: (a) Abrupt model structure obtained in this work for the 4H(0001)-SiC/SiO$_2$ interface, with detailed views of the transition region: (b) top view and (c) side view.

purpose the exposed bonds of the interface units were saturated with H atoms. The added H atoms were subsequently removed, and the resulting structure, consisting now of the substrate and the interfacial oxide structures, was used as a new template in a second set of classical simulations. In this case, Si and O atoms of the oxide were evolved in the neighborhood of this template, while the atoms in the template were kept frozen. Through a thermal annealing cycle, we obtained an interface model which continuously connects crystalline SiC to amorphous SiO$_2$. In order to optimize the structural properties, we performed a final relaxation step with the density-functional scheme [152]. Our final model (Fig. 3.5) contains a crystalline substrate with 8 planes of alternating Si and C atoms (8.2 Å thick) and an amorphous oxide with a thickness of 16 Å. The model is composed of 237 atoms, including 20 terminating H atoms.
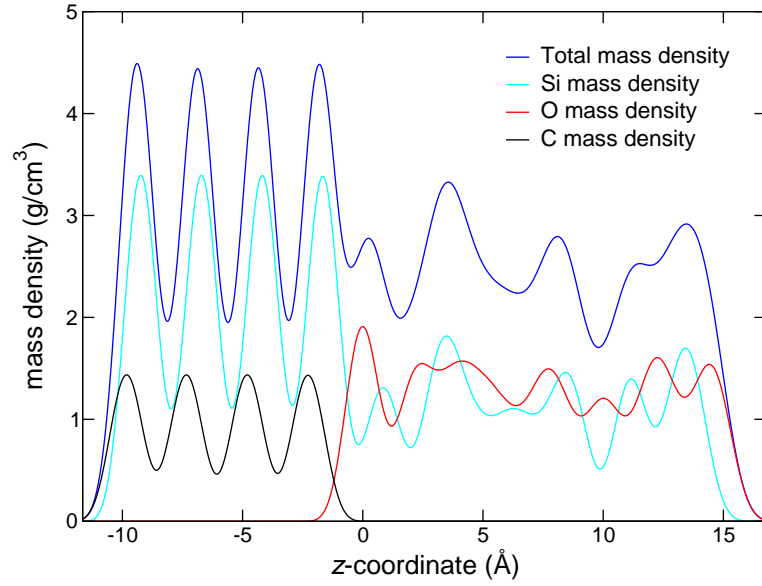
Figure 3.6: Mass density (blue) vs. a coordinate z evolving normal to the interface plane. Contributions from Si (cyan), O (red), and C atoms (black) are also indicated. The origin of the z coordinate corresponds to the first O layer of the oxide.

3.3   Structural properties

We give in this section the main structural parameters of the $4H$-SiC(0001)/SiO$_2$ interface generated in this work. In Fig. 3.6, we give the mass density for our model interface vs. a coordinate z evolving normal to the interface plane, together with partial contributions from C, Si, and O atoms. On the substrate side of the interface, one observes regular oscillations around an average value of 3.21 g/cm^3, close to the experimental value for the $4H$-SiC crystal (3.24 g/cm^3; Ref. [10]). On the SiO$_2$ side of the interface, the irregular fluctuations reflect the disordered nature of the oxide. In this region, we calculated an average mass density of 2.5 g/cm^3, slightly higher than the density of vitreous SiO$_2$ obtained from the melt (2.2 g/cm^3) but close to oxide densities near the interface found in models of the Si(100)/SiO$_2$ interface (2.3–2.4 g/cm^3) [167]. The transition between the two components occurs rather abruptly indicating that the densities of the interfacial and bulk oxides are similar.

Average structural parameters for bond lengths and bond angles of the oxide are given in Table 3.1. These parameters compare well with similar ones obtained for models of the Si(100)/SiO$_2$ interface [167]. Hence, the present model demonstrates that it is possible to construct oxides on SiC substrates of similar structural quality as on Si substrates, despite the different topological constraints.

This result qualitatively agrees with the experimental observation that the quality of oxides thermally grown on SiC is comparable in terms of breakdown electric field to that of SiO$_2$ grown on silicon [23].

The two interfacial oxide structures A and B (Fig. 3.4) share similar stuctural features. The bond lengths and bond angles given in Table 3.2 result from averages over geometrically equivalent features in our final relaxed model structure. Typical spreads are 0.01-0.03 Å for bond lenghts and 1.0-4.0° for bond angles. In structure A [Fig. 3.4(a)], SiC$_4$ tetrahedra of the substrate bind to SiO$_4$ tetrahedra of the oxide keeping the same orientation. The regular tetrahedra in SiC feature average Si-C bond lengths of 1.90 Å, 14% larger than the average Si-O bond length (1.64 Å) in SiO$_2$. This difference introduces a slight departure of the C-Si-O angles from the tetrahedral angle of 109.5°. For the Si-O-Si angle closest to the substrate, we found a value of 118.3°. For C atoms [C2 in Fig. 3.4(a)] connected to two substrate Si atoms of structure A, the C-Si-O angle is 104.4°. For C atoms [C1 in Fig. 3.4(a)] connected to only one of such Si atoms, the corresponding C-Si-O angle is 113.9°. Si-O bond lengths involving Si atoms of the substrate feature slightly longer bond lengths than in the oxide. This effect is similar to the elongated Si-O bond lengths found in the suboxide at the Si(100)/SiO$_2$ interface as a consequence of the modified electronegativity of the Si atoms [168].

Overall, the bonding properties characteristic of the interfacial structure B [Fig. 3.4(b)] are very similar to those of structure A. For structure B, we found Si-O bond lengths involving substrate Si atoms of 1.68 Å, very close to the corresponding values found for structure A (1.66 Å). We observed three different C-Si-O angles, 104.4°, 111.3°, and 113.4°, corresponding to the three nonequivalent C atoms in structure B. For the oxygen atoms closest to the substrate, we obtained Si-O-Si angles of 133.8°.

Table 3.1: Mean (μ) and standard deviation (σ) of bond-length and bond-angle distributions in the oxide for the present 4H(0001)-SiC/SiO$_2$ model interface.

	μ	σ
Si-O (Å)	1.64	0.02
$\angle$ Si-O-Si	137.4°	14.22°
$\angle$ O-Si-O	109.5°	5.5°

Table 3.2:   Mean (μ) and standard deviation (σ) of bond-length and bond-angle distributions in structures A and B. Notation of atoms corresponds to Fig. 3.4.

	Structure A		Structure B	
	μ	σ	μ	σ
Si1-O1 (Å)	1.66	0.03	1.68	0.02
Si2-O1 (Å)	1.65	0.01	1.66	0.01
$\angle$ C1-Si1-O1	113.9°	1.7°	113.4°	4.0°
$\angle$ C2-Si1-O1	104.4°	2.3°	104.4°	1.0°
$\angle$ Si1-O1-Si2	118.3°	2.0°	133.8°	2.8°
$\angle$ C3-Si1-O1	–	–	111.3°	2.7°

3.4   Electronic structure

3.4.1   Local density of states

We study the electronic properties through the planar averaged local electronic density of states:

$$D(z; \epsilon) = 2 \sum_n |\langle z | \psi_n \rangle|^2 \delta(\epsilon - \epsilon_n), \tag{3.1}$$

where z indicates a coordinate along the interface normal, $|\langle z | \psi_n \rangle|^2$ corresponds to the electron density integrated in xy planes, the factor of 2 accounts for the spin degeneracy, and ψ_n are the Kohn-Sham eigenstates of energy ϵ_n. In the calculations, the Dirac delta functions in Eq. 3.1 were replaced by Gaussian functions with a standard deviation of 0.02 eV.

Figure 3.7 shows the total electronic density of states of our model $4H(0001)$-SiC/SiO$_2$ interface obtained with the sPBE0 functional. We also give the corresponding local electronic density of states decomposed in Si, C, and O contributions in the SiO$_2$, the interfacial, and the SiC regions. The atomic decomposition is achieved via projections of the electron wave functions onto the atomic orbitals of the atoms situated in each considered layer. In the SiC, because of the higher electronegativity of C with respect to Si, the valence states have predominantly C character, while the conduction bands carry a higher Si weight. In the interfacial layer, this feature persists because the highest valence and lowest conduction states are still determined by the SiC. Furthermore, we observe that the lower
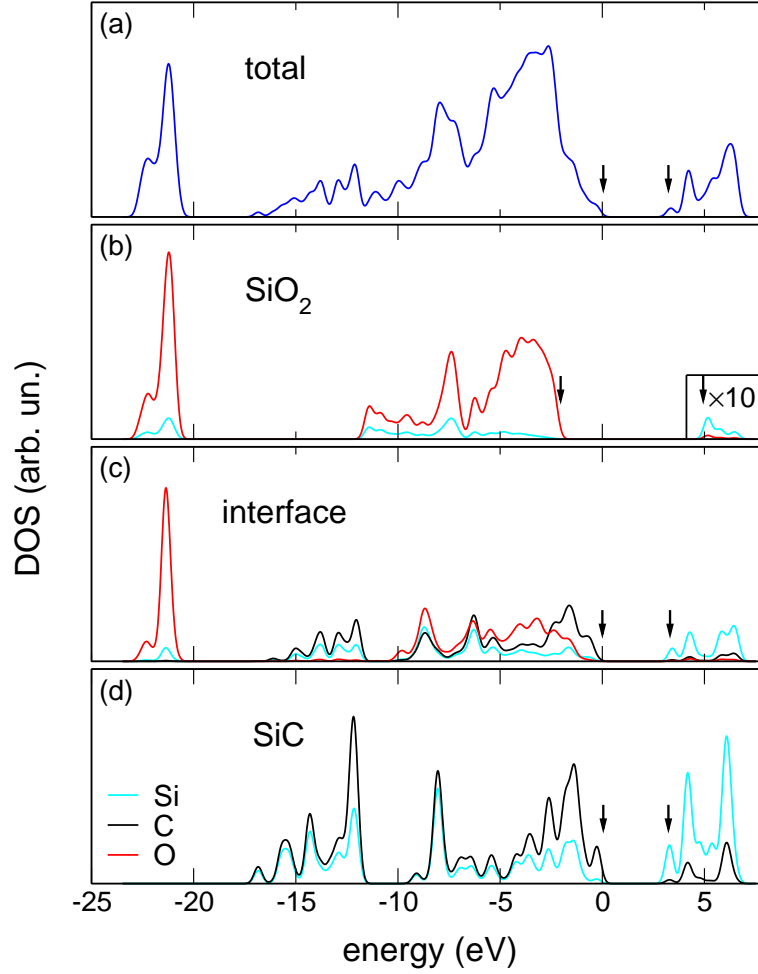
Figure 3.7: (a) Total electronic density of states (DOS) of our model $4H$(0001)-SiC/SiO$_2$ interface calculated with the sPBE0 functional, and corresponding local electronic density of states decomposed in Si (cyan), C (black), and O (red) contributions for 5-Å-thick layers situated (b) in the SiO$_2$ (c) at the interface (centered at $z = 0$) and (d) in the SiC. The origin of the energy scale corresponds to the Fermi level. The positions of the highest occupied and lowest unoccupied states are indicated by arrows.

part of the valence band, extending from -10 to -2 eV, shows significant contributions from all atomic species, because electronic states are found at these energies in both the SiC and SiO$_2$. The two lower bands, from -23 to 20 eV and from -17 to -12 eV, do not carry such a mixed character and correspond to SiO$_2$ (O 2s) and SiC bands, respectively. In the oxide layer, we recover the electronic density of states of amorphous SiO$_2$ [157, 169]. The highest valence states correspond to O states, while the conduction states are predominantly Si-related, in accord with the relative electronegativities of O and Si.
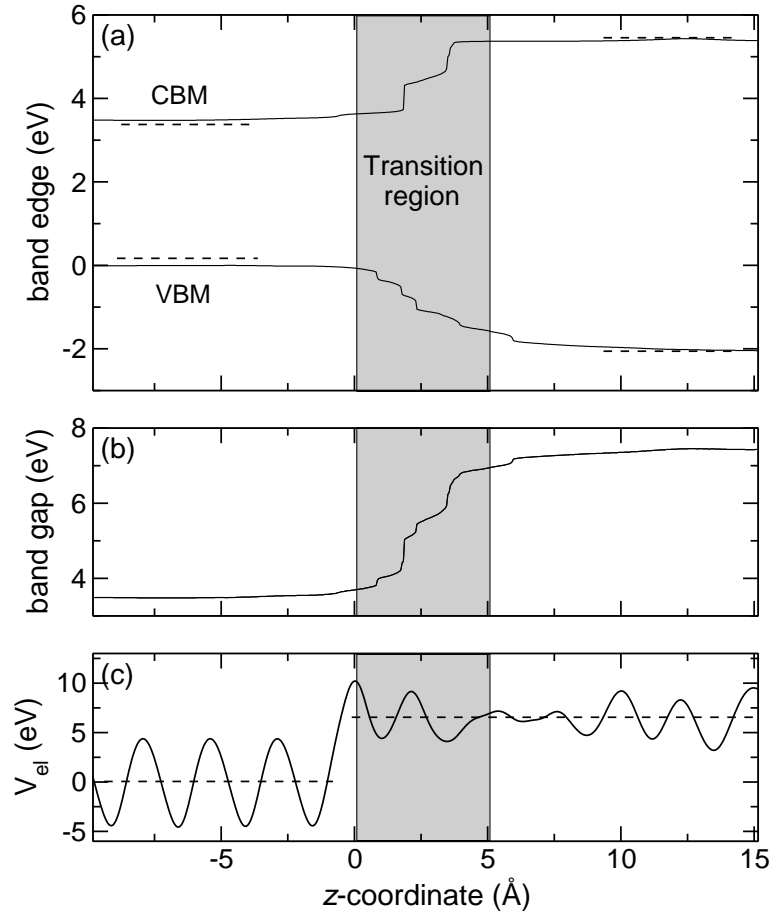
Figure 3.8: Evolution of the conduction band minimum (CBM), valence band maximum (VBM), band gap, and local electrostatic potential across the interface in our $4H(0001)$-SiC/SiO$_2$ model, calculated at the sPBE0 level of theory. The shaded area corresponds to the first two layers of SiO$_4$ tetrahedra from the interface. Dashed lines correspond to VBM and CBM obtained from bulk calculations of SiC and SiO$_2$ and aligned at the interface through the average electrostatic potential.

3.4.2   Evolution of band edges across the interface

The determination of the local band edges is nontrivial when one of the interface components is an amorphous material [170, 171]. From the local electronic density of states $D(z; \epsilon)$, we obtained the evolution of the valence band maximum (VBM) and the conduction band minimum (CBM) across the interface as follows. For every value of z, we determined the local band edges by requiring that the number of states falling between the cell midgap and the band edge equals a threshold value of 0.03 states/Å^3 [172]. The threshold value was determined by imposing that the band gap in bulk SiC is accurately recovered. Using a model of amorphous SiO$_2$ [157], we checked that this threshold value results in a band gap differing by less than 0.1 eV from the separation between the Kohn-Sham

energies of the highest occupied and lowest unoccupied energy levels.

In Fig. 3.8, we report sPBE0 results for the evolution of the CBM, VBM, band gap, and local electrostatic potential across the interface in our $4H(0001)$-SiC/SiO$_2$ model.[1] The band gap deep inside each component of the interface is found to be relatively constant. In the SiO$_2$ layer, the band gap derived from the local density of states (7.0 eV) agrees well with the band gap (7.1 eV) calculated in Sec. 3.1.2 for our reference model of amorphous SiO$_2$. In the SiC substrate, we calculated a band gap of 3.5 eV, slightly larger than for our bulk $4H$-SiC reference (3.2 eV, cf. Sec. 3.1.1). This effect should be ascribed to the quantum confinement of the electron states in the SiC semiconductor layer, as found previously for silicon slabs [173, 174]. From SiC to SiO$_2$, we record a progressive increase of the electronic band gap over a spatial region of 5 Å, corresponding to the first two layers of SiO$_4$ tetrahedra (cf. Fig. 3.8). This extent is in excellent accord with the experimental estimate of 5 Å, derived from internal photoemission data [175]. A similar transition region for the electronic properties has previously also been found for the Si/SiO$_2$ interface [171, 172]. Since our model interface is abrupt at the atomic scale, this extent should be considered as the minimal one that is required for recovering the band gap of bulk SiO$_2$. Thus, from our results it appears that the internal photoemission measurements are consistent with an atomically abrupt interface.

3.4.3 Band offsets

Because of the quantum confinement effect in the SiC layer, the SiC band edges determined from the local density of states are biased. To determine reliable band offsets, we therefore had recourse to the method proposed by Van de Walle and Martin [176]. This method consists in determining the offset of the local electrostatic potential across the interface [176]. Band offsets are then obtained by determining the positions of the band edges with respect to the local electrostatic potential in bulk calculations of the two interface components. For a crystalline material, this method can thus reliably be used to position the band edges with respect to the electrostatic potential at the interface. However, in the case of an amorphous component, application of this method faces difficulties associated

---

[1]In the vacuum region of the cell, a non-zero electrostatic potential due to the presence of the natural dipole formed by the finite interface structure in the cell and the artificial periodic boundary conditions can be seen. However, the corresponding electric field remains small in the SiO$_2$ oxide and undetectable in the SiC substrate, which renders the use of dipole-correction methods optional.

with the determination of the average electrostatic potential and with the choice of the bulk reference model. In our application to the SiC/SiO$_2$ interface, this method will thus accurately provide the positions of the SiC band edges. For the band edges of the SiO$_2$ component, the method is expected to be subject to larger errors. However, in the latter case, the band edges can reliably be obtained from the local density of states.

Figure 3.8 (c) shows the planar-averaged electrostatic potential V_{el} across the interface in our model $4H$(0001)-SiC/SiO$_2$. In the SiC, V_{el} shows regular oscillations corresponding to the atomic planes and the average value can accurately be determined. In the SiO$_2$, the amorphous nature of the material gives rise to irregular fluctuations and the determined average value therefore suffers from the statistical error. Through bulk calculations for the two reference components of our interface, we are able to position their band edges with respect to the average values of V_{el}. In Fig. 3.8(a), the levels determined in this way are compared with the CBM and VBM derived from the local density of states. In the SiC, the band edges are found to fall in between the extrema derived from the local density of states. This is consistent with the quantum confinement effect discussed above. In the SiO$_2$, the band edges fall close to those obtained from the local density of states, despite the errors due to the limited statistics. The agreement between the positions of the oxide band edges obtained with the two alternative approaches supports the consistency of the applied procedures.

By aligning band extrema to the local electrostatic potential V_{el} [176], we obtain valence and conduction band offsets of 2.2 and 1.7 eV, respectively, for sPBE0 calculations. These values are considerably smaller than the respective experimentally determined offsets of 2.9 and 2.7 eV. However, the calculations correctly reproduce the experimental trend yielding a higher offset for the valence band than for the conduction band. Furthermore, the agreement between calculated and measured band offsets improves when expressed with respect to the oxide band gap. For these ratios, we obtained 31% and 24% for valence and conduction bands, to be compared with the experimental ratios of 33% and 30%, respectively.

Table 3.3 summarizes our results for the band offsets at the $4H$(0001)-SiC/SiO$_2$ as obtained with the two procedures discussed above and with the four density functionals considered in this work. For all fonctionals, the comparison between the band offsets obtained through the local DOS and through the alignment with respect to the local electrostatic potential is similar. Within the scheme based on the local DOS, the SiO$_2$ band gap is always found to be well described while

Table 3.3: Calculated PBE, PBE0, and sPBE0 band gaps and band offsets (in units of eV) for our model of the $4H(0001)$-SiC/SiO$_2$ interface, compared to corresponding experimental data [38]. Band gaps and band offsets were obtained following two different procedures, either through the local density of states (DOS) or through the offset of the local electrostatic potential ($\Delta V_{\rm el}$) [176]. In parentheses, the band offsets are expressed as ratios with respect to the SiO$_2$ band gap. Results obtained with the mixed scheme (see text) are also given.

	$E_{\rm gap}^{\rm SiC}$	$E_{\rm gap}^{\rm SiO_2}$	$\Delta E_{\rm v}$	$\Delta E_{\rm c}$
Through local DOS:				
PBE	2.5	5.3	1.4 (25%)	1.4 (25%)
PBE0	4.2	7.7	2.0 (26%)	1.5 (19%)
sPBE0	3.5	7.0	2.0 (29%)	1.5 (21%)
PBE0^{15}	3.6	6.8	1.8 (26%)	1.4 (21%)
Through $\Delta V_{\rm el}$:				
PBE	2.2	5.3	1.5 (28%)	1.6 (30%)
PBE0	3.9	7.9	2.2 (28%)	1.8 (23%)
sPBE0	3.2	7.1	2.2 (31%)	1.7 (24%)
PBE0^{15}	3.3	6.9	2.0 (29%)	1.6 (23%)
Mixed scheme	3.3	8.9	3.0 (34%)	2.6 (29%)
Expt.	3.3	8.9	2.9 (33%)	2.7 (30%)

the SiC is overestimated by 0.2-0.3 eV, due to the quantum confinement effect of the thin substrate. The comparison between the band offsets calculated with the various functionals and the corresponding experimental values is less trivial. The PBE band offsets are not only significantly smaller than the experimental values but also fail in reproducing the relative size of conduction and valence band offsets. The use of the PBE0 functionals corrects the relative size of these offsets and leads to an improved valence band offset. However, the conduction band offset deteriorates because of the large overestimation of the SiC band gap. The comparison in Table 3.3 shows that the best agreement with experiment when using only one Hartree-Fock exchange parameter throughout all calculations is achieved with the sPBE0 functional, not only for the absolute band offsets but also for their ratios with respect to the oxide band gap. This good agreement
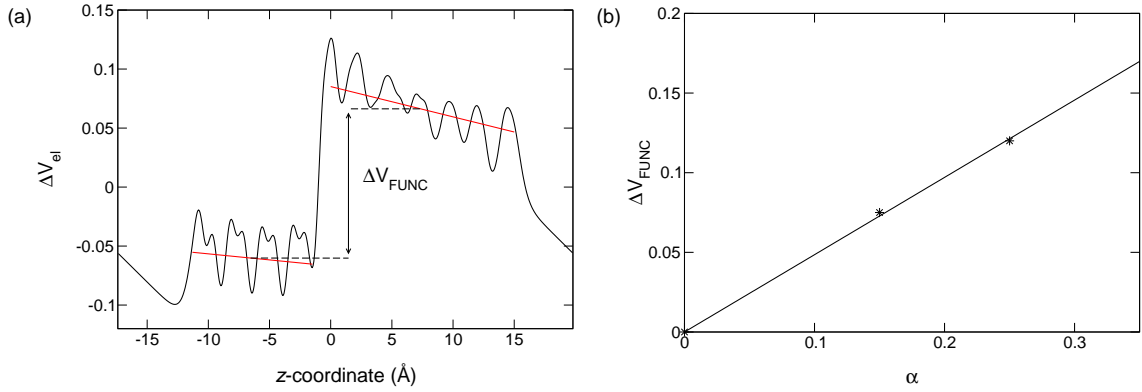
Figure 3.9: (a) Difference in the evolution of the local electrostatic potential at the SiC/SiO$_2$ interface between the PBE0 calculation with 25% of Hartree-Fock exchange and the PBE calculation. (b) Difference in the average electrostatic potential between the SiC substrate and the SiO$_2$ oxide for PBE and PBE0 calculations with two different values of Hartree-Fock exchange (α=15% and α=35%). A linear extrapolation is also plotted.

should be attributed to the good description of the SiC band gap achieved with the sPBE0 functional. However, the band offsets obtained with the sPBE0 functional still underestimate their experimental counterparts by ~1 eV.

To determine the band offsets accurately, we turn to another scheme which also relies on the alignment of band extrema through the electrostatic potential. However, in this scheme, we use a tuned hybrid functional to recover the experimental band gap for the bulk models of the two interface components. As shown in Sec. 3.1, the use of 15% and 35% of Hartree-Fock exchange allows one to recover the experimental band gaps of bulk 4H-SiC and SiO$_2$, respectively. In each bulk model, the band extrema can be located with respect to the electrostatic potential. In the crystalline SiC bulk model, we considered the average electrostatic potential, as seen in Fig. 3.8 (c). In the amorphous SiO$_2$, the determination of the average electrostatic potential is not so trivial and subject to errors because of the important fluctuations. The band extrema are therefore located with respect to the oxygen 2s states which are only little affected by the local environment. The scheme then assumes that the electrostatic potential across the interface does not undergo significant varaiations when different amounts of Hartree-Fock exchange are used.

Figure 3.9 (a) shows the difference in the electrostatic potential of the interface structure between the PBE0 calculation involving 25% of Hartree-Fock exchange and the PBE calculation. In the vaccuum region ($z < -13$ Å and $z >16$ Å), a non-zero electrostatic potential due to the presence of different dipoles in the PBE and

PBE0 calculations can be observed. This causes the bending of the electrostatic potential in the two interface materials. However, the determination of the difference in the average electrostatic potential between the SiC substrate and the SiO$_2$ oxide is subject to minor errors and can be easily determined without applying further dipole-correction methods. The difference in the average electrostatic potential between the SiC substrate and the SiO$_2$ oxide for PBE and PBE0 calculations involving different values of Hartree-Fock exchange is plotted in Fig. 3.9 (b). The linear interpolation allows us to estimate the error made when aligning the bulk band extrema of SiC (calculated with 15% of Hartree-Fock exchange) and SiO$_2$ (calculated with 35% of Hartree-Fock exchange) through the electrostatic potential in the interface model to be about 0.1 eV. This method can then be used reliably and lead to valence band and conduction offsets of 3.0 and 2.6 eV, respectively, in excellent agreement with their experimental counterparts of 2.9 and 2.7 eV. This new scheme is particularly useful in the study of defects for which the alignment to the band edges is a critical issue.

3.5 Conclusions

In view of further studies on near-interface defects, we here set out to generate a model structure providing a realistic description of the majority bonding arrangements at the $4H$(0001)-SiC/SiO$_2$ interface. In this work we chose to consider an atomically abrupt interface. While such a model does not show interfacial silicon oxycarbide species as found for SiC/SiO$_2$ interfaces grown by standard processing procedures [76, 161, 162], it nevertheless offers a realistic description of SiC/SiO$_2$ interfaces obtained through the oxidation of reconstructed SiC(0001) surfaces [85, 86]. Furthermore, we aimed at reproducing the amorphous nature of the oxide as well as its typical density. We succeeded in these intents by sequentially using classical and *ab initio* simulation methods. Classical molecular dynamics allowed us to identify two typical interfacial units consisting of SiO$_4$ connected to the (0001)SiC substrate. We incorporated these units at the interface in appropriate amounts to achieve the required bond density reduction when going from the substrate to the oxide. A connection to bulk amorphous SiO$_2$ was then achieved through classical molecular dynamics. A structural relaxation within a density-functional scheme resulted in a model interface with good structural parameters.

We then investigated the electronic properties of the generated model interface

using hybrid density functionals, which incorporate a fraction of the Hartree-Fock exchange interaction. The use of such functionals is motivated by the necessity of accurately describing band gaps and band offsets, which are known to be poorly described by standard density functional schemes. Indeed, the identification of typical near interface defects is expected to mainly rest on the position of energy levels with respect to the relevant band edges.

We studied the evolution of the valence and conduction band edges across the interface through the local density of states averaged in planes parallel to the interface. For our abrupt model interface, the band gap of the oxide is already fully recovered at a distance of 5 Å from the interface. This extent is in excellent agreement with internal photoemission measurements, thereby providing support for the abruptness of the actual $4H(0001)$-SiC/SiO$_2$ interface. The evolution of the local density of states across the interface was also used for the determination of band offsets. To overcome the quantum confinement effect of the electronic states in the thin SiC substrate, we also determined more reliable band offsets by aligning the band extrema through the local electrostatic potential at the interface. Using a hybrid functional with a screened Coulomb potential in the Hartree-Fock exchange term, we obtained valence and conduction band offsets that underestimate their experimental counterparts by $\sim$30%, but agree with measured values within only a few percent when expressed with respect to the oxide band gap. Absolute values in very good agreement with experiment were then obtained through the use of a scheme in which the band extrema of each of the two bulk components of the interface are first calculated through hybrid calculations incorporating the appropriate amount of Hartree-Fock exchange to recover experimental band gaps. The band extrema are then aligned to the electrostatic potential of the interface model, leading to band offsets that agree with their experimental counterparts within 0.1 eV.

In conclusion, we found that the generated model structure of the $4H(0001)$-SiC/SiO$_2$ interface features realistic properties both from the structural and electronic standpoints. In particular, the description of band gaps and band offsets appears to be very reliable, so that the identification of defect states through their energy levels can be envisaged. This assessment constitutes the first step towards the use of a realistic model structure to study defects at $4H(0001)$-SiC/SiO$_2$ interfaces.

Chapter 4

Defects at the SiC/SiO$_2$ interface

The large density of defect states (D_{it}) encountered at the interface between 4H-SiC and its native oxide SiO$_2$ has so far hindered the development of SiC-based devices [23]. In particular, the D_{it} shows large values just below the conduction band edge of 4H-SiC [23, 24, 27, 31], suggesting that the defects responsible for the electrical degradation situate in this energy range. The nature of these defects is at present not well understood.

Density-functional calculations have been used to investigate several defect candidates at the SiC/SiO$_2$ interface [34, 35, 56]. In particular, Knaup *et al.* calculated energy levels for several carbon related defects and found them to lie in the mid and low part of the SiC band gap, providing an interpretation for features of the D_{it} in this energy range [35]. Wang *et al.* proposed a different defect structure involving two carbon interstitials on the substrate side and exhibiting correlated carbon dangling bonds, but its energy levels were found to lie about 1 eV below the conduction band [56]. More recently, Deák *et al.* considered a defect consisting in two bonded carbon atoms substituting two nearby oxygen atoms of the oxide. Its calculated acceptor level fell in correspondence of the SiC conduction band edge, providing an interpretation for the sharp peak below the SiC conduction band [70].

The alignment of defect levels with respect to the relevant band edges at a semiconductor-oxide interface is a critical issue. In the calculations of Knaup *et al.* and Deák *et al.*, a sequential approach involving both bulk and interface calculations was used [35]. A legitimate question arises whether the resulting alignments would be modified in case the defects were directly generated at the model interface. In the calculation of Wang *et al.* [56], an interface structure was used in which the oxide density significantly exceeds that of typical values

for SiO$_2$. This might affect the local strain at the interface and consequently the energy levels of near-interface defects.

In this chapter, we investigate defect levels at the $4H$-SiC(0001)/SiO$_2$ interface using spin-polarized hybrid density functionals [116, 130]. We take under consideration several carbon-related defects previously proposed in the literature [35, 56, 70] and suggested by experiment [28, 36]. Interfacial defects are first generated in a model structure describing the transition between crystalline SiC and amorphous SiO$_2$. The Kohn-Sham energy levels associated with the defects are aligned with respect to the SiC band edge. This approach constitutes a first step towards the identification of possible candidates for the high density of defect states. It also provides a useful comparison with the calculations of defects identified in the literature through this method. Moreover, the charge transition levels cannot directly be determined at the interface as charged interface calculations in periodic slab systems are difficult to treat. Therefore, charge transition levels of potential contributors to the D_{it} in the upper SiC band gap are calculated in the appropriate bulk models. The relaxation and polarization effects due to the interface are then taken into account to evaluate the location of the charge transition levels at the interface. Intrinsic defects in the oxide as well as oxygen-related defects at the interface are also considered. Finally, the passivation of the C-C pair defect is investigated.

4.1   Methods

4.1.1   Computational details

The electronic structure of the defects is described at two levels of theory using the PBE functional [116] and a hybrid functional incorporating a fraction of Hartree-Fock exchange [130]. The PBE functional used here to carry out structural relaxations fails in reproducing the experimental band gaps. As shown in Chap. 3, the PBE0 functional leads to significant improvement in the description of band gaps and therefore allows useful comparison with experiment. Interface and bulk SiC calculations are carried out using 15% of Hartree-Fock exchange which leads to an accurate description of the $4H$-SiC experimental band gap. Regarding the study of intrinsic defects of the oxide, 35% of Hartree-Fock exchange is included in the calculations for an accurate description of the SiO$_2$ band gap. For notation convenience, the amount of included Hartree-Fock exchange will be

denoted in the superscript of the functional acronym, e.g. PBE0[15] or PBE0[35].

Core-valence interactions for all atoms are described by Troullier-Martins normconserving pseudopotentials [150] in the Kleinman-Bylander form [149]. For the valence electron wave functions, we use plane-wave basis sets with a cutoff energy of 70 Ry. The Brillouin zone is sampled at the Γ point. This approach also provides atomic forces that are used to carry out structural relaxations. We here use the implementation provided in the CPMD package [152, 159].

4.1.2   Defects generation and alignment

The modeling of an atomistic model of the $4H$-SiC/SiO$_2$ interface with good structural and electronic properties has been described in Chap. 3. Most of the defects studied in this work are generated directly in this model interface. This procedure appears essential to capture specific interface related effects, such as structural relaxation and bonding rearrangement. For intrinsic defects and determination of accurate charge transition levels, bulk calculations are also carried out (cf. Sec. 3.1). For each defect, full relaxation is carried out at the PBE level of theory. The electronic structure is then described at the PBE and PBE0[15] levels. Hybrid functional calculations are computationally expensive which makes geometry optimization at the PBE0 level of theory impractical. The PBE0 electronic descriptions are then based on structures relaxed at the PBE level of theory.

As shown in Sec. 3.4.3, the SiC band edges determined from the local density of states are biased because of quantum confinement effects due to the finite thickness of the substrate [173]. Hence, the band edges of $4H$-SiC are also determined by aligning the bulk band extrema through the local electrostatic potential [176]. The band edges determined in the latter way serve as reference for the defect levels at the interface and in bulk SiC. For a crystalline material, this method can reliably be used to position the band edges with respect to the electrostaic potential. However, in the case of an amorphous component, application of this method faces difficulties associated with the determination of the average electrostatic potential. For SiO$_2$, the oxygen $2s$ states deep in energy and unaffected by local environment are used as the reference to which the defect levels are aligned.
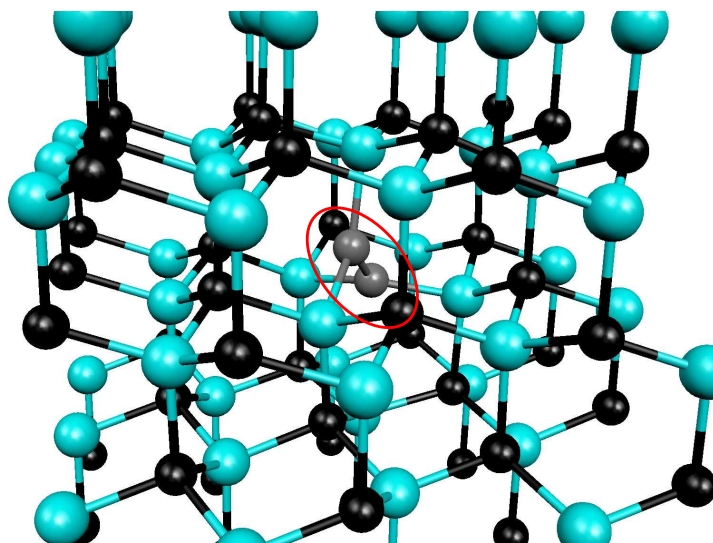
Figure 4.1: Carbon interstitial at a carbon site in a 96 atom model of bulk 4H-SiC. The red ellipse circles the resulting two sp^2 hybridized carbon atoms represented in grey.

4.2 Carbon-related defects

Conventional oxidation of SiC results in a much higher defect density of states at SiC/SiO$_2$ interfaces than at Si/SiO$_2$ interfaces. The most obvious difference in the oxidation of the two semiconductors is that the key atomic-scale oxidation step of SiC entails carbon release. The incomplete removal of carbon can lead to various forms of carbon-related defects in either the near interface SiC substrate or the SiO$_2$ oxide. We start our study of carbon-related defects with the most simple one, i.e. the single carbon interstitial.

4.2.1 Single carbon interstitial in bulk SiC

We first study the single carbon interstitial in bulk SiC. While interface specific features are omitted, this provides an adequate starting step to point out the major characteristics of the single carbon interstitial. We use the 96 atom model of bulk 4H-SiC introduced in Sec. 3.1.1, and introduce a carbon atom at a C lattice site. Upon full relaxation, one notices that structural adjustments mainly occur in the immediate vicinity of the two neighbor carbons. The volume of the tetrahedron defined by the four silicon atoms enclosing the C-C pair increases by 10% upon insertion of the additional carbon atom. With a value of 1.79 Å, the average Si-C distance involving one of the two C atoms of the pair decreases by 6% compared to bulk SiC. The average Si-C-Si angle is 138.4° ($\pm$1.4°) and the C-
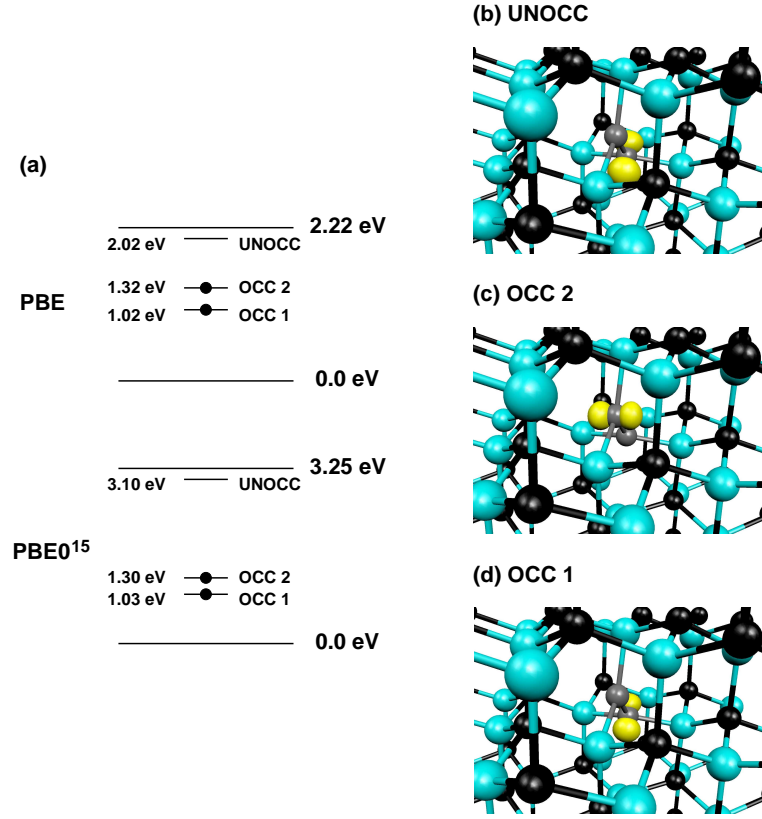
Figure 4.2: (a) Carbon-related defect levels in the $4H$-SiC band gap, calculated within the PBE and PBE0[15] scheme. The occupied levels are denoted by a black dot. The top of the valence band is taken as the origin. (b)-(d) Isosurfaces of the density of the defect states in the $4H$-SiC band gap as identified in (a).

C bond is 1.37 Å. Finally, the angle between the planes of the two sp^2 hybridized carbons is 89.3°, and the average dihedral angle Si-C-C-Si involving the C-C pair is 85.3° (with a standard deviation of 2.1°).

We then study the electronic structure of the carbon interstitial defect using a spin-polarized density-functional approach at the PBE [116] and PBE0 [130] levels of theory. The Kohn-Sham levels are aligned to the band edges of the defect-free bulk $4H$-SiC model through the local electrostatic potential. Figure 4.2 shows three defect levels located in the band gap of SiC both in the PBE and the PBE0[15] calculations. Two levels located at or below midgap in the PBE and PBE0[15] calculations, respectively, are occupied while one defect located just below the conduction band is unoccupied. A first observation when comparing the description of the defect levels in PBE and PBE0[15] calculations is the very good agreement of the positions of the occupied levels with respect to the valence band. Similarly, very good agreement for the unoccupied level is observed when

referred to the conduction band . The two occupied levels are located at $\sim$1.0 eV and $\sim$1.3 eV above the valence band while the unoccupied level is $\sim$0.2 eV below the conduction band. When including a fraction of Hartree-Fock exchange in the calculation, the valence band is shown to go down with respect to the local electrostatic potential while the conduction band goes up (cf. Sec. 3.1.1). The occupied and unoccupied levels are therefore affected in a similar manner as the valence and conduction band, respectively, when the amount of Hartree-Fock is changed.

The projections of the states in the SiC band gap on the atomic orbitals allow one to identify the carbon atoms of the C-C pair as the origin of the defect states. The isosurfaces of the density (e.g. the square of the wave function) of the three defect states are plotted in Fig. 4.2 (b)-(d). The C-C pair is composed of two sp^2 hybridized carbon atoms. However, the planes of their sp^2 orbitals are nearly perpendicular, which results in a single σ bond whose energy level is located below the valence band. Two singly occupied p orbitals therefore remain (one on each carbon atom) and account for the occupied levels in the band gap. Their corresponding non-bonding orbitals are located at higher energies, one of which results in the unoccupied level located just below the conduction band. The projections of the unoccupied states on the atomic orbitals situate the second non-interacting orbital corresponding to the higher occupied level in the band gap $\sim$0.15 eV above the conduction band. This state is only partially localized on one carbon atom of the C-C pair due to its interactions with the conduction states of SiC. The modelling of the carbon interstitial in bulk $4H$-SiC indicates that trap states related to carbon defects in the substrate can be present in the upper part of the band gap, in contrast with previous studies [35, 56]. However, these states are associated with defects far from the interface and the legitimate question arises whether structural relaxation and dielectric effects present at interfaces would affect their positions.

4.2.2   Carbon pairs in SiC at the SiC/SiO$_2$ interface

Following the line of defects study initiated with the carbon interstitial in bulk SiC, we model the carbon pair defect in five different configurations on the substrate side of the SiC/SiO$_2$ interface. We use the model of the SiC/SiO$_2$ interface introduced in Chap. 3. In the first two configurations, a carbon interstitial shares a carbon lattice site with an atom of the SiC substrate. In the first configuration,

the carbon lattice site is chosen to locate in the last C plane of the SiC substrate, thereby placing the C-C pair in the immediate vicinity of the interface. In the second configuration, the C-C pair is situated farther down in the substrate, about 3 Å from the interface. In the third configuration, the carbon pair replaces a Si atom in the last-by-one Si plane of the SiC substrate. Each carbon of the pair therefore bonds to two other carbon atoms as opposed to silicon atoms in the first two configurations. Finally, the last two configurations present the intermediate situation in which each carbon of the interstitial C-C pair bonds to one silicon atom and one carbon atom of the substrate. The difference between the last two configurations comes from the relative positions of the silicon atoms bonding to the carbon atoms of the C-C pair. When looking along the C-C bond, the two silicon can either be oriented in the same direction as in Fig 4.3 (d) or be oriented in opposing directions as in Fig 4.3 (e). Ball and stick representations of the five configurations are displayed in Fig. 4.3 (a)-(e). The main structural parameters of the relaxed defect models are summarized in Table 4.1.

Table 4.1: Distance and angle parameters of the X_2-C-C-X_2 structures (X refers to Si or C) in the SiC substrate. In the case of the last two structures, C-C and then Si-C distances are given in the corresponding column. Distances are given in Å and angles in degrees. The last two columns refer to the angle between the planes of the two sp^2 hybridized carbon atoms and the average dihedral angles of the X_2-C-C-X_2 structure, respectively. Standard deviations are given in parentheses.

	C-C	X-C	$\angle$ X-C-X	$\angle(sp^2$ planes)	$\sigma_{\angle \text{dih.}}$
Si_2-C-C-Si_2	1.39	1.80	134.9 ± 4.2	89.7	74.9 (2.3)
$(Si_2$-C-C-$Si_2)$'	1.38	1.79	138.2 ± 0.9	89.5	89.0 (0.7)
C_2-C-C-C_2	1.43	1.54	137.5 ± 1.5	89.4	82.4 (0.8)
SiC-C-C-SiC	1.37	1.46/1.78	121.3 ± 1.0	15.3	49.6 (3.5)
(SiC-C-C-SiC)'	1.38	1.45/1.75	127.1 ± 10.0	38.1	52.5 (7.2)

In the previous subsection, it was shown that the defect levels associated with the carbon pair originate from the non-bonding p orbitals of the carbon atoms when the planes of their sp^2 hybridized orbitals are nearly perpendicular. The first three configurations modeled here share this feature. The first two carbon pair defect configurations only differ by their distance from the interface. Their distance and angle parameters are rather similar and the overall defect configuration remains mainly unchanged whether it is located in the vicinity of the in-
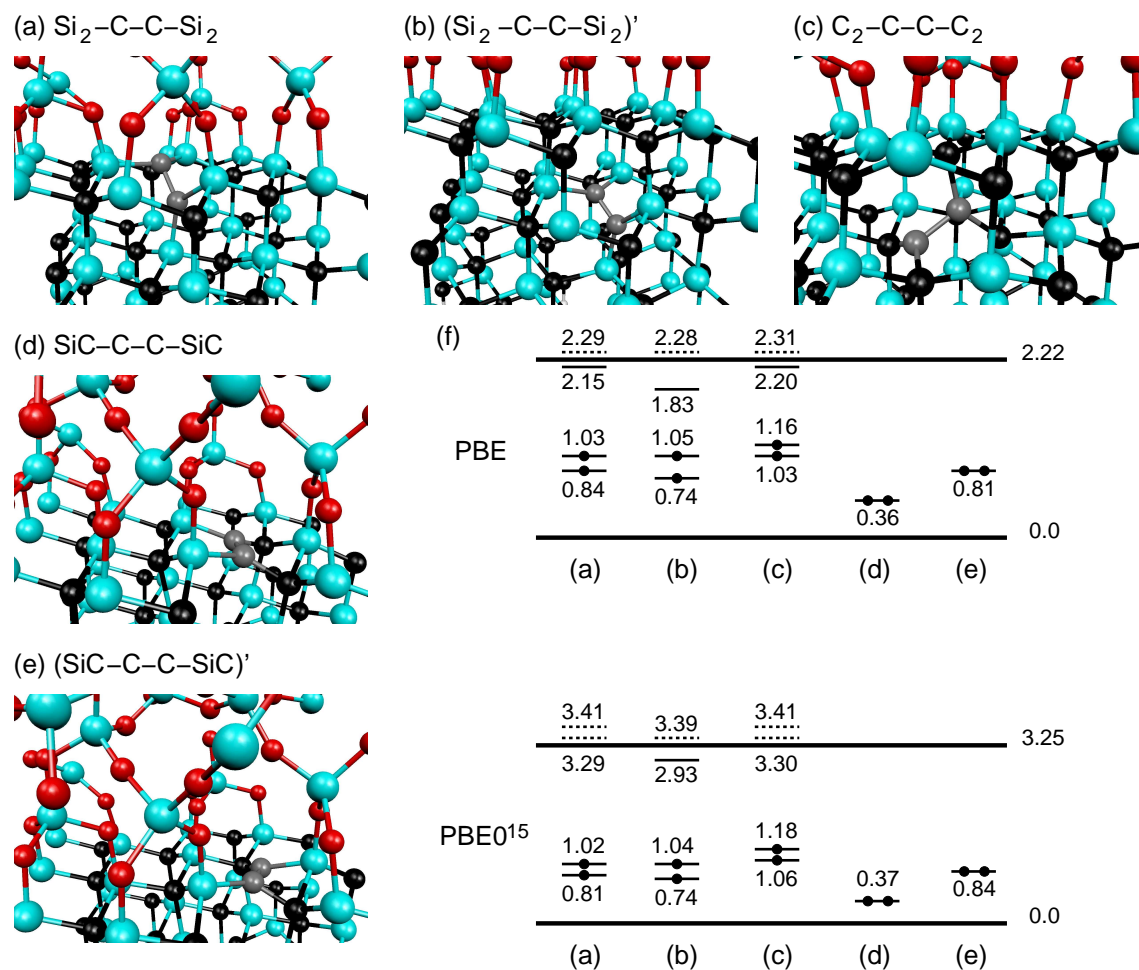
(a) Si$_2$–C–C–Si$_2$

(b) (Si$_2$–C–C–Si$_2$)'

(c) C$_2$–C–C–C$_2$

(d) SiC–C–C–SiC

(f)

(e) (SiC–C–C–SiC)'

Figure 4.3: (a)-(e) The carbon pair defect in SiC at the SiC/SiO$_2$ interface in five different configurations. (f) Defect levels related to the carbon pair defect in configurations (a)-(e). The occupied levels are denoted by one of two black dots for single or double occupancy, respectively, and unoccupied levels located above the SiC conduction band are represented by a dotted line. Energies are given in eV.

terface or farther down in the substrate. However, the (Si$_2$-C-C-Si$_2$)' configuration located deeper in the substrate features structural parameters closer to the carbon pair defect in bulk SiC (cf. Sec. 4.2.1). The Si$_2$-C-C-Si$_2$ configuration benefits from its location at the interface and some structural rearrangements occur. The Si-C-Si and the dihedral Si-C-C-Si angles show some departure from the defect structure in bulk SiC, and the structure near the interface is less symmetric than in the bulk configuration. Despite the different chemical nature of the neighbors of the paired carbon atoms in the C$_2$-C-C-C$_2$ defect model, the overall structure remains very similar to the first two defect configurations. In the C$_2$-C-C-C$_2$ defect model, the distances between carbon atoms of the C-C pair and their neighbors

are strongly reduced, leaving more space for the C-C pair than in the previous configurations. However, despite the different chemical nature of the neighbors of the paired carbon atoms in this defect model, the overall structure remains very similar to the first two defect configurations. In the last two configurations, a carbon pair interstitial is introduced in the close vicinity of the interface. The presence of two additional carbon in the last planes of the substrate results in the reduction of the bond lengths between the carbon atoms of the C-C pair and their neighbors compared to the first three structures. But the main difference resides in the angle between the planes of the two sp^2 hybridized carbon atoms. Whereas the planes of the two sp^2 hybridized carbon atoms are nearly perpendicular in the first three structures, they are almost parallel in the last two configurations.

We then turn to the electronic configuration of the defect structures at the interface. Due to the quantum confinement effects related to the finite thickness of the substrate, the SiC band edges determined from the local density of states are biased. Hence, the defect levels are aligned to the bulk band extrema through the local electrostatic potential. Figure 4.3 (f) shows the defect levels associated with the carbon pair calculated at the PBE and PBE0[15] level of theory[1]. The quantum confinement of the substrate in the interface structure induces a band gap opening of SiC (cf. Sec. 3.4.3). In the interface sructure, some well localized defect levels close to the band extrema but in the band gap of SiC in the interface structure can therefore appear above the conduction band after alignment to the bulk band extrema.

The overall electronic structure descriptions of the defects within the two functional frameworks agree very well. In particular, occupied levels coincide very accurately with respect to the valence band and their locations do not differ by more than 0.03 eV. The locations of the unoccupied levels fluctuate a little bit more but the difference with respect to the conduction band never exceeds 0.11 eV between the two levels of theory. Some occupied levels located just below the conduction band in the PBE description appear a few tenths of eV above the conduction band in the PBE0 description. The absolute difference remains however very small and can be ascribed to the localization of the band edges with respect to the local electrostatic potential calculated with a precision that can differ by a few tenths of eV between the PBE and PBE0[15] calculations.

---

[1]To assess the convergence of the defect levels with the finite thickness of the SiC slab, calculations at the PBE level were carried out with the thickness of SiC doubled. The positions of the defect levels did not shift by more than 0.1 eV
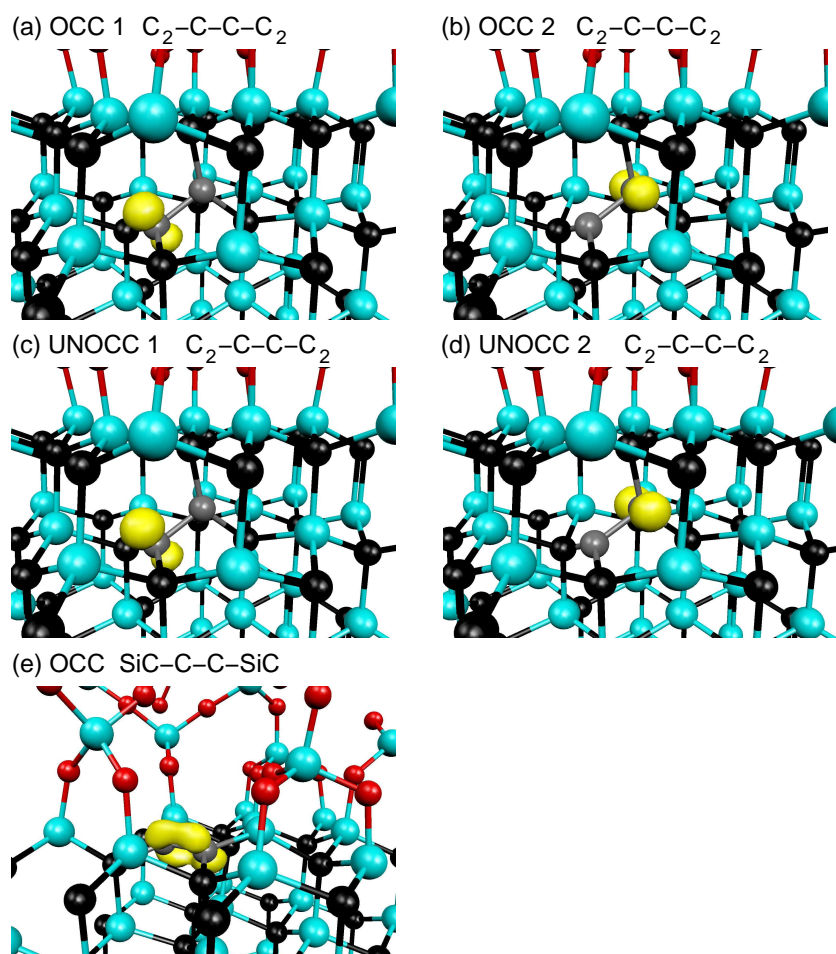
(a) OCC 1 C$_2$–C–C–C$_2$

(b) OCC 2 C$_2$–C–C–C$_2$

(c) UNOCC 1 C$_2$–C–C–C$_2$

(d) UNOCC 2 C$_2$–C–C–C$_2$

(e) OCC SiC–C–C–SiC

Figure 4.4: Isosurfaces of the density of the defect states related to the carbon pair in (a)-(d) the C$_2$-C-C-C$_2$ model structure. The defect levels are ordered in ascending energy (OCC1 denotes the lowest occupied level in the band gap and UNOCC2 the highest non-occupied level related to the carbon pair defect). (e) Isosurface of the density of the occupied defect state related to the carbon pair in the SiC-C-C-SiC structure.

The overall electronic structures of the first three different defect configurations appear very similar. In all these configurations, two occupied levels locate between about 0.7 eV and 1.2 eV above the valence band and their separation ranges from 0.1 eV to 0.3 eV. Two unoccupied levels lie between 0.4 eV below the conduction band and 0.2 eV above the conduction band, and are 0.1 eV to 0.5 eV apart. These differences in locations and separations can be attributed to the local environment of the defect C-C pair. In particular, when a carbon atom shares a carbon lattice site, the location of the first unoccupied level in the SiC band gap can fluctuate by 0.4 eV whether the defect structure is located in the vicinity of the interface (cf. structure Si$_2$-C-C-Si$_2$) or farther down in the substrate (cf.

structure (Si$_2$-C-C-Si$_2$)'), involving different structural relaxations. In a perfectly symmetric arrangement around the C-C pair and provided their interaction can be neglected, the two occupied and the two unoccupied carbon levels would be degenerate and located at the same energy. Depending on the structural relaxations allowed by the local constraints of the environment, departures from this ideal situation occur and the two occupied and the two unoccupied levels split. Despite these small location differences, the occupied and unoccupied levels in all three defect configurations share the same origin. Figure 4.4 (a)-(d) shows the isosurfaces of the density of defect states related to the carbon pair in the C$_2$-C-C-C$_2$ model structure. The two occupied levels are the singly occupied p orbitals of the C-C pair, and their corresponding non-bonding orbitals account for the two unoccupied levels. In this case, each level is clearly associated with one of the two carbon atoms of the C-C pair. Because of degeneracy, one defect level can also result from the partial contribution of both carbon atoms. In all cases, the two occupied and the two unoccupied levels originate from the overall C-C pair
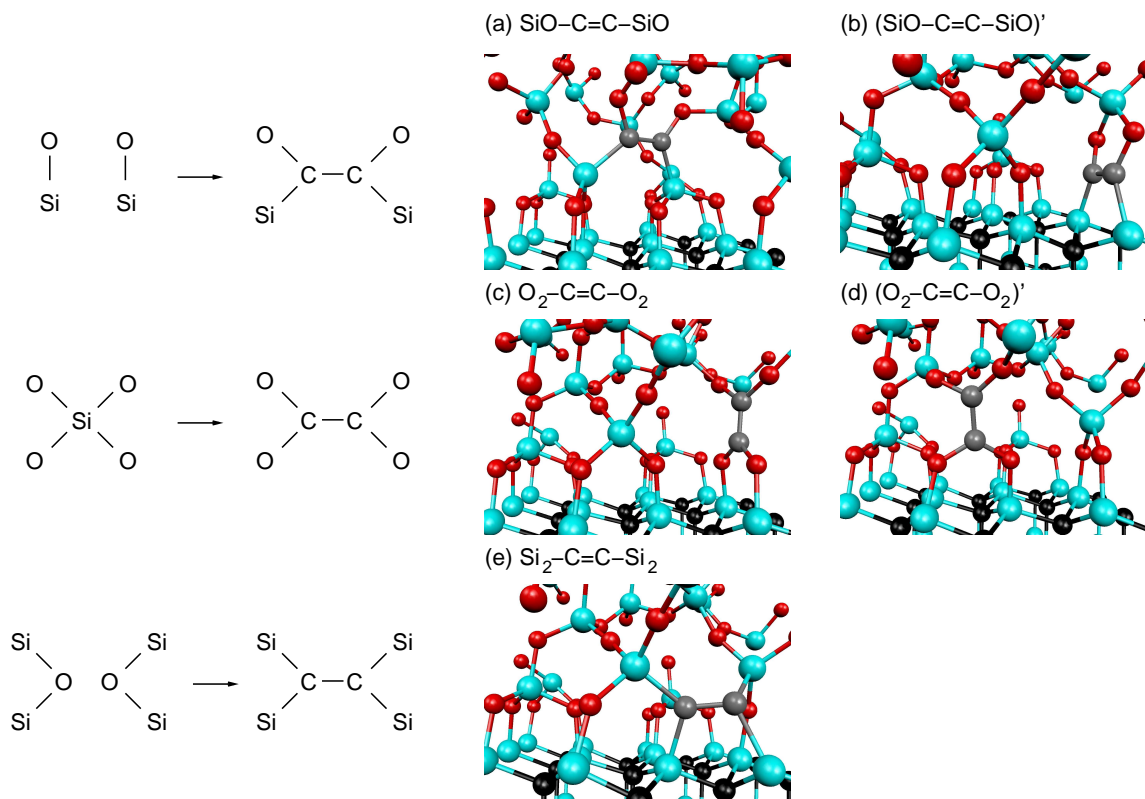

Figure 4.5: The carbon pair defect in SiO$_2$ at the SiC/SiO$_2$ interface in five different configurations. The insertion of the C-C pair in the different environments is represented schematically and the corresponding ball-and-stick representations of the relaxed structures are shown.

orbitals.

In the last two defect structures modeled in the substrate, a different situation occurs. In contrast with the first three defect structures, the angle between the planes of the two sp^2 hybridized carbon atoms is far from $90°$. In these cases, the p orbitals of the carbon atoms of the C-C pair can overlap and form a π bond. The isosurface of the occupied defect state related to the carbon pair in the SiC-C=C-SiC structure is shown in Fig. 4.7 (e). This results in a defect level doubly occupied in the lower part of the SiC band gap. As noticed for the unoccupied levels in the first three structures, the different local environment (in particular the angle between the planes of the two sp^2 hybridized carbon atoms in this case) accounts for the variation of the defect level position. The corresponding unoccupied level does not occur in the band gap.

4.2.3   Carbon pairs in SiO$_2$ at the SiC/SiO$_2$ interface

During the SiC oxidation, carbon atoms can be incorporated in the SiO$_2$ oxide. We therefore investigate the possible configurations of the C-C pair in the oxide. Two carbon atoms can occur at the interface and disrupt Si-O bonds; each carbon therefore bonds to one silicon atom and one oxygen in addition to its neighbor carbon atom (Fig. 4.5 (a) and (b)). Two such configurations are modeled. In the first one, the Si-O bonds in which the C-C pair incorporates involve silicon atoms of the first Si plane of the oxide and oxygen atoms of the second O plane. The second configuration involves silicon atoms of the terminating Si plane of the substrate. A C-C pair can also replace a silicon atom of the oxide (Fig. 4.5 (c) and

Table 4.2: Distance and angle parameters of the X$_2$-C-C-X$_2$ structures (X refers to Si or C) in the oxide. Distances are given in Å and angles in degrees. The last two columns refer to the angle between the planes of the two sp^2 hybridized carbon atoms and the average dihedral angle of the X$_2$-C-C-X$_2$ structure, respectively. Standard deviations are given in parentheses.

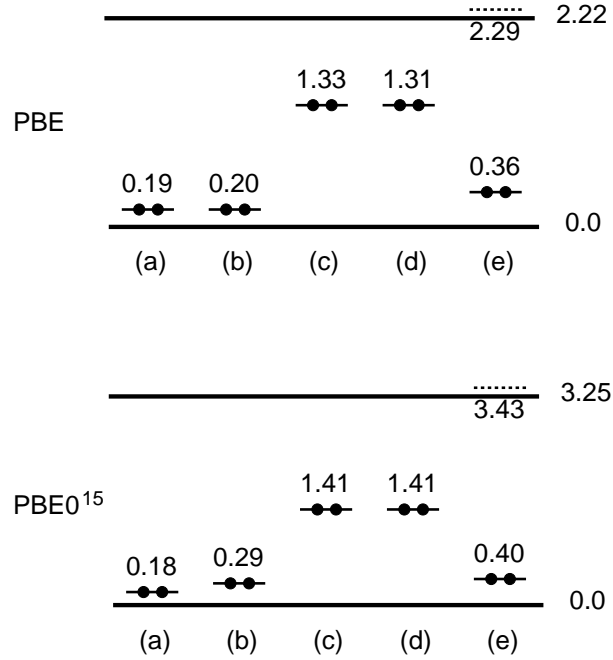|	C-C	O-C	Si-C	$\angle$ X-C-X	$\angle(sp^2$ planes)	$\sigma_{\angle \text{dih.}}$
SiO-C=C-SiO	1.36	1.38	1.87	118.0 ± 6.6	10.1	11.1 (8.1)
(SiO-C=C-SiO)'	1.39	1.39	1.87	128.9 ± 1.1	31.9	10.4 (6.1)
O$_2$-C=C-O$_2$	1.36	1.37	—	117.8 ± 2.1	16.3	16.2 (0.9)
(O$_2$-C=C-O$_2$)'	1.35	1.37	—	119.1 ± 0.9	51.0	72.5 (4.3)
Si$_2$-C=C-Si$_2$	1.38	—	1.91	118.0 ± 3.9	48.5	51.0 (23.5)

Figure 4.6: Defect levels related to the carbon pair defect in configurations (a)-(e) as denoted in Fig. 4.5. The occupied levels are denoted by a black dot, and unoccupied levels located above the SiC conduction band are represented by a dotted line. Energies are given in eV.

(d)). Each carbon atom bonds to two oxygen and one carbon atom. Two such configurations in which the replaced silicon atom belongs to the first Si plane of the oxide are studied. Finally, a C-C pair defect replacing two neighboring oxygen atoms of the first O plane of the oxide is modeled (Fig. 4.5 (e)). In these modeled defects, the carbon atoms therefore bond to each other and to (1) one silicon atom and one oxygen atom, (2) two oxygen atoms, and (3) two silicon atoms. Fig. 4.5 shows schematically the insertion of the C-C pair in the different environments and the corresponding ball-and-stick representations of the relaxed structures.

Table 4.2 summarizes the distance and angle parameters of the defect structures. The distance between the carbon atoms of the C-C pair and the distance between carbon atoms of the C-C pair and oxygen/silicon neighbors are very similar in the five defect structures. In contrast, the angle parameters cover a wide range of values across the five structures. In particular, the angle between the planes of the two sp^2 hybridized carbon atoms varies from $10°$ to $51°$, as opposed to the C-C pair defect structures in SiC. The standard deviation of the dihedral angles involving the C-C pair also describes the large departure from the previous modelling of the C-C pair in SiC where the defect structure could be schematically represented as two orthogonal planes with all dihedral angles close to $90°$. The
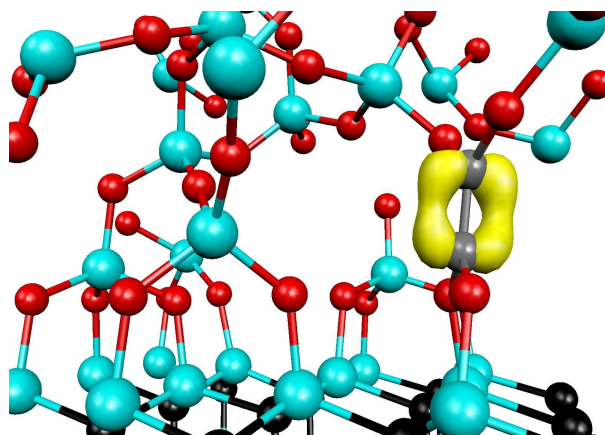
Figure 4.7: Isosurface of the density of the occupied defect state related to the carbon pair in the O$_2$-C=C-O$_2$ structure.

amorphous SiO$_2$ network is indeed more deformable than the SiC crystal and can accomodate more easily important structural relaxations.

Figure 4.6 shows the defect levels of the five C-C pair defect configurations calculated at the PBE and PBE0[15] levels of theory. Both occupied and unoccupied levels descriptions correspond very well and their locations with respect to the valence band and conduction band agree within 0.1 eV. In all five defect structures a doubly occupied level locates in the low/mid part of the band gap. In contrast with the first three defect structures modeled in the SiC substrate, the angle between the two planes formed by each carbon atom of the C-C pair and its neighbors is far from 90° and varies between 10° and 51°. In these cases, the p orbitals of the carbon atoms of the C-C pair can overlap and form a π bond as in the last two defect configurations modeled in SiC at the interface. The isosurface of the occupied defect state related to the carbon pair in the O$_2$-C=C-O$_2$ structure, very similar to that of the SiC-C-C-SiC structure modeled in SiC, is shown in Fig. 4.7.

Structures SiO-C=C-SiO and (SiO-C=C-SiO)', and structures O$_2$-C=C-O$_2$ and (O$_2$-C=C-O$_2$)', present two different configurations of the C-C pair defect with the same neighboring environment, respectively. Despite their different structural parameters, in particular the angle between the planes of the sp^2 hydridized carbon atoms, the occupied defect levels remain unchanged. Comparing the models of the C-C pair defect in SiC and SiO$_2$, the angle between the planes of the sp^2 hydridized carbon atoms appears fundamental to obtain two singly occupied unpaired orbitals or one doubly occupied paired orbital. However, within the range of angle values where the π bonding occurs, the energy level does not appear to

depend in a perceptible way on the angle. Another difference with the models of the C-C pair defect in SiC can be seen in the detection of unoccupied levels. The antibonding π orbital could be detected only in the configuration where the C-C pair bonds to four Si atoms, as proposed earlier by Knaup *et al.* [34]. In that case, it locates just above the conduction band of SiC whereas in all other configurations its interaction with the SiC conduction levels made it undetectable. However, its detection in one defect structure indicates that near interface trap states related to carbon atoms can occur in the oxide. Moreover, only a few possible configurations of the C-C pair in the SiO_2 are here modeled. Trap levels could therefore appear below the SiC conduction band in some configurations of the C-C pair defect in the near interface oxide.

4.2.4 Investigation of the C-C pair in molecules

C-C pair defects were modeled in the SiC substrate and in the SiO_2. In both cases, trap states located around the conduction band of SiC could be identified. To investigate the energy range that these trap states can span, we now turn to an investigation of the C-C pair in molecules. The variety of possible chemical bonding environment of the C-C pair and complex structural arrangements contribute to the fluctuations of the defect levels positions. However, a major parameter appears to be the relative orientation of the paired or unpaired p orbitals of the two sp^2 hybridized carbons. We therefore here investigate the positions of the defect levels of the C-C pair versus the angle between the planes of the two sp^2 hybridized carbons. We model three molecules in which the C-C pair shows similar neighbors as in the defect strutures modeled at the interface.

Figure 4.8 shows the isosurfaces of the density of the C-C states when the angle between the planes of the two sp^2 hybridized carbons is 0°, 45°, and 90°. The two angles 0° and 90° lead to isosurfaces very similar to the ones of the C-C
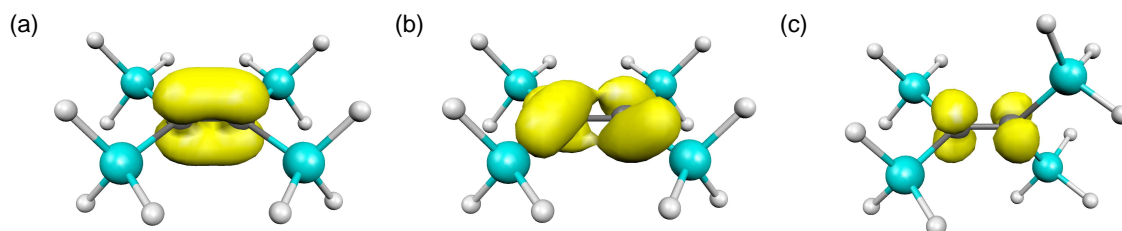

Figure 4.8: Isosurface of the density of the p orbitals in the $C_2(SiH_3)_4$ molecule when the angle between the planes of the two sp^2 hybridized carbons is (a) 0°, (b) 45°, and (c) 90°.
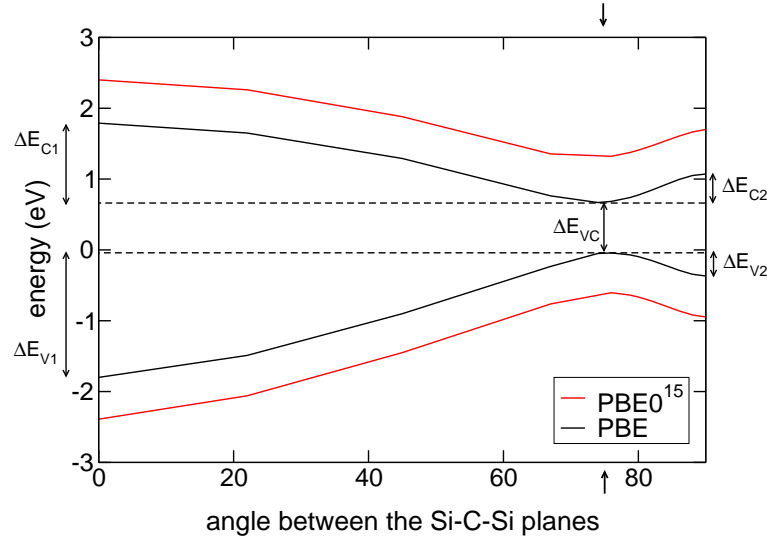
Figure 4.9: Evolution of the highest occupied and lowest unoccupied levels with respect to the σ C-C bond in the C$_2$(SiH$_3$)$_4$ molecule when the angle between the planes of the two sp^2 hybridized carbon atoms varies between 0° and 90°.

defect structures in SiO$_2$ where the p orbitals are nearly parallel and pair up, and in SiC where the p orbitals are almost perpendicular and do not overlap, respectively. The geometry of the molecules are first fully relaxed with the constraint that all but the hydrogen atoms remain in the same plane. The angle between the planes of the two sp^2 hybridized carbon atoms is then varied between 0° and 90°. The defect levels are aligned to the σ bond of the C-C pair.

The positions of the highest occupied and lowest unoccupied defect levels of the C-C pair versus the angle between the planes of the two sp^2 hybridized carbons are shown in Fig. 4.9 for the C$_2$(SiH$_3$)$_4$ molecule. The figures for the C$_2$(CH$_3$)$_4$ and C$_2$(OH)$_4$ molecules are very similar and are not presented here; the energies defined in Fig. 4.9 are reported in Table 4.3 for the three molecules.

The PBE and PBE0[15] descriptions provide overall the same picture with the usual larger separations between occupied and unoccupied levels in PBE0[15]. In all three molecules, the smallest separation between the highest occupied and lowest unoccupied levels occurs when the system most stable configuration switches from spin-unpolarized to spin-polarized configuration between 74° and 76° for the three molecules. The largest separation between occupied and unoccupied levels is obtained when the planes of the two sp^2 hybridized carbon atoms are parallel. When they are orthogonal, the highest occupied level and the lowest unoccupied level are shifted down and up, respectively, by about 0.3-0.6

eV compared to their maximum and minimum value (cf. Table 4.3).

The picture provided by these molecular models is partial as the only parameter is the angle between the planes of the two sp^2 hybridized carbon atoms. However, it highlights some interesting features of the C-C pair defect. First, the trap states of the C-C pair have lower energies and can therefore be identified near the SiC conduction band edges when the angle between the planes of the two sp^2 hybridized carbon atoms is close to $\sim 75°$. This situation occurs much more frequently in the SiC substrate where the tetrahedra formed by the atoms bonded to the C-C pair cannot be strongly distorted. On the other hand, the structure around a C-C pair in the amorphous SiO_2 oxide can relax much more easily and accomodate a π bond stabilizing the system. This accounts for the rare detection of unoccupied C-C levels when the defect is modeled in SiO_2 in contrast with the modelling in SiC. Second, the chemical nature of the atoms bonded to the C-C pair has an impact on the splitting between occupied and unoccupied levels. The $C_2(SiH_3)_4$ molecules features the smallest separation between occupied and unoccupied levels throughout the whole angle range. The only unoccupied level detected in the five defect models in the oxide is indeed associated with the Si_2-C-C-Si_2 structure. In the SiC susbtrate, the lowest unoccupied C-C level detected also derives from the Si_2-C-C-Si_2 defect structure.

The qualitative comparison between the separations of the occupied and unoccupied levels in Si_2-C-C-Si_2 structures at the interface and in the $C_2(SiH_3)_4$ molecule is also instructive. The Si_2-C-C-Si_2 structure in SiO_2 features a level separation of 1.9 eV and 3.0 eV at the PBE and PBE0[15] levels of theory, respectively. When the angle between the planes of the two sp^2 hybridized carbon atoms

Table 4.3: Values of the energies defined in Fig. 4.9 for $C_2(SiH_3)_4$, $C_2(CH_3)_4$, and $C_2(OH)_4$ at the PBE and PBE0[15] levels of theory.

	ΔE_{VC}	ΔE_{C1}	ΔE_{C2}	ΔE_{V1}	ΔE_{V2}
$C_2(SiH_3)_4$ PBE	0.7	1.1	0.4	1.8	0.3
$C_2(SiH_3)_4$ PBE0[15]	1.9	1.1	0.4	1.8	0.3
$C_2(CH_3)_4$ PBE	1.2	1.5	0.6	1.8	0.4
$C_2(CH_3)_4$ PBE0[15]	2.4	1.1	0.5	1.8	0.4
$C_2(OH)_4$ PBE	0.9	1.2	0.4	0.9	0.4
$C_2(OH)_4$ PBE0[15]	2.2	1.1	0.4	0.9	0.4

of the C$_2$(SiH$_3$)$_4$ molecule has the same value of $\sim$49°, the level separation is 2.0 eV (PBE) and 3.1 eV (PBE0[15]), in very good agreement with the values for the defect structure in SiO$_2$. When a similar comparison for the two Si$_2$-C-C-Si$_2$ structures in SiC is performed, a poorer agreement is obtained with average level separations of 1.0 eV (PBE) and 2.1 eV (PBE0[15]) in the interface structures to be compared with level separations of 1.4 eV (PBE) and 2.6 eV (PBE0[15]) in the molecule. However, this agreement is sufficiently good to use the molecular model together with the modeled defect structures at the interface for an estimation of the energy range of the C-C trap levels. Combining these two approaches allows us to explore all the possible angles between the planes of the two sp^2 hybridized carbon atoms that the defect structure can take and to incorporate structural relaxations at the interface in the description. Taking $E_{90°}^{mol}$ as the energy of the lowest unoccupied level in the C$_2$(SiH$_3$)$_4$ molecule when the angle between the planes of the two sp^2 hybridized carbon atoms is 90°, we note from Fig. 4.9 that the minima of the lowest unoccupied level in the C$_2$(SiH$_3$)$_4$ molecule locates at $E_{90°}^{mol}$-0.4 eV when the angle between the planes of the two sp^2 hybridized carbon atoms is 78°. As the modeled Si$_2$-C=C-Si$_2$ structures in SiC at the interface also feature an angle $\sim$90°, we can align the average energy of the lowest unoccupied level in the modeled Si$_2$-C=C-Si$_2$ structure in SiC to $E_{90°}^{mol}$ of the C$_2$(SiH$_3$)$_4$ molecule. Finally, this gives a minimum value for the lowest unoccupied level at the interface located at about 0.5 eV below the SiC conduction band (PBE0[15]). We therefore suggest that this large distribution of energies could correspond to the broad hump in the density of states centered just below the SiC conduction band.

4.2.5 Single carbon atoms in the oxide

Two defect structures involving single carbon atoms in the oxide are now studied. In the SiC/SiO$_2$ system, carbon and silicon share a preference for fourfold coordination. A carbon atom could then replace a silicon atom during the oxidation growth and bond to four oxygen of the oxide. A carbon atom could also replace an oxygen atom in a Si-O-Si bond to form a Si$_2$-C=O structure. Ball-and-stick representations of these two configurations are shown in Fig. 4.10 (a) and (b).

When one carbon atom replaces one silicon atom in the oxide network, the structural rearrangement is driven by the shorter C-O distance. In the relaxed structure, the averaged C-O bond length is 1.41 Å about 16% shorter than the
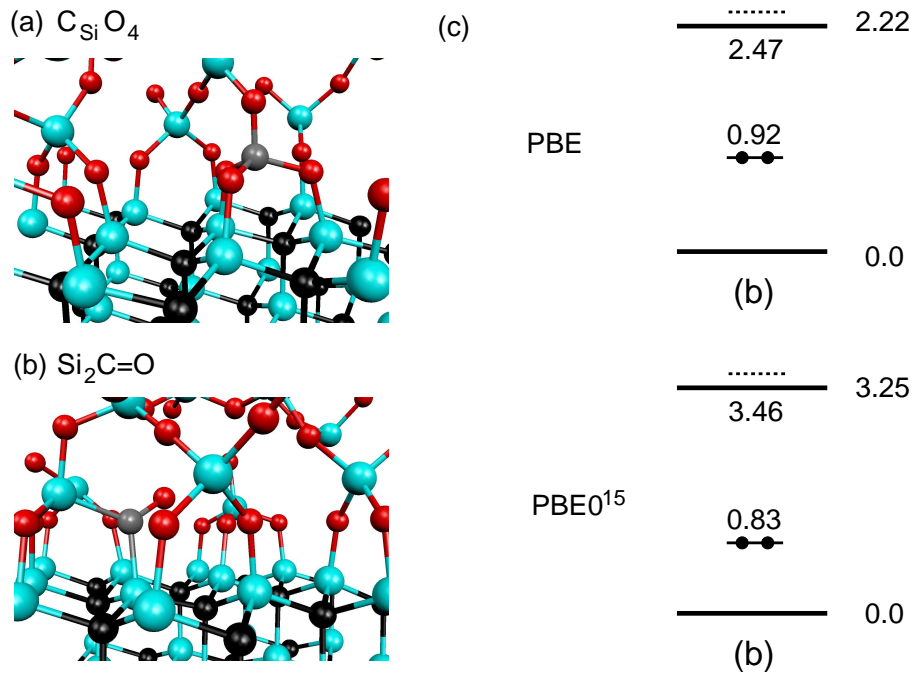
Figure 4.10: Ball-and-stick representations of the (a) $C_{Si}O_4$ and (b) Si_2-C=O structures. (c) Defect levels associated with the carbon atom of the structure shown in (b).

averaged Si-O bond length in the oxide. All the other structural parameters remain almost unchanged upon replacement of silicon by carbon. In the Si_2-C=O structure, the carbon atom is threefold coordinated. The angle between the two planes defined by the Si-C-O atoms is only $11.2°$, making the overall structure almost planar. The Si-C bond lengths of 1.87 Å are comparable to that in the SiC substrate, and the C-O bond length is 1.23 Å. The Si-C-O angles are about $122°$, so that the carbon atom almost locates at the barycenter of the triangle formed by the oxygen atom and the two silicon atoms.

The electronic structure of the configuration in which a carbon atom replaces
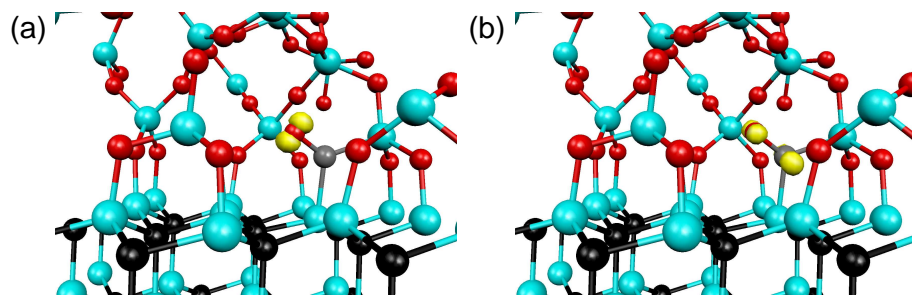

Figure 4.11: (a) Isosurface of the density of the (a) occupied and (b) unoccupied defect states in the Si_2-C=O structure, as identified in Fig. 4.10 .

a Si atom does not reveal any defect level in the gap. The chemical similarity of carbon and silicon accounts for this. In the Si$_2$-C=O structure, one doubly occupied defect lies in the lower part of the SiC band gap, while one unoccupied level locates slightly above the SiC conduction band. These defect levels can be attributed to one of the oxygen lone pairs and to the π^* anti-bonding orbital, respectively (Fig. 4.11). The second oxygen lone pair is lower in energy and does not give any level in the gap. The overall picture for the unoccupied defect level is very similar to that of the C-C pair when the planes of the two sp^2 hybridized carbons are nearly parallel. This confirms the presence of carbon-related defects near the SiC conduction band.

4.2.6   Charge transition levels of the C-C pair defect

Charge transition levels in the bulk models

In the previous subsections, unoccupied Kohn-Sham energy levels related to the C-C pair defect near the conduction band of SiC were identified in bulk SiC and at the SiC/SiO$_2$ interface. They provide a first step towards the identification of possible defects. However, the physical significance of Kohn-Sham energy levels is questionable. It is preferable to describe defect levels through the determination of charge transition levels, which are defined as total-energy differences. We here focus on the formation energy of the C-C pair defect in its negative charge states. Charged interface calculations in periodic slab systems are difficult to treat as the spurious contribution to the total energy from the interaction of periodic charges at the interface of different dielectric materials is hard to estimate. To circumvent this problem, we calculate the formation energy of the charge states through bulk calculations. The C-C pair defect is modeled in bulk SiC (cf. Sec. 4.2.1) and in amorphous bulk SiO$_2$ in two different configurations. The structural relaxation and the image charge interaction occurring at the interface are then estimated and the formation energies of the C-C pair defect at the interface determined.

The formation energy of a defect state with charge q is determined as a function of the electron chemical potential μ with respect to the edge of the valence band ϵ_v of the defect-free system as:

$$E_f^q(\mu) = E^q - E^0 + q(\epsilon_v + \mu + \Delta V) + E_{\mathrm{corr}} \qquad (4.1)$$

where E^q and E^0 are the total energies for the defect with charge q and the neutral defect, respectively. ΔV is required for the accurate positioning of the va-
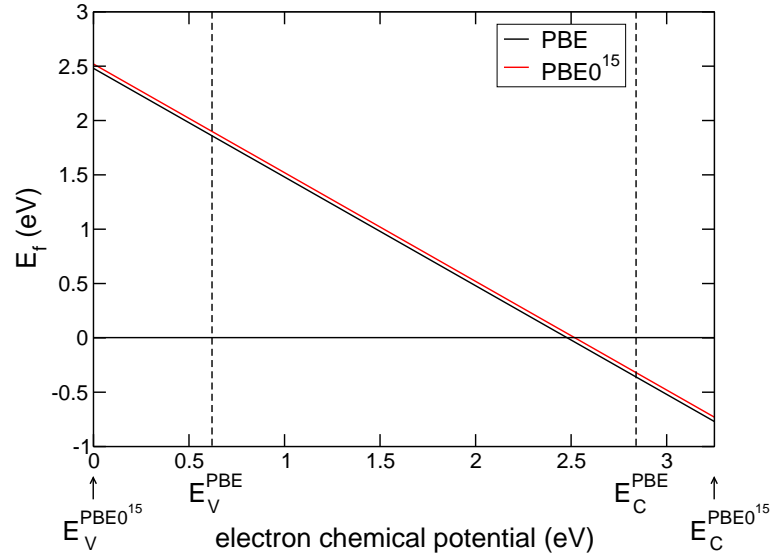
Figure 4.12: Formation energies of the -1 charge state of the C-C pair defect vs electron chemical potential in bulk $4H$-SiC at the PBE (black) and PBE0^{15} (red) levels of theory. The valence band of bulk $4H$-SiC in the PBE0^{15} calculation is used as the reference for the electron chemical potential. The positions of the valence and conduction bands at the PBE level aligned to PBE0^{15} values through the electrostatic potential are also indicated.

lence band by aligning the electrostatic potential far from the defect to that of the defect-free bulk model [176]. E_{corr} is a correction that accounts for the spurious interaction of the charged defect with the compensating uniform background when periodic boundary conditions are used [177]. We use a dielectric constant of 9.6 for bulk SiC [10] to estimate $E_{\mathrm{corr}}^{\mathrm{SiC}} = 0.21$ eV for $|q| = 1$ and a dielectric constant of 4.0 for bulk SiO$_2$ leading $E_{\mathrm{corr}}^{\mathrm{SiO_2}} = 0.49$ eV and $E_{\mathrm{corr}}^{\mathrm{SiO_2}} = 1.96$ eV for $|q| = 1$ and $|q| = 2$, respectively. The formation energies of the negative (-1) charge state of the C-C pair defect vs electron chemical potential in bulk $4H$-SiC are shown at the PBE and PBE0^{15} levels of theory in Fig. 4.12.

The position of the charge transition level $\mathrm{E}^{0/-1}$ is defined as the value of the chemical potential at which the neutral and negative charge states of the C-C pair defect have equal formation energies. $\mathrm{E}^{0/-1}$ differs considerably when referred to the conduction band in PBE and PBE0^{15} calculations. It locates at $E_c - 0.36$ eV and $E_c - 0.73$ eV at the PBE and PBE0^{15} levels of theory, respectively. However, when referred to the electrostatic potential, $\mathrm{E}^{0/-1}$ determined with the two functionals agree very well. An explanation was provided very recently [178]. It was shown that the two contributions entering the expression for the difference in charge transition levels between PBE and PBE0 are defect-defect interactions

Table 4.4: Charge transition levels of the C-C pair in SiC and SiO$_2$ calculated at the PBE and PBE0 levels. The reference is the SiC conduction band. For the C-C pair defects modeled in SiO$_2$, the method presented in Sec. 3.4.3 is used to describe the band offset. The ratio of the position of the charge transition level above the SiO$_2$ valence band to the bulk SiO$_2$ band gap is given in parentheses.

	$(C\text{-}C)^{SiC}$	$(C\text{-}C)_1^{SiO_2}$	$(C\text{-}C)_2^{SiO_2}$
PBE $0/-1$	-0.36 (63%)	-0.31 (64%)	-0.20 (66%)
PBE $-1/-2$	—	0.46 (78%)	0.61 (81%)
PBE0 $0/-1$	-0.73 (62%)	-0.45 (65%)	-0.29 (67%)
PBE0 $-1/-2$	—	0.32 (74%)	0.48 (76%)

and defect-bulk interactions.[2] For a localized defect, the differences between PBE and PBE0[15] charge transitions levels due to defect-defect interactions should be analogous to the corresponding differences for ionization potentials and electron affinities in the case of atoms and molecules. For such isolated systems, these quantities can be expressed as total-energy differences and are already well described in semilocal approximations such as PBE [179, 180], as demonstrated by extensive quantum chemistry calculations [181]. Hence, this contribution is expected to give shifts independent of the location of the defect level in the band gap. As for the defect-bulk contributions, it can be shown that they vanish in the limit of point-like defect states.

A similar agreement between PBE and PBE0 is found for the charge transition levels of the two C-C pair defects modeled in bulk SiO$_2$. Table 4.4 shows the location of the charge transition level with respect to the SiC conduction band and the ratio of the position of the charge transition level above the SiO$_2$ valence band to the bulk SiO$_2$ band gap.[3] These relative PBE and PBE0 charge transition levels agree within 5%. However, the charge transition levels expressed with respect to the SiC conduction band obtained with PBE0 are expected to yield better comparison with experiment as the description of the band gap is improved with PBE0 compared to PBE. For the rest of the discussion, we will therefore only use

---

[2]In this section, PBE0[15] and PBE0[35] are used for the calculations in bulk SiC and bulk SiO$_2$, respectively. For the sake of simplicity, we will refer to both functionals as PBE0 when the discussion equally applies to both of them.

[3]As mentionned in Sec. 4.2.1, the second unoccupied defect level is not well localized in bulk SiC, and the $-1/-2$ charge transition level can therefore not be calculated.
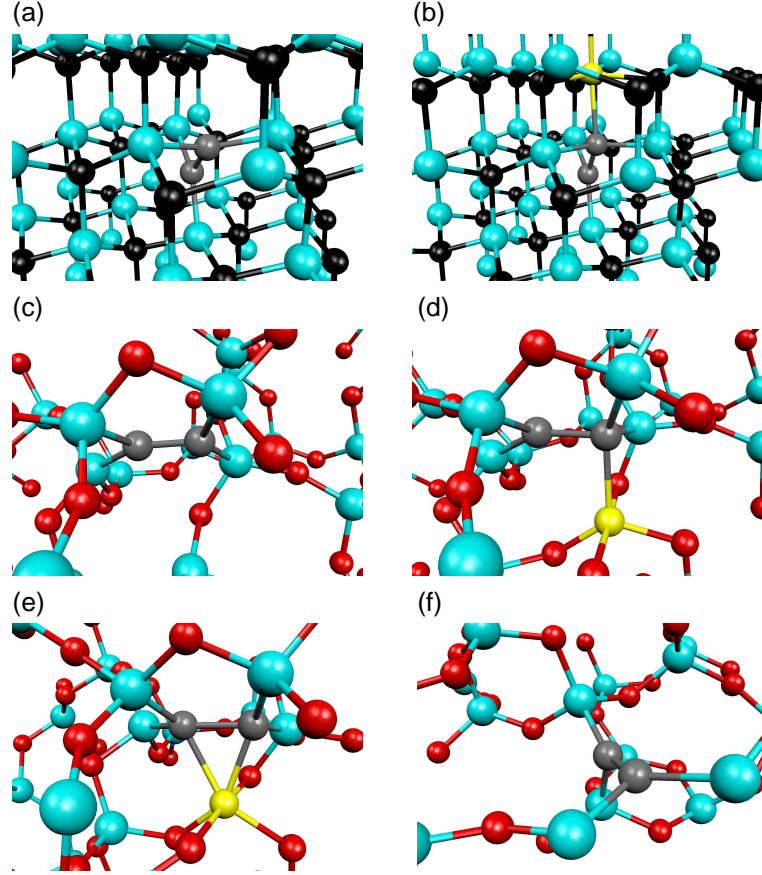
Figure 4.13: The C-C pair defect in bulk SiC and bulk SiO_2. The $(C\text{-}C)^{SiC}$ model is shown in the (a) neutral and (b) -1 charge state, the $(C\text{-}C)_1^{SiO_2}$ model is shown in the (c) neutral, (d) -1 and (e) -2 charge state, and the $(C\text{-}C)_2^{SiO_2}$ model is shown in the (f) neutral charge state. The nearby overcoordinated Si atom is highlighted (yellow).

the PBE0 charge transition levels.

Before comparing the charge transition levels of the C-C pair defect in the different environments, we describe the different structural relaxations that the system can undergo upon charging. Figure 4.13 shows the relaxed structures in the neutral and negative charge states. The main structural parameters are summarized in Table 4.5. Two scenarios arise when negative charges are added to the system. When one electron is introduced, one carbon atom of the C-C pair bonds to a neighboring silicon atom in the $(C\text{-}C)^{SiC}$ and in the $(C\text{-}C)_1^{SiO_2}$ structures. This silicon atom becomes then fivefold coordinated. Upon introduction of a second electron, this silicon atom bonds to the second carbon atom of the C-C pair and becomes sixfold coordinated. It was checked that the configurations shown in Fig. 4.13 are recovered upon charging and discharging, thereby assuring that these are the most stable configurations in the neutral and negative charge states. In

Table 4.5: Distance and angle parameters of the Si$_2$-C-C-Si$_2$ structures in bulk SiC and bulk SiO$_2$ in the neutral and negative charge states. Distances are given in Å and angles in degrees. Si* refers to the silicon atom fivefold (sixfold) coordinated to one (two) of the carbon atoms of the C-C pair. The two Si*-C distances are averaged in the doubly charged (C-C)$_1^{\text{SiO}_2}$ structure.

	C-C	Si-C	Si*-C	$\angle$ Si-C-Si	$\angle(sp^2\text{planes})$
(C-C)$^{\text{SiC}}$, $q=0$	1.37	1.79	—	138.4 ± 1.3	89.3
(C-C)$^{\text{SiC}}$, $q=-1$	1.47	1.79	2.08	135.0 ± 1.8	—
(C-C)$_1^{\text{SiO}_2}$, $q=0$	1.37	1.86	—	124.0 ± 13.6	6.4
(C-C)$_1^{\text{SiO}_2}$, $q=-1$	1.51	1.86	1.95	117.8 ± 7.8	—
(C-C)$_1^{\text{SiO}_2}$, $q=-2$	1.62	1.81	1.96	120.8 ± 14.1	—
(C-C)$_2^{\text{SiO}_2}$, $q=0$	1.46	1.91	—	94.6 ± 5.8	80.4
(C-C)$_2^{\text{SiO}_2}$, $q=-1$	1.50	1.85	—	95.4 ± 5.1	73.6
(C-C)$_2^{\text{SiO}_2}$, $q=-2$	1.57	1.80	—	96.8 ± 4.5	78.1

the second scenario, there is no silicon atom in the vicinity of the C-C pair, and the structure hardly changes upon charging. This is the case for the (C-C)$_2^{\text{SiO}_2}$ structure.

Despite the different configurations in the neutral and charge states of the C-C pair defect modeled in bulk SiC and bulk SiO$_2$, the charge transition levels calculated in the three different models have very similar values. The $0/-1$ charge transition level locates between 0.7 and 0.3 eV below the SiC conduction band, and the $-1/-2$ charge transition level is $\sim$0.5-0.6 eV above the SiC conduction band.

Figure 4.14 shows the comparison between the positions of the Kohn-Sham energy levels and their corresponding charge transition levels in the (C-C)$^{\text{SiC}}$ structure and in the (C-C)$_1^{\text{SiO}_2}$ structure. The different behaviour of the Kohn-Sham energy levels and the charge transition levels upon incorporation of a fraction of exact exchange noticed before is confirmed here. The occupied Kohn-Sham energy levels tend to follow the evolution of the valence band while the unoccupied Kohn-Sham energy levels follow the conduction band. On the other hand, the charge transition levels do not fluctuate when referred to the electrostatic potential. This leads to the charge transition levels being up to 1.2 and 1.8 eV below the corresponding Kohn-Sham level at the PBE0[15] and PBE0[35] level of theory, respectively. Overall, the large fluctuations of the Kohn-Sham energy levels with
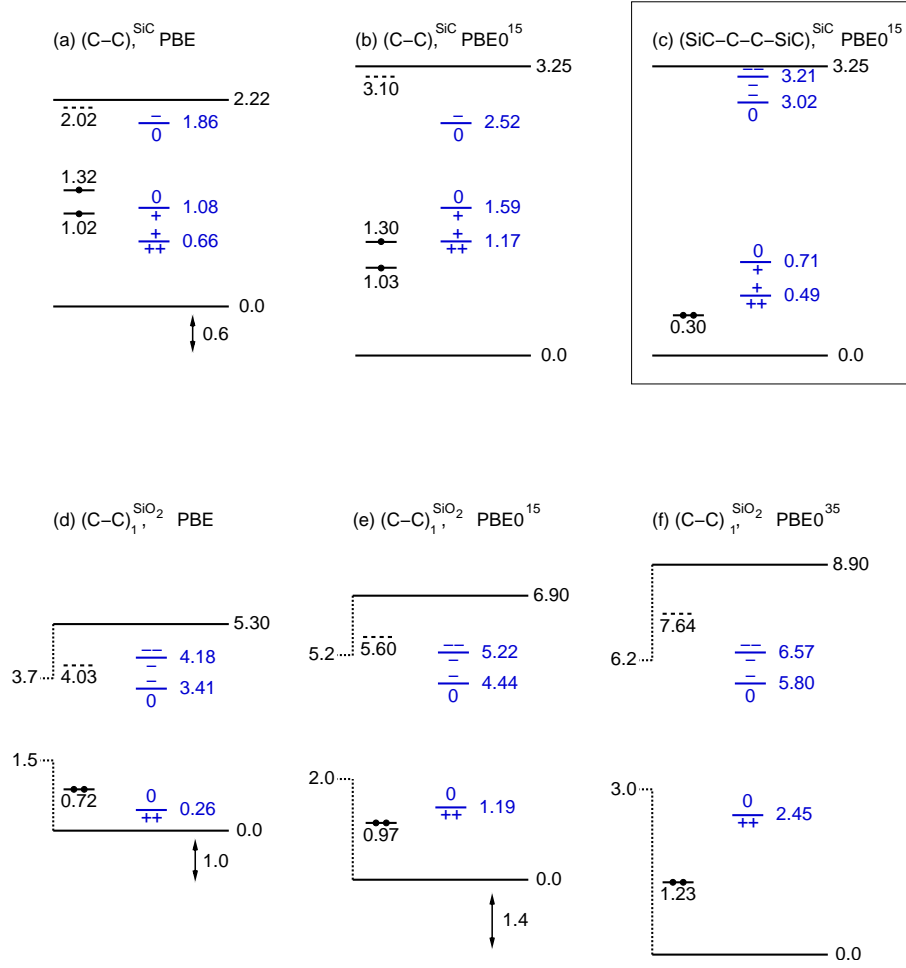
Figure 4.14: Comparison of the positions of the Kohn-Sham energy levels (black) and their corresponding charge transition levels (blue) in (a)-(b) the $(C-C)^{SiC}$ structure, (c) the $(SiC-C-C-SiC)^{SiC}$ structure (see text), and (d)-(f) the $(C-C)_1^{SiO_2}$ structure. The band extrema are aligned to the electrostatic potential. The shifts of the valence band between the different functionals are indicated. In (d)-(f), the band extrema of SiC are also indicated. Energies are given in eV.

the functional used indicate that they cannot be used to describe accurately the electronic structure of defects. However, they constitute an adequate step to get a qualitative picture from which trends can be extracted. In the present case, the comparison between the positions of the Kohn-Sham energy levels and their corresponding charge transition levels indicates that the C-C pair defects featuring unoccupied Kohn-Sham energy levels slightly above the SiC conduction band are expected to have $0/-1$ and $-1/-2$ charge transition levels in the upper part of the SiC band gap. Based on this indication, we calculated the charge transition levels of the SiC-C-C-SiC structure in bulk SiC (cf. Fig. 4.3 where the structure is represented at the interface). This structure presents an occupied level close to

the valence band of SiC and the unoccupied level associated with the C-C part is expected to be located slightly above the SiC conduction. As in the calculation at the interface, the unoccupied Kohn-Sham energy levels associated with the C-C pair situate above the conduction band of SiC and cannot be located. However, Figure 4.14 (c) shows that the $0/-1$ and $-1/-2$ charge transition levels locate just below the conduction band of SiC. This confirms that the Kohn-Sham energy levels cannot be used to describe accurately the electronic structure of defects but can provide useful indications in the investigation of defects.

Charge transition levels at the interface

To evaluate the location of the charge transition levels at the interface from bulk calculations, two effects must be taken into account. First, the structural relaxation of the defect models can be different whether the defect locates in the bulk or at the interface. Second, the charge transition levels determined in the bulk models do not take into account the image charge interaction when the charged C-C pair defect is modeled at the interface.

The structural relaxation of the C-C pair in SiC is expected to be similar whether it is modeled in the bulk or at the interface because of the hardness of the substrate. Indeed, the crystalline substrate does not undergo any major modification upon insertion of a carbon interstitial in SiC in either model. Accordingly, the Kohn-Sham levels differ by at most 0.2 eV between the C-C pair structures modeled in SiC at the interface and in bulk SiC. The comparison between the Si$_2$-C=C-Si$_2$ structure in SiO$_2$ at the interface and the (C-C)$_1^{\text{SiO}_2}$ structure in bulk SiO$_2$ is less straightforward, as the angles between the planes of the two sp^2 hybridized carbon atoms differ in the two structures. However, a quantitative picture is provided in Fig. 4.9, which shows the evolution of the highest occupied and lowest unoccupied levels in the C$_2$(SiH$_3$)$_4$ molecule with respect to the angle between the planes of the two sp^2 hybridized carbon atoms. For the angles in structures (C-C)$_1^{\text{SiO}_2}$ and Si$_2$-C=C-Si$_2$, the molecular model predicts a difference between the highest occupied and lowest unoccupied levels of 4.6 and 3.1 eV, respectively, to be compared with the actual values of 4.6 and 3.0 eV. Therefore, the structural relaxation of the C-C pair in SiO$_2$ whether in the bulk model or in the interface model is expected to be similar. Overall, the difference between the structural relaxations in the bulk and interface systems appears small and will be neglected.
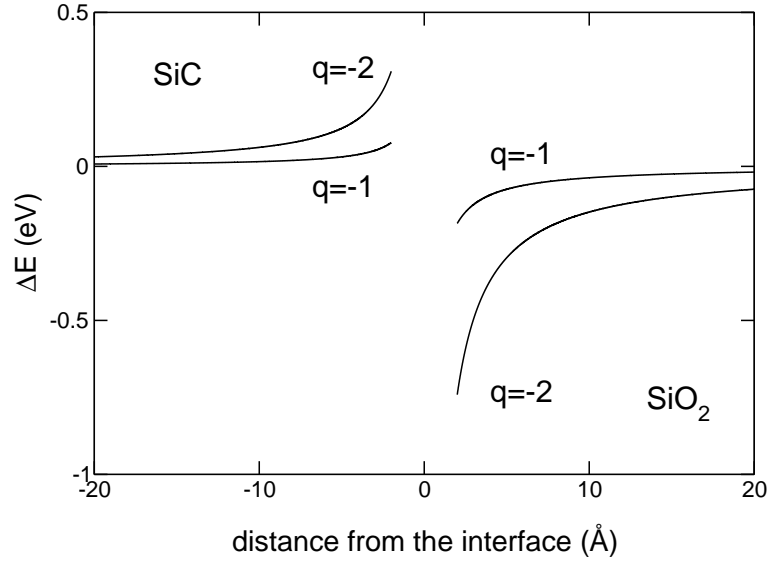
Figure 4.15: Corrections to the charge transition levels in the SiC/SiO$_2$ interface model as calculated with classical electrostatics.

The extra energy contribution due to the dielectric discontinuity at the interface can then be estimated through a simple classical model. We consider a system of two adjacent semi-infinite dielectrics with dielectric constants ϵ_{SiC} and ϵ_{SiO_2}. A point charge q is embedded first in the semi-infinite SiC substrate (for example) at a distance d from the interface. Using the image method, an image charge q' symmetric to q with respect to the interface plane is responsible for a potential V given by:

$$V = \frac{1}{\epsilon_{SiC}} \frac{q'}{2d}, \quad \text{with} \quad q' = -\left(\frac{\epsilon_{SiO_2} - \epsilon_{SiC}}{\epsilon_{SiO_2} + \epsilon_{SiC}}\right) \cdot q. \tag{4.2}$$

Finally, the electrostatic energy ΔE due to the charge q at a distance d from the interface is given by $\Delta E = \frac{1}{2} q \cdot V$. When q is placed in SiO$_2$, the same equation applies provided the dielectric constants are exchanged.

Fig. 4.15 shows the electrostatic energy ΔE as a function of the distance of the charge from the interface. The curve is interrupted at a distance of 2 Å because of the artificial divergences occurring in classical electrostatics. Due to the higher dielectric constant of SiC, the image charge interaction for a charge q placed in the substrate is only a fraction ($\epsilon_{SiC}/\epsilon_{SiO_2} \sim 2.4$) of that for q placed in the oxide. It should also be noted that the value of the image charge interaction scales as q^2 which makes it particularly important when the C-C pair is doubly charged.

Figure 4.16 shows schematically how the energy range spanned by the $0/-1$ and $-1/-2$ charge transition levels at the SiC/SiO$_2$ interface can be estimated
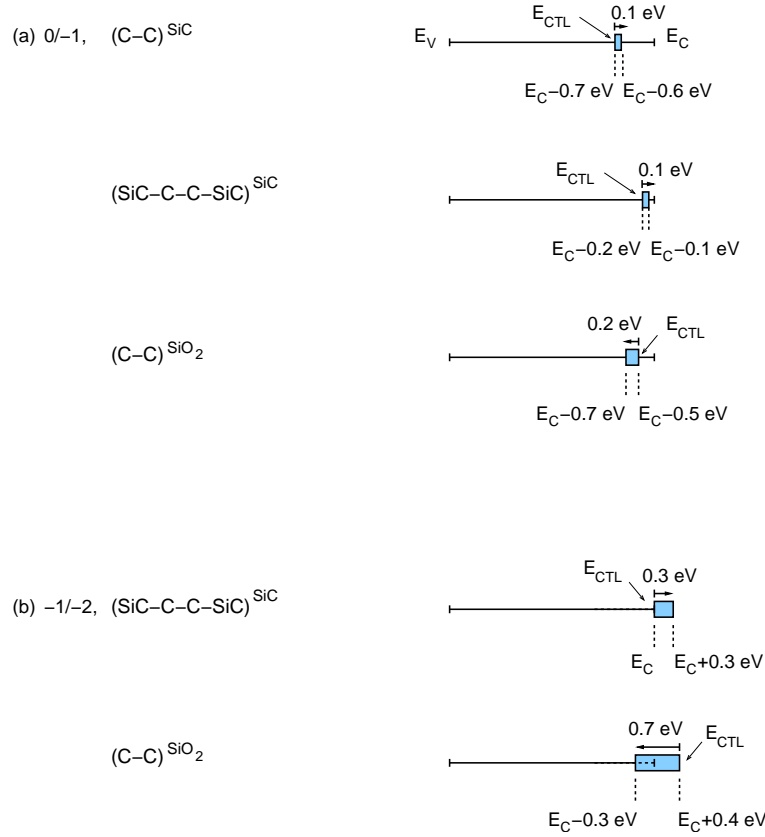
Figure 4.16: Schematic of the determination of the energy range spanned by the (a) $0/-1$ and (b) $-1/-2$ charge transition levels at the SiC/SiO$_2$ interface from bulk calculations and electrostatics corrections.

from bulk calculations and classical electrostatics corrections. For each charge transition level, its calculated value in bulk SiC or bulk SiO$_2$ (averaged over the two cases sharing similar values) is positioned with respect to the SiC band edges. The classical electrostatics correction plotted in Fig. 4.15 is then determined from Eq. (4.2) at a distance $d = 2$ Å from the interface and added to the charge transition level calculated in bulk SiC to account for the image charge interaction when the defect is close to the interface. This determines the energy range that the charge transition level can span. Figure 4.16 shows that the $0/-1$ charge transition level is expected to locate about $E_C^{SiC}-0.7$ eV to $E_C^{SiC}-0.1$ eV at the interface, where E_C^{SiC} is the energy of the SiC conduction band, while the $-1/-2$ charge transition level extends from $E_C^{SiC}-0.3$ eV to $E_C^{SiC}+0.4$ eV . The overlap of the possible positions of the C-C charge transition levels finally ranges from $E_C^{SiC}-0.7$ eV to $E_C^{SiC}+0.4$ eV. The charge transition level calculations indicate that the C-C pair defect contributes to the high density of defect states in the upper part of

the SiC band gap. However, two characteristics of the C-C pair defect make it an inadequate candidate for the sharp peak of the NITs. First, its defect levels locate both in the lower and upper part of the band gap, whereas the peak of the NITs does not present any correlation with the defect levels in the lower part of the SiC band gap. Second, the peak of the NITs is sharp, whereas the distribution of the C-C pair defects in the upper part of the SiC band gap is broad. We therefore conclude that the C-C pair is not a contributor to the NITs just below the SiC conduction band.

In this section, we identified the C-C pair defect in a variety of configurations as the origin of Kohn-Sham energy levels in the lower and upper part of the SiC band gap. To improve the description of the electronic structure of the defects, we calculated the charge transition levels in bulk models. The comparison between Kohn-Sham levels at the interface and charge transition levels in the bulk can be useful for defect identification. The C-C pair defects were identified as contributors to the high density of defect states in the upper part of the SiC band gap, but these defects were excluded as possible candidates to the sharp peak of NITs just below the SiC conduction band because of their broad energy distribution and their correlation with defect levels in the lower part of the SiC band gap.

4.3 Oxygen-related defects

4.3.1 The hydrogen bridge defect

Intrinsic defects in SiO_2 [28, 29, 30, 36, 37] have been proposed to account for the D_{it} in the upper band gap of SiC. These so-called near-interface traps (NITs) have been detected both in Si- and SiC- based MOS structures and their energy levels appear to be fixed with respect to the conduction band of SiO_2. Photon simulated tunneling measurements on SiC-based MOS structures revealed a mean energy barrier of 2.8 eV, indicating that these negatively charged NIT levels are positionned 0.1 eV below the conduction band of $4H$-SiC.

We here investigate the hydrogen complexed oxygen vacancy (or hydrogen bridge defect) proposed in the litterature as the possible origin of the NITs [28, 36]. The defect is created in the 72-atom bulk SiO_2 model introduced in Sec. 3.1.2. One hydrogen atom is located at an oxygen vacancy site and bridges two silicon atoms as shown in Fig. 4.17.

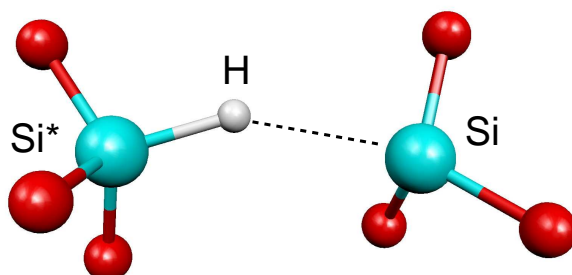Four different configurations of the hydrogen bridge defect were investigated.

Figure 4.17: Ball-and-stick representation of the hydrogen bridge defect. Si* refers to the silicon atom closer to the bridging hydrogen.

For each configuration, the structure in three charge states (-1, 0, and $+1$) is fully relaxed. The averaged structural parameters for the hydrogen bridge defect structure are summarized in Table 4.6. One can notice that in the negative and neutral charge states, the position of the hydrogen atom is strongly asymetric with respect to the two silicon atoms. Its distances to the silicon atoms differ by ~35% and it does not locate on the line joining them. When the system acco- modates a positive charge, the distances between the hydrogen and the silicon atoms differ much less and the hydrogen atom locates closer to the Si*-Si line. The standard deviations of the angle and the distances show that the hydrogen bridge defect features slightly different configurations depending on the environ- ment.

We then calculate the charge transition level as presented in Sec. 4.2.6. The results are summarized in Table 4.7 for PBE and PBE0[35] calculations and are

Table 4.6: Structural parameters for the hydrogen bridge defect structure averaged over four different configurations in three different charge states. Si* refers to the silicon atom closer to the bridging hydrogen. Standard deviations are given in parentheses.

	-1	0	$+1$
Si*-Si (Å)	3.24 (0.27)	3.18 (0.20)	3.09 (0.20)
Si*-H (Å)	1.51 (0.07)	1.49 (0.02)	1.60 (0.07)
Si-H (Å)	2.34 (0.32)	2.32 (0.09)	1.88 (0.28)
$\angle$ Si*-H-Si ($^\circ$)	113.2 (7.6)	119.8 (17.6)	129.2 (20.6)

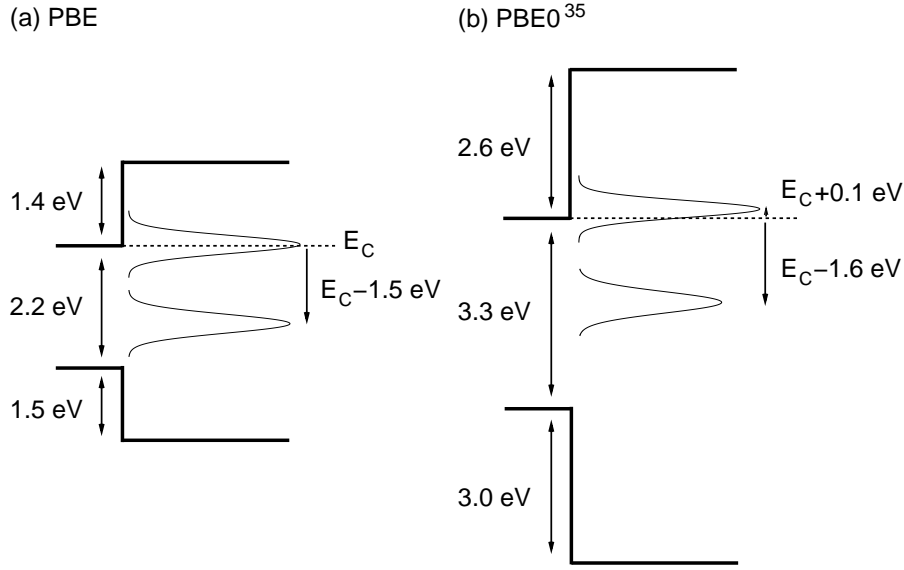(a) PBE   (b) PBE0 [35]

Figure 4.18: Gaussian distributions of the hydrogen bridge charge transition levels according to values reported in Table 4.7 in a schematic of the band gap evolution across the interface model. The electrostatic potential is aligned for the two calculations.

schematically shown in Fig. 4.18. As discussed before, the PBE and PBE0[35] charge transition levels agree well when expressed relative to the electrostatic potential. At the PBE0[35] level, the +1/0 and 0/−1 charge transition levels are both located in the upper part of the SiC band gap and are separated by only 1.7 eV. The 0/−1 charge transition location agrees within 0.2 eV with the PST experiments measuring a sharp peak of trap defects 0.1 V below the conduction band. However, the +1/0 charge transition level of the hydrogen bridge defect does not appear in the density of defect states represented in Fig. 1.5. The hydrogen bridge defect can therefore not account for the high density of defect states just below the conduction band characterized by a unique sharp peak. An oxide defect featuring solely one charge transition level in the upper part of the SiC band gap and no correlation with defect levels in the mid/lower part of the band gap still

Table 4.7: Charge transition levels calculated at the PBE and PBE0[35] levels. The reference is the SiO$_2$ valence band. Standard deviations are given in parentheses.

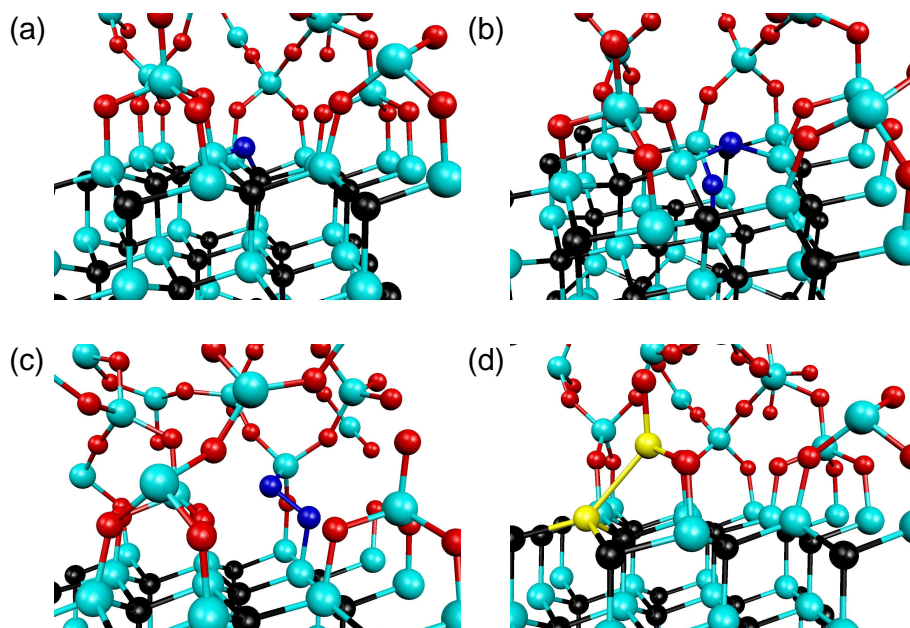|	+1/0	0/−1
PBE	2.35 (0.17)	3.88 (0.16)
PBE0[35]	4.73 (0.19)	6.40 (0.15)

Figure 4.19: Ball-and-stick representations of four oxygen-related defects at the interface (cf. text for details).

remains to be identified.

4.3.2   Oxygen interstitials and oxygen vacancy

We then investigate other oxygen-related defects at the interface through their Kohn-Sham energy levels as a first step. During the oxidation, a single oxygen atom could slip in a Si-C bond of the substrate [Fig. 4.19 (a)]. Or one oxygen atom of a O_2 molecule could replace one carbon atom of the substrate while the second oxygen incorporates between two of the silicon atoms previously bonded to the replaced carbon atom [Fig. 4.19 (b)]. An additional oxygen atom could also incorporate in a Si-O-Si bond, thereby forming a Si-O-O-Si bridge [Fig. 4.19 (c)]. Finally, an oxygen vacancy can lead to a Si-Si bond [Fig. 4.19 (d)].

These four oxygen-related defect structures modeled at the interface benefit from the strain release due to the bond reduction at the interface. They feature small structural relaxations of the defect environment compared to the defect-free structure. For example, the single interstitial oxygen atom in a Si-C bond [Fig. 4.19 (a)] buckles out of the interface plane and has regular Si-O=1.60 Å and C-O=1.46 Å bond lengths. The replacement of one carbon atom by an oxygen atom together with the insertion of another oxygen atom between two of silicon atoms previously bonded to the replaced carbon atom leads to a structure presenting

average Si-O bond length and Si-O-Si angle of 1.65 Å and 141°, respectively, very close to the corresponding values of 1.64 Å and 137° for the bulk oxide model [Fig. 4.19 (b)]. The Si-O-O-Si bridge [Fig. 4.19 (c)] presents a dihedral angle of 99.3°, and features Si-O and O-O bond lengths of 1.68 Å and 1.50 Å, respectively. Finally, the oxygen vacancy [Fig. 4.19 (d)] leads to a Si-Si bond of length 2.41 Å.

The electronic structures of these four structures do not reveal any occupied or unoccupied levels in the band gap. These oxygen-related defects presenting regular bonding parameters do not lead to any degradation of the electronic properties of the SiC/SiO_2 interface.

The oxygen-related defects studied in this section cannot account for the high density of defect states near the SiC conduction band. The hydrogen bridge defect, proposed in the literature as a possible candidate, can be ruled out due to the presence of the two charge transition levels in the upper part of the SiC band gap, where the NITs present a unique peak.

4.4 Passivation of the C-C pair defect

Recently, it was shown that a post oxidation anneal in nitric oxide followed by a post metallization anneal in hydrogen resulted in a reduction of the trap density near the conduction band by over an order of magnitude [68, 69]. It was suggested that this treatment could eliminate the threefold coordinated atoms responsible for the high interface trap density either by H-passivation or replacement by N [69, 70]. In this section, we carry out total energy calculations showing that the passivation of the C-C pair defect by hydrogen and nitrogen is thermodynamically favorable.

4.4.1 Passivation of the C-C pair defect by hydrogen

We use here the C-C pair defect modeled in SiC at the interface (cf. Sec. 4.2.1). To calculate the energy gain upon passivation by H_2, we perform two separate calculations. In the first calculation, a H_2 molecule is introduced in a void in the oxide of the defect-free interface model. In the second calculation, one hydrogen atom is placed in the vicinity of each carbon atom of the C-C pair. The relaxed structure of the passivated C-C pair defect is shown in Fig. 4.20. Only minor rearrangements occur, such as the increase of the C-C length by ~8% and the decrease of the angle between the planes of the two sp^2 carbon atoms from 89.3°
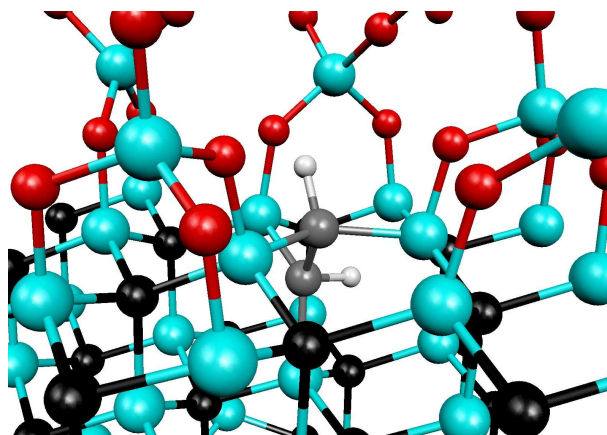
Figure 4.20: Ball-and-stick representation of the interfacial C-C pair defect passivated by H atoms.

to 80.4°. The C-H bonds have a regular length of 1.09 Å and the dihedral angle ∠ H-C-C-H is 88.2°.

The total energy difference of the two relaxed structures indicates an energy gain of 2.5 eV upon passivation of the C-C pair defect by hydrogen. However, as mentionned in a recent study [56], it should be noted that the two C-H bonds point in opposite directions, suggesting that a large energy barrier is involved when an H$_2$ molecule is introduced to passivate the defect (the passivation of the two carbon dangling bonds cannot be a one-step process because of the distance separating them). Indeed, the passivation by atomic hydrogen generated by letting H$_2$ pass through a transition-metal layer was shown to be more effective than the passivation by molecular hydrogen [56]. Although further studies would be needed to calculate the reaction path of the H$_2$ dissociation and the passivation by atomic hydrogen, the calculations presented here confirm that the passivation of C-C dangling bonds is thermodynamically favorable.

4.4.2   Passivation of the C-C pair defect by nitrogen

We now turn to the passivation of the carbon dangling bonds by nitrogen. The valence shell of nitrogen contains one electron more than the valence shell of carbon. When a nitrogen atom is threefold coordinated, it has a lone pair instead of a dangling bond in the case of a threefold coordinated carbon atom. Replacing the carbon atoms of the C-C defect pair with nitrogen atoms is therefore expected to lead to the removal of defect levels associated with the carbon dangling bonds. As shown in Fig. 4.21, we perform three calculations in which (1) the C-C pair defect locates in SiC at the interface, (2) one nitrogen atom replaces one carbon
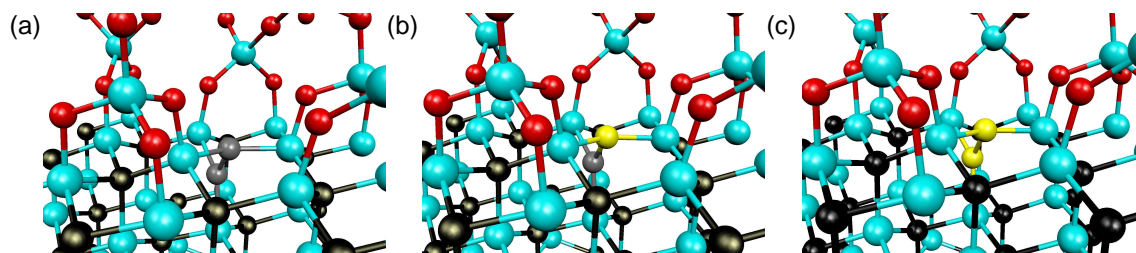
Figure 4.21: Ball-and-stick representations of (a) the interfacial C-C pair defect, (b) the interfacial C-N pair in which one carbon atom of the C-C pair defect is replaced by one nitrogen atom (yellow), and (c) the interfacial N-N pair replacing the C-C pair defect.

atom of the C-C pair, and (3) the N-N pair replaces the C-C defect pair. Two extra calculations, in which either a CO or a NO molecule, respectively, are introduced in a void of the oxide of the defect-free interface, model complete the set of calculations needed to determine the energy gains associated with the replacement of carbon by nitrogen atoms.

No major rearrangement occur upon replacement of one or two carbon atoms of the C-C pair by nitrogen atoms. The total energy differences indicate an energy gain of 2.7 eV and 2.3 eV when one and two carbon atoms of the C-C pair are replaced by nitrogen atoms, respectively. Although the study of the chemical reaction path is needed to determine the kinetics of the C-C pair passivation by nitrogen, these calculations nevertheless indicate that this passivation is thermodynamically favorable.

Total energy calculations show that the C-C pair passivation by either hydrogen or nitrogen is favorable. Only one C-C pair configuration was studied here and we expect that some transition states occurring upon C-C passivation may involve high energy barriers. However, the high energy gain caused by the passivation makes it thermodynamically favorable.

4.5   Conclusions

In this chapter, we investigated possible defect candidates for the high density of defect states near the SiC conduction band. The C-C pair defect involving sp^2 hybridized carbon atoms in bulk SiC was identified as the origin of occupied Kohn-Sham energy levels in the low/mid part of the SiC band gap but also of unoccupied levels in the upper part of the semiconductor band gap. The electronic structure of different C-C pairs configurations in SiC and in SiO_2 were then investigated at the SiC/SiO_2 interface through their Kohn-Sham energy levels. Despite

their structural differences, their overall electronic structures followed a similar pattern as that in bulk SiC. Charge transition levels were then calculated in bulk SiC and bulk SiO$_2$ and were found to locate in the vicinity of the SiC conduction band gap. The $0/-1$ and $-1/-2$ charge transition levels of the C-C pair defect at the SiC/SiO$_2$ interface were estimated through bulk calculations and a classical electrostatic model, and were found to locate between 0.7 eV below and 0.4 eV above the SiC conduction band. The C-C pair defect could therefore account for a part of the high density of defect states near the SiC conduction band. However, its broad distribution together with the correlation of its occupied and unocupied defect levels makes it an inadequate candidate for the sharp peak of the NITs close to the SiC conduction band.

The comparison between the positions of the Kohn-Sham energy levels and their corresponding charge transition levels for two C-C pair defect structures in the bulk model structures showed that the consideration of the Kohn-Sham energy levels alone for the accurate identification of defect levels is not reliable. However, they prove useful to determine trends. In the present case, their position with respect to their corresponding charge transition levels indicates that C-C pair defects with unoccupied Kohn-Sham energy levels slightly above the SiC conduction band can have their $0/-1$ and $-1/-2$ charge transition levels in the vicinity of the SiC conduction band. The study of the C-C pair in molecules shows that the chemical nature of the C-C pair neighbors have an influence on the Kohn-Sham levels, and suggest the location of the respective charge transition levels.

It should be noted that the estimation of the position of the charge transition levels at the interface from the bulk calculations relies on the assumption that the structural relaxations are similar in both models. However, some configurations at the interface cannot be reproduced in the bulk models. Calculations of charge transition levels directly at the interface appear therefore necessary. However, this requires taking care of the spurious contribution to the total energy from the interaction of periodic charges in these systems.

The charge transition levels of the hydrogen bridge defect were then investigated. The $0/-1$ charge transition level was found to locate in the close vicinity of the SiC conduction band where the NITs show a sharp peak. However, the $+1/0$ charge transition level located 1.6 eV below the SiC conduction dismissed it as a contributor to the NITs.

Finally, the passivation of the C-C pair defect by hydrogen and nitrogen was

studied. The total energy calculations established that both the passivation by hydrogen and the passivation by nitrogen are thermodynamically favorable.

In conclusion, several types of defects that could contribute to the high density of defect states near the SiC conduction band were identified. However, the main source of the NITs could not be identified and remains unknown.

Chapter 5

Epitaxial SiC/SiO$_2$ interfaces

In this chapter, we focus on an alternative approach explored by experimental research to go beyond conventional pre- and post-oxidation treatments to obtain SiC/SiO$_2$ interfaces with a reduced density of interface states. The preparation of hexagonal SiC surfaces by etching in hydrogen flow was shown to result in the formation of highly ordered monolayers of SiO$_2$ [81, 82]. In the two proposed epitaxial structures, the bond angles and distances of the silicate epitaxial adlayer agree well with those of bulk SiO$_2$. The first epitaxial structure of this sort has been proposed by Bernhardt *et al.* [81]. Silicon dangling bonds occur at the interface because of the bond density reduction between SiC and SiO$_2$. These bonds are imagined to be saturated by hydrogen atoms. The semiconductor surface being passivated, it preserves its perfect order in air, leading to an atomically abrupt interface between the SiC and the SiO$_2$ adlayer [in the following, this structure will be referred to as SiC/SiO$_2$(epi)] [81]. Shirasawa *et al.* [82] performed a subsequent annealing in nitrogen atmosphere leading to the formation of a silicon oxynitride epitaxial layer [82]. A hetero-double-layer structure, consisting of a silicate monolayer attached to a silicon nitride monolayer via Si-O-Si bridge bonds, is then obtained. This structure (referred to as the SiC(N)/SiO$_2$(epi) structure in the following) does not contain dangling bonds and is robust against air exposure [82]. The measured scanning tunneling spectroscopy (STS) current-voltage characteristic on the epitaxial layer exhibits a band gap of ∼9 eV, comparable to that of bulk SiO$_2$ [82]. This electronic property appears particularly intriguing since the silicate layer only extends over ∼4 Å [82].

In this chapter, we first describe the structural differences of the two interface structures based on $6H$-SiC(0001) and composed of an epitaxial silicon oxide layer [81] and an oxynitride layer [82], as proposed by Bernhardt *et al.* [81]

and by Shirasawa *et al.* [82], respectively. We also consider two models of the SiC/SiO$_2$ interface (cf. Ch. 3) with thick oxides, one of which incorporating a nitrogen layer at the interface as in the SiC(N)/SiO$_2$(epi) structure. These models will be used for comparison in Sec. 5.3. We then simulate scanning-tunneling-microscopy (STM) images of filled and empty states of the epitaxial oxide layer in the model proposed by Shirasawa *et al.*, finding good agreement with their experimental counterparts [82]. The evolution of the planar-averaged local density of states across the interface structures is then addressed and we find that the band gap of the SiC(N)/SiO$_2$(epi) structure opens up at a short distance from the substrate. Two properties of the SiC(N)/SiO$_2$(epi) structure contribute to this effect. The presence of the nitrogen layer is responsible for a band-gap opening occurring already in correspondence of the last layers of the SiC substrate and for its evolution until a distance of about ∼2.5 Å from the interface, thereby mainly affecting the electron states which lie close to the band edges of bulk SiC. The high potential-energy barrier represented by the external surface of the epitaxial oxide causes a further band-gap opening but is effective only in correspondence of the last two layers of the epitaxial silicate and affects electron states with energies close to the band extrema of SiO$_2$. The latter effect is enhanced in the presence of an interfacial nitrogen layer. Therefore, the combined effects of the thinness of the epitaxial silicate layer and of the presence of the interfacial nitrogen layer account for the origin of the large band gap experimentaly observed at the SiC(N)/SiO$_2$(epi) interface.

5.1   Computational settings

We describe the electronic structure using the generalized gradient approximation proposed by Perdew, Burke, and Ernzerhof (PBE) for the exchange and correlation energy [116]. For the valence electron wave functions, we used a plane-wave basis set with a cutoff energy of 70 Ry. For all atoms, core-valence interactions were described by Troullier-Martins normconserving pseudopotentials [150] in the Kleinman-Bylander form [149]. The Brillouin zone was sampled at the Γ point. This approach also provides atomic forces that were used to carry out structural relaxations. To achieve an improved description of band gaps [135, 156], we then adressed the electronic properties using the hybrid density functional PBE0 [130] in which 25% of the PBE exchange interaction is replaced by Hartree-Fock exchange. We took care of the integrable divergence of the exchange term by

extending the methods in Ref. [151] to Γ-point sampling. We here used the CPMD package [152, 159]. Simulated STM images are topographs of constant local density of states $\rho(x, y, z; \epsilon) = \rho_0$, where ϵ corresponds to the Fermi level off set by the experimental tunneling voltage [182]. The STM images were created with the DACAPO package [183, 184].

5.2 Model structures

Our study comprises four model structures involving the $6H$-SiC(0001) substrate and SiO$_2$ overlayers. In two of the model structures the oxide is epitaxial, while it is amorphous and extended in the other two.

The epitaxial models correspond to the structures generated by Bernhardt *et al.* [81] and Shirasawa *et al.* [82]. The former is nitrogen free [SiC/SiO$_2$(epi), Fig. 5.1(a) and (b)] while the latter incorporates a full monolayer of nitrogen atoms at the interface [SiC(N)/SiO$_2$(epi), Fig. 5.1(c) and (d)]. In these models, the SiC(0001) substrate exposes a Si-terminated SiC(0001) surface and contains a periodic 3×4 repeat unit in the plane of the interface. The transverse cell parameters were chosen to match the equilibrium lattice constants of bulk $6H$-SiC. The SiC substrate is composed of 12 layers, the bottom layer being H terminated. In the model structure proposed by Bernhardt *et al.* [81], one in every four Si atoms of the last substrate plane exposes a H-saturated Si bond towards the epitaxial oxide. The other Si atoms of this plane form Si-O-Si bridging bonds with an epitaxial silicate monolayer. The SiC(N)/SiO$_2$(epi) model interface was constructed by following Shirasawa *et al.* [82]. The presence of the nitrogen layer contributes to achieve a bond density reduction at the interface. Hence, the substrate connects to the same epitaxial silicate monolayer as in the SiC/SiO$_2$(epi) model, without any bond being saturated by hydrogen. For this model, average structural parameters for

Table 5.1: Bond lengths and bond angles for the relaxed SiON epitaxial layer, compared to experimental values [82]. The Si-O-Si angle close to $180°$ corresponding to the vertical Si-O-Si unit is not considered. Si* indicates a Si atom belonging to the SiC substrate.

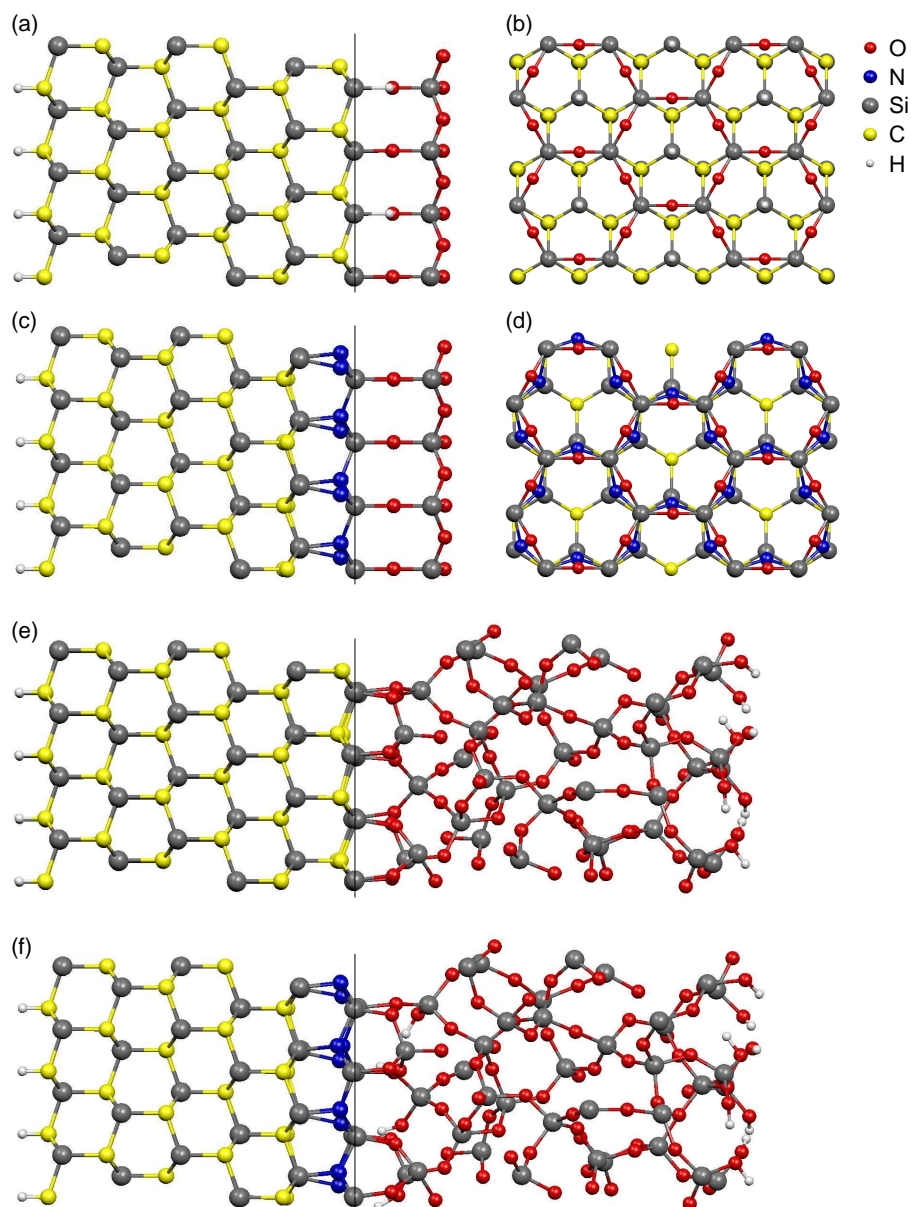|	Si-O (Å)	Si-N (Å)	$\angle$ Si-O-Si	$\angle$ Si-N-Si	$\angle$ Si-N-Si*
Present	1.63	1.75	141°	126°	114°
Expt.	1.63	1.75	143°	125°	114°

Figure 5.1:   (color-online) Ball-and-stick representation of the SiC/SiO$_2$ model structures considered in this chapter: (a) side and (b) top view of SiC/SiO$_2$(epi), (c) side and (d) top view of SiC(N)/SiO$_2$(epi), and side views of (e) SiC/SiO$_2$ and (f) SiC(N)/SiO$_2$. The vertical lines give the adopted origin of the spatial coordinate evolving in a direction perpendicular to the interfacial plane. For clarity, the top views in (b) and (d) were generated for periodically repeated unit cells.

bond lengths and bond angles were found to show excellent agreement with experimental values [82] (cf. Table 5.1).

For comparison, we also considered model structures containing thick oxide layers, either with or without an interfacial nitrogen layer. For this purpose, we generated a 6H(0001)-SiC/SiO$_2$ model interface on the basis of the 4H(0001)-
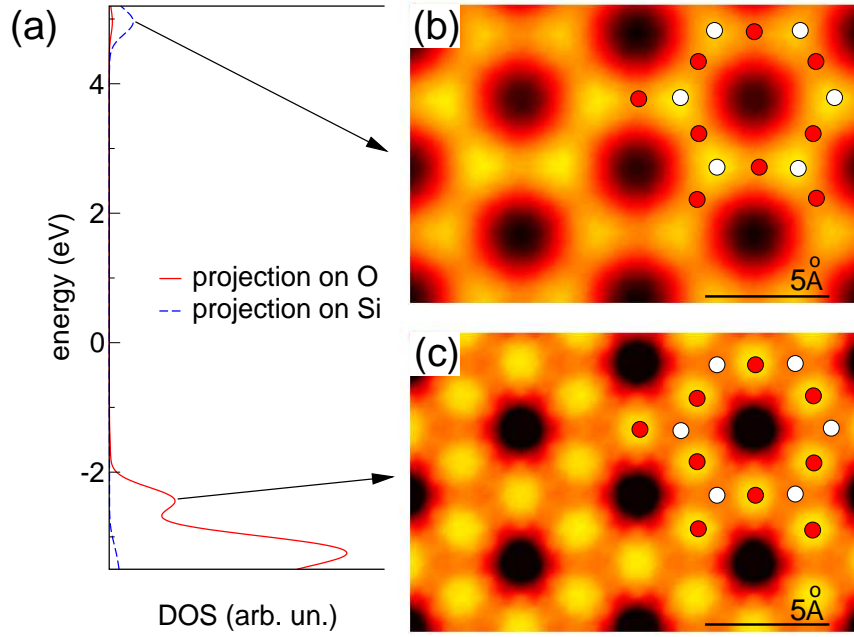
Figure 5.2: (a) Density of states (DOS) projected onto Si and O atoms of the outermost atomic layer of the epitaxial oxide in the SiC(N)/SiO$_2$(epi) structure. The STM images correspond to (b) empty and (c) filled states located close to the oxide band gap. The insets show the atomic positions of the Si (white) and O (red) atoms.

SiC/SiO$_2$ interface modeled previously. [cf. Fig. 5.1(e), Ch. 3]. In this model, amorphous SiO$_2$ is connected to an abrupt SiC substrate without showing any coordination defect. The thickness of the oxide layer amounts to 16 Å. In the following, we refer to this model as SiC/SiO$_2$. This structure was then modified in order to incorporate an interfacial nitrogen monolayer following the construction in the SiC(N)/SiO$_2$(epi) model. The uppermost carbon atoms in the substrate were substitutionally replaced by nitrogen atoms. To account for the threefold coordination of the nitrogen atoms, four silicon atoms of the last substrate plane were then removed and the resulting undercoordinated oxygen atoms were saturated by hydrogen atoms [cf. Fig. 5.1(f)]. This model is referred to as SiC(N)/SiO$_2$.

5.3   Electronic structure

Further support to the model structure proposed by Shirasawa *et al.* [82] comes from the analysis of the local density of states. Figure 5.2 shows the density of states projected on Si and O atoms belonging to the outermost oxide layer. The

highest occupied states show a predominant oxygen character and correspond to O $2p$ orbitals, while the lowest unoccupied states are primarily related to Si atoms. Consequently, simulated STM images of filled and empty states give bright spots on O and Si atoms, respectively, in agreement with experiment [82].

Despite the occurrence of a single silicate layer in the epitaxial oxide, the STS current-voltage characteristic showed a band gap that closely agrees with that of bulk SiO$_2$ [82]. To address this issue, we investigated the planar averaged local density of states:

$$D(z; \epsilon) = 2 \sum_n |\langle z|\psi_n\rangle|^2 \delta(\epsilon - \epsilon_n), \tag{5.1}$$

where z indicates a coordinate along the interface normal, $|\langle z|\psi_n\rangle|^2$ corresponds to the electron density integrated in xy planes, the factor of 2 accounts for the spin degeneracy, and ψ_n are the Kohn-Sham eigenstates of energy ϵ_n. In the calculations, the Dirac delta functions in Eq. (5.1) were replaced by Gaussian functions with a standard deviation of 0.02 eV.

From the local electronic density of states $D(z; \epsilon)$, we obtained the evolution of the valence band maximum (VBM) and conduction band minimum (CBM) across the interface as follows. For every value of z, we determined the local band edges by requiring that the number of states falling between midgap and the band edge equals a threshold value of 0.03 states/Å^3 [172]. The threshold value was determined by imposing that the band gap in bulk SiC is accurately recovered. For a model of bulk amorphous SiO$_2$ [157], we found that this threshold value still gives the band gap within 0.1 eV. Therefore, it is expected that this choice of threshold value accurately describes the transition across the semiconductor-oxide system.

We report in Fig. 5.3(a) the evolution of the conduction and valence band edges across the two epitaxial structures, SiC/SiO$_2$(epi) and SiC(N)/SiO$_2$(epi), as calculated within the PBE0 scheme. On the semiconductor side of the SiC/SiO$_2$(epi) structure, we found a band gap for 6H-SiC of 3.8 eV in close agreement with the bulk value of 3.7 eV. In the SiC(N)/SiO$_2$(epi) structure, the semiconductor features a larger band gap by $\sim$0.15 eV. The small differences with respect to the bulk values result from quantum confinement effects due to the finite thickness of the semiconductor layer in our models. In particular, the presence of a nitrogen layer appears to repel the conduction band states leading to an effectively thinner substrate layer. The band gap then progressively increases across the epitaxial oxide. This effect originates from the semiconductor states induced in the oxide
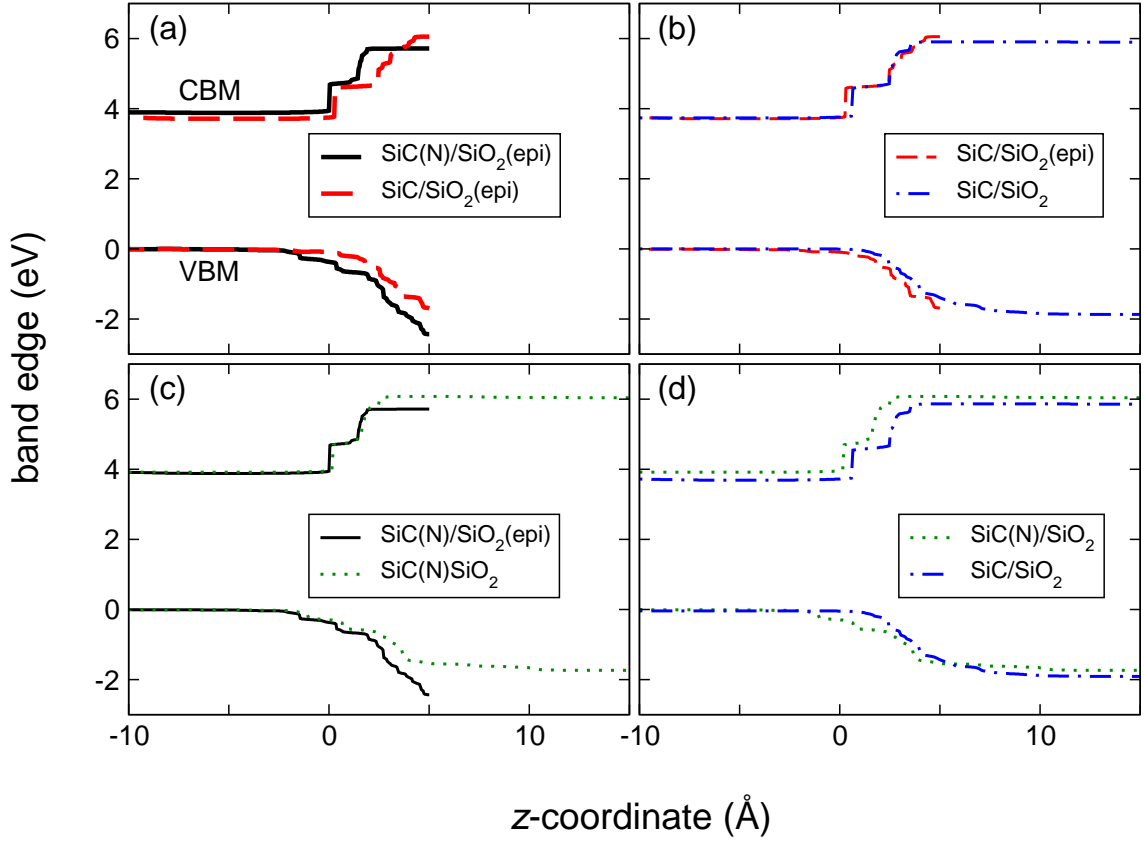
Figure 5.3: (color-online) Evolution of the conduction band minimum (CBM) and valence band maximum (VBM) for the SiC/SiO$_2$ model structures considered in this work: (a) SiC/SiO$_2$(epi) (dashed, red) vs SiC(N)/SiO$_2$(epi) (solid, black), (b) SiC/SiO$_2$(epi) vs SiC/SiO$_2$ (dashed-dotted, blue), (c) SiC(N)/SiO$_2$(epi) vs SiC(N)/SiO$_2$ (dotted, green), and (d) SiC/SiO$_2$ vs SiC(N)/SiO$_2$. The origin of the spatial coordinate corresponds to the outermost Si plane of the substrate (cf. Fig. 5.1). The energy scale is aligned to the local average potential in the bulk substrate.

band gap which decrease as they penetrate the oxide. For the SiC(N)/SiO$_2$(epi) structure, the calculated band gap has reached the value of 8.1 eV in correspondence of the last atomic layer of the epitaxial oxide. This value should be compared with the band gap of bulk SiO$_2$, for which we found 7.9 eV when calculated within the same PBE0 scheme. Our electronic structure theory therefore supports the experimental finding of a bulk-like band gap in correspondence of the uppermost silicate layer of the epitaxial oxide. In the SiC/SiO$_2$(epi) structure, the band gap starts to open at a smaller distance from the outer surface. Moreover, the band gap of bulk SiO$_2$ is not fully recovered in correspondence of the last atomic layer of the epitaxial oxide.

To highlight the effect of different oxide thicknesses, we performed comparisons between the two epitaxial structures and their respective bulk oxide coun-
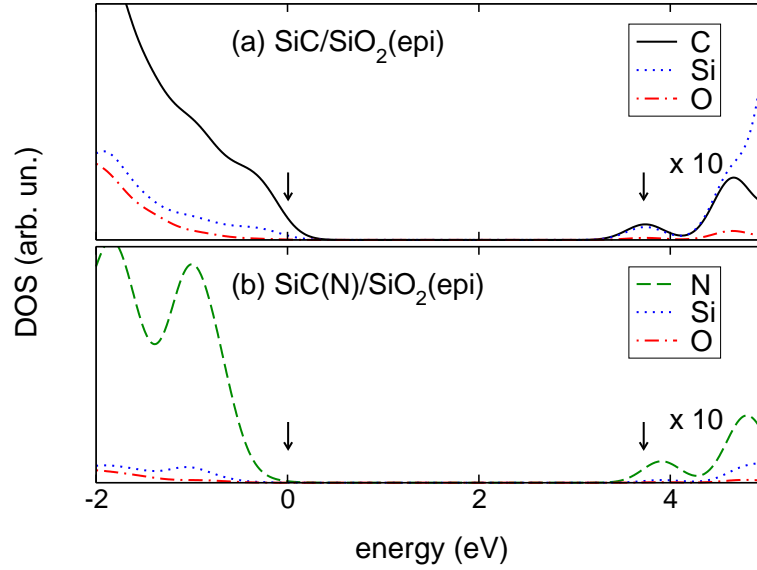
Figure 5.4: (color-online) Projections of the density of states (DOS) of (a) the SiC/SiO$_2$(epi) and (b) the SiC(N)/SiO$_2$(epi) model structures on the atoms belonging to the interfacial region, comprising the last double layer of the substrate and the first oxygen layer of the oxide. The arrows indicate the position of the band edges of the SiC/SiO$_2$(epi) model in correspondence of this double layer, as found in Fig. 5.3. The following labeling is used: C (black, solid), N (green, dashed), Si (blue, dotted), O (red, dashed-dotted). For clarity, the DOS of the conduction band is multiplied by a factor of 10 ($\times$10).

terparts. In Fig. 5.3(b), we compare the two structures that are nitrogen-free, SiC/SiO$_2$(epi) and SiC/SiO$_2$. We observe a similar band-gap opening occurring over identical distances for the two structures. This comparison shows that, in the absence of a nitrogen layer, the thinness of the epitaxial oxide has no significant effect on either the valence or the conduction band. Conversely, we compare in Fig. 5.3(c), the two structures featuring an interfacial nitrogen layer but different oxide thicknesses, SiC(N)/SiO$_2$(epi) and SiC(N)/SiO$_2$. Up to a distance of $\sim$2.5 Å from the interface, the band-gap opening in the two structures follows a similar trend, indicating that this behavior should be entirely ascribed to the presence of the nitrogen layer. The effect due to the thinness of the oxide layer becomes evident only in correspondence of the last two monolayers of the epitaxial oxide. The band gap of the thin oxide grows faster and to a slightly larger value than in the case of the thick oxide. We note that this effect should be contrasted with the nitrogen-free models where the thickness of the oxide does not affect the band gap opening in a significant way [cf. Fig. 5.3(b)].

The effect of the nitrogen layer is further investigated by comparing the two model structures with thick oxides, SiC(N)/SiO$_2$ and SiC/SiO$_2$ [Fig. 5.3(d)]. The

comparison of the band evolutions shows that the main differences due to the nitrogen layer are again observed in the region which extends up to a distance of ~ 2.5 Å from the interface.

In Fig. 5.4, we highlight the effect of the interfacial nitrogen monolayer by comparing the projected density of states of the two epitaxial structures. The considered atoms locate in the interfacial region, comprising the uppermost double layer of the substrate and the first oxygen layer of the oxide. When the nitrogen atoms are present, the band gap is enhanced, both valence and conduction band edges being determined by states carrying a predominant nitrogen character. The density of states projected on the silicon and oxygen atoms is correspondingly shifted away from the band edges.

5.4   Conclusions

We investigated the electronic properties of two epitaxial SiC/SiO_2(epi) and $SiC(N)$-$/SiO_2$(epi) structures which might show great potential for SiC-based electronic devices [81, 82]. The oxide structure of the latter interface proposed by Shirasawa *et al.* [82] is strongly supported by the good agreement between experiment and theory found for the structural parameters and STM images. We then investigated the origins of the band-gap opening experimentally observed at the $SiC(N)/SiO_2$(epi) interface [82]. Through the evolution of the planar-averaged local density of states across four model structures, we distinguished the effects of the thinness of the epitaxial oxide layer and of the occurrence of an interfacial nitrogen layer. The presence of the nitrogen layer is responsible for a band-gap opening occurring already in correspondence of the last layers of the SiC substrate and for its evolution until a distance of about ~ 2.5 Å from the interface. It thereby mainly affects the electron states which lie close to the band edges of bulk SiC. The high potential-energy barrier represented by the external surface of the epitaxial oxide causes a further band-gap opening but becomes operative only in correspondence of the last two layers of the epitaxial silicate and affects electron states with energies lying close to the band extrema of SiO_2. Our investigation shows that the latter effect is enhanced in the presence of an interfacial nitrogen layer. Thus, our study indicates that the origin of the large band gap observed experimentally should be attributed to the combined effect of the thinness of the epitaxial oxide layer and of the occurrence of the interfacial nitrogen layer.

Chapter 6

Conclusions

In this thesis we carried out a first-principles study of defects at the SiC/SiO_2 interface through hybrid functionals.

The theoretical modeling performed in this work contributes to the understanding of the nature of the defects responsible for the degradation of the electronic properties at the SiC/SiO_2 interface. The experimental information regarding the defect structures at the SiC/SiO_2 interface is scarce. The availability of atomic-scale quantum-mechanical modeling is therefore particularly helpful in this case. The comparison of atomic-scale experimental measurements with atomic-scale theoretical investigations can indeed show whether or not a particular defect model provides electronic properties relevant to the observed charge or trap. To provide a reliable comparison with experiment, the theoretical modeling of the defect at the interface must satisfy two conditions.

First, the structural parameters of the interface model must be similar to those of the experimental interface. We therefore set out to generate a model structure providing a realistic description of the majority bonding arrangements at the $4H(0001)$-SiC/SiO_2 interface. In this work we chose to consider an atomically abrupt interface which offers a realistic description of SiC/SiO_2 interfaces obtained through the oxidation of reconstructed SiC(0001) surfaces. The sequential use of classical and *ab initio* simulation methods allowed us to obtain a model structure in which not only the short-range structural parameters such as the bond lengths and bond angles, but also the global properties such as the oxide density remain close to typical experimental values.

Second, the band gaps and band offsets must be described accurately. To fulfill this condition, we investigated the electronic properties of the generated model interface using hybrid density functionals, which incorporate a fraction of the

Hartree-Fock exchange interaction. The use of such functionals was motivated by the necessity of accurately describing band gaps and band offsets, which are known to be poorly described by standard density functional schemes. Indeed, the identification of typical near interface defects is expected to mainly rest on the position of energy levels with respect to the relevant band edges. We used the following scheme to calculate accurately the band offsets. The band extrema of each of the two bulk components of the interface were first calculated through hybrid calculations incorporating the appropriate amount of Hartree-Fock exchange to recover experimental band gaps. The band extrema were then aligned to the electrostatic potential of the interface model, leading to band offsets that agree with their experimental counterparts within 0.1 eV.

The good structural properties and the accurate electronic description of our structure model make it a reliable model for the further study of defects and for the comparison of their properties with experimental measurements. Furthermore, the methodology applied to obtain a suitable model interface and the novel scheme providing a reliable description of the band gaps and band offsets are valuable tools that can be transferred to other systems. The use of hybrid density functionals providing an improved description of the electronic structure over standard functionals appears mandatory.

We then investigated possible defect candidates for the high density of defect states near the SiC conduction band. The C-C pair defect involving sp^2 hybridized carbon atoms was first modeled in bulk SiC. The electronic structure of this defect revealed occupied and unoccupied Kohn-Sham energy levels located in the lower and upper part of the SiC band gap, respectively. Different configurations of the C-C pair defect were then investigated in SiC and SiO_2 at the interface. Despite their structural differences, they all featured an electronic structure similar to that of the C-C pair modeled in bulk SiC. We then focussed on the formation energy of the C-C pair defect in its negative charge states. The $0/-1$ and $-1/-2$ charge transition levels of the C-C pair defect were calculated in bulk SiC and bulk SiO_2 and were found to locate in the vicinity of the SiC conduction band. The charge transition levels of the C-C pair defect at the SiC/SiO_2 interface were estimated through bulk calculations and a classical electrostatic model, and were found to locate between 0.7 eV below and 0.4 eV above the SiC conduction band. The C-C pair defect could therefore account for a part of the high density of defect states near the SiC conduction band. However, its broad distribution together

with the correlation of its occupied and unoccupied defect levels makes it an inadequate candidate for the sharp peak of the NITs close to the SiC conduction band.

The hydrogen bridge defect was then investigated as an intrinsic defect of SiO_2 that could contribute to the high density of defect states near the SiC conduction band. The $0/-1$ charge transition level was found to locate in the close vicinity of the SiC conduction band where the NITs show a sharp peak. However, the $+1/0$ charge transition level located 1.6 eV below the SiC conduction dismissed it as a contributor to the NITs.

Several types of defects that could contribute to the high density of defect states near the SiC conduction band were identified. However, the main source of the NITs could not be identified. The occurence of these trap states both at the SiC/SiO_2 and Si/SiO_2 interfaces suggests an intrinsic defect of the oxide. An oxide defect featuring solely one charge transition level in the upper part of the SiC band gap and no correlation with defect levels in the mid/lower part of the band gap still remains to be identified.

The comparison between the Kohn-Sham energy levels and their corresponding charge transition levels revealed that the former do not provide a reliable description of the electronic structure. They can be used to provide guidance on the study of defects, but it is preferable to describe defect levels through the determination of charge transition levels. In this work, the charge transition levels of the defects were performed in bulk models. Indeed, charged interface calculations in periodic slab systems are difficult to treat as the spurious contribution to the total energy from the interaction of periodic charges at the interface of different dielectric materials is hard to estimate. However, some configurations at the interface cannot be reproduced in the bulk models. Calculations of charge transition levels directly at the interface appear therefore necessary. A methodology taking care of the spurious contribution to the total energy from the interaction of periodic charges in these systems is needed.

In the last part of this thesis, we focussed on an alternative approach explored by experimental research to go beyond conventional pre- and post-oxidation treatments to obtain SiC/SiO_2 interfaces with a reduced density of interface states. We investigated the electronic properties of two epitaxial $6H$-SiC(N)/SiO_2(epi) and $6H$-SiC/SiO_2(epi) structures which might show great potential for SiC-based electronic devices. The oxide structure proposed for the SiC(N)/SiO_2(epi) is strongly

supported by the good agreement between experiment and theory found for the structural parameters and STM images. We then investigated the origins of the band-gap opening experimentally observed at the SiC(N)/SiO$_2$(epi) interface. Through the evolution of the planar-averaged local density of states across four model structures, we distinguished the effects of the thinness of the epitaxial oxide layer and of the occurrence of an interfacial nitrogen layer. The presence of the nitrogen layer is responsible for a band-gap opening occurring already in correspondence of the last layers of the SiC substrate and for its evolution until a distance of about $\sim$2.5 Å from the interface. It thereby mainly affects the electron states which lie close to the band edges of bulk SiC. The high potential-energy barrier represented by the external surface of the epitaxial oxide causes a further band-gap opening but becomes operative only in correspondence of the last two layers of the epitaxial silicate and affects electron states with energies lying close to the band extrema of SiO$_2$. Our investigation shows that the latter effect is enhanced in the presence of an interfacial nitrogen layer. Thus, our study indicates that the origin of the large band gap observed experimentally should be attributed to the combined effect of the thinness of the epitaxial oxide layer and of the occurrence of the interfacial nitrogen layer.

Bibliography

[1] J.J. Berzelius, Ann. Phys. (Leipzig) **1**, 169 (1884).

[2] Zhe Chuan Feng, in *SiC Power Materials: Devices and Applications*, edited by R. Hull, R. M. Osgood Jr, J. Parisi, and H. Warlimont (Springer-Verlag, Berlin, 2004).

[3] H. J. Round, Electr. World **19**, 309 (1907).

[4] Yu. M. Tairov and V. F. Tsvetkov, J. Cryst. Growth **43**, 209 (1978).

[5] S. Nishino, J. A. Powell, and H. A. Will, Appl. Phys. Lett. **42**, 460 (1983).

[6] N. Kuroda, K. Shibahara, W. S. Yoo, S. Nishino, and H. Matsunami, Ext. Abstr. 19th Conf. on Solid State Devices and Materials, Tokyo, 227 (1987).

[7] H. V. Jagodzinski, Acta Cryst. **2**, 208 (1949).

[8] G. R. Fisher and P. Barnes, Phil. Mag. B **61**, 217 (1990).

[9] L. S. Ramsdell, Amer. Mineral. **32**, 64 (1947).

[10] Yoon Soo Park, in *SiC Materials and Devices*, edited by R. K. Willardson and E. R. Weber (Academic Press, USA, 1998).

[11] Landolt-Börnstein, *Numerical data and functional relationships in science and technology. New series / Landolt-Börnstein* (Springer-Verlag, Berlin, 2001), Vol. 41A1a.

[12] M. Levinshtein, S. Rumyantsev, and M. Shur, in *Handbook Series on Semi-conductor Parameters*, edited by M. Levinshtein, S. Rumyantsev, and M. Shur (Worls Scientific, Singapore, 1996), Vol. 1.

[13] T. Kimoto, T. Yamamoto, Z. Y. Chen, H. Yano, and H. Matsunami, J. Appl. Phys. **89**, 6105 (2001).

[14] D. Nakamura, I. Gunjishima, S. Yamaguchi, T. Ito, A. Okamoto, H. Kondo, S. Onda, and K. Takatori, Nature **430**, 1009 (2004).

[15] K. Ueno, R. Asai, and T. Tsuji, IEEE Electron Device Lett. **19**, 244 (1998).

[16] R. Schörner, P. Friedrichs, D. Peters, and D. Stephani, IEEE Electron Device Lett. **20**, 241 (1999).

[17] K. Ueno, R. Asai, and T. Tsuji, Mater. Sci. Eng. B **61-62**, 472 (1999).

[18] H. Yano, T. Kimoto, H. Matsunami, M. Bassler, and G. Pensl, Mater. Sci. Forum **338-342**, 1109 (2000).

[19] E. Bano, C. Banc, T. Ouisse, and S. Scharnholz, Solid-State Electron. **44**, 63 (2000).

[20] J. Spitz, M. R. Melloch, Jr. J. A. Cooper, and M. A. Capano, IEEE Electron Device Lett. **19**, 100 (1998).

[21] V. R. Vathulya and M. H. White, Solid-State Electron. **44**, 309 (2000).

[22] J. R. Williams, G. Y. Chung, C. C. Tin, K. McDonald, D. Farmer, R. K. Chanana, R. A. Weller, S. T. Pantelides, O. W. Holland, M. K. Das, and L. C. Feldman, Mater. Sci. Forum **389-393**, 967 (2002).

[23] V. V. Afanas'ev, M. Bassler, G. Pensl, and M. Schulz, Phys. Stat. Sol. (a) **162**, 321 (1997).

[24] G. Y. Chung, C. C. Tin, J. R. Williams, K. McDonald, M. Di Ventra, S. T. Pantelides, L. C. Feldman, and R. A. Weller, Appl. Phys. Lett. **76**, 1713 (2000).

[25] N. S. Saks, S. S. Mani, and A. K. Agarwal, Appl. Phys. Lett. **76**, 2250 (2000).

[26] H. Kobayashi, T. Sakurai, and M. Takahashi, Phys. Rev. B **67**, 115305 (2003).

[27] H. Yano, T. Kimoto, and H. Matsunami, Appli. Phys. Lett. **81**, 301 (2002).

[28] V. V. Afanas'ev and A. Stesmans, Appl. Phys. Lett. **69**, 2252 (1996).

[29] V. V. Afanas'ev and A. Stesmans, Phys. Rev. Lett. **78**, 2437 (1997).

[30] V. V. Afanas'ev, A. Stesmans, M. Bassler, G. Pensl, and M. J. Schulz, Appl. Phys. Lett. **76**, 336 (2000).

[31] K. McDonald, R. A. Weller, S. T. Pantelides, L. C. Feldman, G. Y. Chung, C. C. Tin, and J. R. Williams, J. Appl. Phys. **93**, 2719 (2003).

[32] P. Jamet and S. Dimitrijev, Appl. Phys. Lett. **79**, 323 (2001).

[33] P. Deák, A. Gali, Z. Hajnal, Th. Frauenheim, N. T. Son, E. Janzén, W. J. Choyke, and P. Ordejón, Mater. Sci. Forum **433-436**, 535 (2003).

[34] J. M. Knaup, P. Deák, Th. Frauenheim, A. Gali, Z. Hajnal, and W. J. Choyke, Phys. Rev. B **72**, 115323 (2005).

[35] J. M. Knaup, P. Deák, Th. Frauenheim, A. Gali, Z. Hajnal, and W. J. Choyke, Phys. Rev. B **71**, 235321 (2005).

[36] V. V. Afanas'ev and A. Stesmans, Appl. Phys. Lett. **71**, 3844 (1997).

[37] V. V. Afanas'ev, A. Stesmans, F. Ciobanu, G. Pensl, K. Y. Cheong, and S. Dimitrijev, Appl. Phys. Lett. **82**, 568 (2003).

[38] V. V. Afanas'ev, F. Ciobanu, S. Dimitrijev, G. Pensl, and A. Stesmans, J. Phys.: Condens. Matter **16**, S1839 (2004).

[39] V. V. Afanas'ev, A. Stesmans, and C. Harris, Mater. Sci. Forum **264**, 857 (1998).

[40] V. V. Afanas'ev, A. Stesmans, M. Bassler, G. Pensl, M. J. Schulz, and C. I. Harris, J. Appl. Phys. **85**, 8292 (1999).

[41] K. Fukuda, S. Suzuki, T. Tanaka, and K. Arai, Appl. Phys. Lett. **76**, 1585 (2000).

[42] K.-C. Chang, N. T. Nuhfer, L. M. Porter, and Q. Wahab, Appl. Phys. Lett. **77**, 2186 (2000).

[43] S. Wang, M. Di Ventra, S. G. Kim, and S. T. Pantelides, Phys. Rev. Lett. **86**, 5946 (2001).

[44] P. Kroll, J. Mater. Chem. **13**, 1657 (2003).

[45] A. Gali, P. Deák, P. Ordejón, N. T. Son, E. Janźen, and W. J. Choyke, Phys. Rev. B **68**, 125201 (2003).

[46] W. Lu, L. C. Feldman, Y. Song, S. Dhar, W. E. Collins, W. C. Mitchel, and J. R. Williams, Appl. Phys. Lett. **85**, 3495 (2004).

[47] K. Fukuda, W. J. Cho, K. Arai, S. Suzuki, J. Senzaki, and T. Tanaka, Appl. Phys. Lett. **77**, 866 (2000).

[48] C. Castiglioni, C. Mapelli, F. Negri, and G. Zerbi, J. Chem. Phys. **114**, 963 (2001).

[49] C. Virojanadara and L. I. Johansson, Surf. Sci. Letters **472**, L145 (2001).

[50] C. Virojanadara and L. I. Johansson, Surf. Sci. **505**, 358 (2002).

[51] E. Pippel, J. Woltersdorf, H. Ö. Ólafsson, and E. Ö. Sveinbjörnsson, J. Appl. Phys. **97**, 034302 (2005).

[52] K.-C. Chang, J. Bentley, and L. M. Porter, J. Electron. Mater. **32**, 464 (2003).

[53] K.-C. Chang, L. M. Porter, J. Bentley, C.-Y. Lu, and Jr J. Cooper, J. Appl. Phys. **95**, 8252 (2004).

[54] J. L. Cantin, H. J. von Bardeleben, Y. Shishkin, Y. Ke, R. P. Devaty, and W. J. Choyke, Phys. Rev. Lett. **92**, 015502 (2004).

[55] J. L. Cantin, H. J. von Bardeleben, Y. Ke, R. P. Devaty, and W. J. Choyke, Appl. Phys. Lett. **88**, 092108 (2006).

[56] S. Wang, S. Dhar, S.-R. Wang, A. C. Ahyi, A. Franceschetti, J. R. Williams, L. C. Feldman, and S. T. Pantelides, Phys. Rev. Lett. **98**, 026101 (2007).

[57] H. Ö. Ólafsson, E. Ö. Sveinbjörnsson, , T. E. Rudenko, I. P. Tyagulski, I. N. Osiyuk, and V. S. Lysenko, Appl. Phys. Lett. **79**, 4034 (2001).

[58] H. Ö. Ólafsson, F. Allerstam, and E. Ö. Sveinbjörnsson, Mater. Sci. Forum **389-393**, 1005 (2002).

[59] V. V. Afanas'ev and A. Stesmans, Phys. Rev. Lett. **80**, 5176 (1998).

[60] H. Li, S. Dimitrijev, H. Harrison, and D. Sweatman, Appl. Phys. Lett. **70**, 2028 (1997).

[61] P. T. Lai, S. Chakraborty, C. L. Chan, and Y. C. Cheng, Appl. Phys. Lett. **76**, 3744 (2000).

[62] P. Jamet, S. Dimitrijev, and P. Tanner, J. Appl. Phys. **90**, 5058 (2001).

[63] S. Dhar, L. C. Feldman, S. Wang, T. Isaacs-Smith, and J. R. Williams, J. Appl. Phys. **98**, 014902 (2005).

[64] J. P. Xu, P. T. Lai, C. L. Chan, B. Li, and Y. C. Cheng, IEEE Electron Device Lett. **21**, 298 (2000).

[65] G. Gudjónsson, H. Ö. Ólafsson, and E. Ö. Sveinbjörnsson, Mater. Sci. Forum **457-460**, 1425 (2004).

[66] H. Yano, F. Furumoto, T. Niwa, T. Hatayama, Y. Uraoka, and T. Fuyuki, Mater. Sci. Forum **457-460**, 1333 (2004).

[67] F. Ciobanu, G. Pensl, V. Afanas'ev, and A. Schörner, Mater. Sci. Forum **483-485**, 693 (2005); F. Ciobanu, T. Franck, G. Pensl, V. Afanas'ev, S. Shamuilia, A. Schörner, and T. Kimoto, Mater. Sci. Forum **527-529**, 991 (2006).

[68] S. Dhar, L.C. Feldman, S. Wang, T. Isaacs-Smith, and J. R. Williams, J. Appli. Phys. **98**, 014902 (2005); S. Dhar, S. Wang, A. C. Ahyi, T. Isaacs-Smith, S. T. Pantelides, J. R. Williams, and L.C. Feldman, Mater. Sci. Forum **527-529**, 949 (2006).

[69] S. T. Pantelides, S. Wang, A. Francesschetti, R. Buczko, M. Di Ventra, S. N. Rashkeev, L. Tsetseris, M. H. Evans, I. G. Batyrev, L. C. Feldman, S. Dhar, K. McDonald, R. A. Weller, R. D. Scrimpf, D. M. Fleetwood, X. J. Zhou, J. R. Williams, C. C. Tin, G. Y. Chung, T. Isaacs-Smith, S. R. wang, S. J. Pennycook, G. Duscher, K. van Benthem, and L. M. Porter, Mater. Sci. Forum **527-529**, 935 (2006).

[70] P. Deák, J. M. Knaup, T. Hornos, C. Thill, A. Gali, and T. Frauenheim, J. Phys. D: Appli. Phys. **40**, 6242 (2007).

[71] F. Allerstam, G. Gudjónsson, H. Ö. Ólafsson, E. Ö. Sveinbjörnsson, T. Rödle, and R. Jos, Mater. Sci. Forum **483-485**, 837 (2005).

[72] M. K. Das, B. A. Hull, S. Krishnaswami, F. Husna, S. Haney, A. Lelis, C. J. Scozzie, and J. D. Scofield, Mater. Sci. Forum **527-529**, 967 (2006).

[73] E. Ö. Sveinbjörnsson, G. Gudjónsson, F. Allerstam, H. Ö. Ólafsson, P.-Å. Nilsson, H. Zirath, T. Rödle, and R. Jos, Mater. Sci. Forum **527-529**, 961 (2006).

[74] E. Ö. Sveinbjörnsson, F. Allerstam, H. Ö. Ólafsson, , G. Gudjónsson, D. Dochev, T. Rödle, and R. Jos, Mater. Sci. Forum **556-557**, 487 (2007).

[75] G. Gudjónsson, H. Ö. Ólafsson, F. Allerstam, P.-Å. Nilsson, E. Ö. Sveinbjörnsson, T. Rödle, and R. Jos, Mater. Sci. Forum **483-485**, 833 (2005).

[76] B. Hornetz, M.-J. Michel, and J. Halbritter, J. Mater. Res. **9**, 3088 (1994).

[77] G. G. Jernigan, R. E. Stahlbush, and N. S. Saks, Appl. Phys. Lett. **77**, 1437 (2000).

[78] J. Deccker, K. Saarinen, H. Ólafsson, and E. Ö. Sveinbjörnsson, Appl. Phys. Lett. **82**, 2020 (2003).

[79] P. V. Sushko, S. Mukhopadhyay, A. S. Mysovsky V. B. Sulimov, A. Taga, and A. L. Schluger, J. Phys.: Condens. Matter **17**, S2115 (2005).

[80] L. A. Lipkin and J. W. Palmour, J. Electron. Mater. **76**, 1713 (1996).

[81] J. Bernhardt, J. Schardt, U. Starke, and K. Heinz, Appl. Phys. Lett. **74**, 1084 (1999).

[82] T. Shirasawa, K. Hayashi, S. Mizuno, S. Tanaka, F. Komori K. Nakatsuji, and H. Tochihara, Phys. Rev. Lett. **98**, 136105 (2007).

[83] W. Lu, P. Krüger, and J. Pollmann, Phys. Rev. B **61**, 13737 (2000).

[84] Y. Hoshino, R. Fukuyama, and Y. Kido, Phys. Rev. B **70**, 165303 (2004).

[85] C. Virojanadara and L. I. Johansson, Phys. Rev. B **71**, 195335 (2005).

[86] C. Virojanadara and Johansson L. I, J. Phys.: Condens. Matter **16**, S1783 (2004).

[87] E. L. Pollock and B. J. Alder, Physica A **102**, 1 (1980).

[88] P. Ewald, Ann. Phys., Lpz. **64**, 253 (1920).

[89] S. W. de Leeuw, J. M. Perram, and E. R. Smith, Proc. R. Soc. Lond. A **373**, 27 (1980).

[90] S. W. de Leeuw, J. M. Perram, and E. R. Smith, Proc. R. Soc. Lond. A **373**, 57 (1980).

[91] S. A. Adelman and J. D. Doll, J. Chem. Phys. **64**, 2375 (1976).

[92] H. Nyquist, Phys. Rev. **32**, 110 (1928).

[93] H. B. Callen and T. A. Welton, Phys. Rev. **83**, 34 (1951).

[94] M. P. Allen and D. J. Tildesley, *Computer simulations of liquids* (Clarendon, Oxford, 1987).

[95] D. Frenkel and B. Smit, *Understanding molecular dynamics* (Academic Press, San Diego, 2002).

[96] P. Hohenberg and W. Kohn, Phys. Rev. **136**, 864 (1964).

[97] P. Hohenberg and W. Kohn, Phys. Rev. **140**, 1133 (1965).

[98] P. A. M. Dirac, Proc. Cambridge Phil. Soc. **26**, 376 (1930).

[99] D. M. Ceperley and C. J. Alder, Phys. Rev. Lett. **45**, 566 (1980).

[100] S. J. Vosko, L. Wilk, and M. Nusair, Can. J. Phys. **58**, 1200 (1980).

[101] R. O. Jones and O. Gunnarsson, Rev. Mod. Phys. **61**, 689 (1989).

[102] K. Burke, J. P. Perdew, and M. Ernzerhof, Int. J. Quantum Chem. **61**, 287 (1997).

[103] C. Lee, D. Vanderbilt, K. Laasonen, R. Car, and M. Parrinello, Phys. Rev. B **47**, 4863 (1993).

[104] J. M. Pérez-Jordá and A. D. Becke, Chem. Phys. Lett. **233**, 134 (1995).

[105] E. J. Meijer and M. Sprik, J. Chem. Phys. **105**, 8684 (1996).

[106] J. P. Perdew, J. A. Chevary, S. H. Vosko, K. A. Jackson, M. R. Pederson, D. J. Singh, and C. Fiolhais, Phys. Rev. B **46**, 6671 (1992); Phys. Rev. B **48**, 4978 (1993).

[107] A. D. Becke, J. Chem. Phys. **96**, 2155 (1992).

[108] E. I. Proynov, E. Ruiz, A. Vela, and D. R. Salahub, Int. J. Quantum Chem. **56**, 61 (1995).

[109] B. Hammer, K. W. Jacobsen, J. K. Nørskov, Phys. Rev. Lett. **70**, 3971 (1993); B. Hammer, and M. Scheffler Phys. Rev. Lett. **74**, 3487 (1995).

[110] D. R. Hamann, Phys. Rev. Lett. **76**, 660 (1996); P. H. T. Philipsen, G. te Velde, and E. J. Baerends, Chem. Phys. Lett. **226**, 583 (1994).

[111] A. Zupan, J. P. Perdew, K. Burke, and M. Causá, Int. J. Quantum Chem. **61**, 835 (1997).

[112] V. Ozolins and M. Körling, Phys. Rev. B **48**, 18304 (1993).

[113] C. Filippi, D. J. Singh, and C. Umrigar, Phys. Rev. B **50**, 14947 (1994).

[114] J. P. Perdew, J. A. Chevary, S. H. Vosko, K. A. Jackson, M. R. Pederson, D. J. Singh, and C. Fiolhais, Phys. Rev. B **45**, 13244 (1992).

[115] J. P. Perdew, J. A. Chevary, S. H. Vosko, K. A. Jackson, M. R. Pederson, D. J. Singh, and C. Fiolhais, Phys. Rev. B **46**, 6671 (1992).

[116] J. P. Perdew, K. Burke, and M. Ernzerhof, Phys. Rev. Lett. **77**, 3865 (1996).

[117] D. L. Novikov, A. J. Freeman, N. E. Christensen, A. Svane, and C. O. Rodriguez, Phys. Rev. B **56**, 7206 (1997).

[118] D. C. Patton, D. V. Porezag, and M. R. Pederson, Phys. Rev. B **55**, 7454 (1997).

[119] B. Montanari, P. Ballone, and R. O. Jones, J. Chem. Phys. **108**, 6947 (1998).

[120] J. E. Jaffe, Z. Lin, and A. C. Hess, Phys. Rev. B **57**, 11834 (1998).

[121] Y. Zhang, W. Pan, and W. Yang, J. Chem. Phys. **107**, 7921 (1997).

[122] Y. Zhang and W. Yang, Phys. Rev. Lett. **80**, 890 (1998).

[123] A. D. Becke, J. Chem. Phys. **98**, 1372 (1993).

[124] O. Gunnarsson and B. I. Lundqvist, Phys. Rev. B **13**, 4274 (1976).

[125] A. D. Becke, J. Chem. Phys. **98**, 5648 (1993).

[126] A. D. Becke, J. Chem. Phys. **104**, 1040 (1996).

[127] M. Ernzerhof, Chem. Phys. Lett. **263**, 499 (1996).

[128] O. Gritsenko, R. van Leeuwen, and E. J. Baerends, Int. J. Quantum Chem. **61**, 231 (1997).

[129] K. Burke, M. Ernzerhof, and J. P. Perdew, Chem. Phys. Lett. **265**, 115 (1997).

[130] J. P. Perdew, M. Ernzerhof, and K. Burke, J. Chem. Phys. **105**, 9982 (1996).

[131] C. Adamo and V. Barone, Chem. Phys. Lett. **274**, 242 (1997).

[132] C. Adamo and V. Barone, J. Chem. Phys. **19**, 418 (1998).

[133] D. J. Lacks and R. G. Gordon, Phys. Rev. A **47**, 4681 (1993).

[134] T. M. Henderson, A.F. Izmaylov, G. E. Scuseria, and A. Savin, J. Chem. Phys. **127**, 221102 (2007).

[135] J. Muscat, A. Wander, and N. M. Harrison, Chem. Phys. Lett. **342**, 397 (2001).

[136] C. N. Kudin, G. E. Scuseria, and R. L. Martin, Phys. Rev. Lett. **89**, 266402 (2002).

[137] J. Heyd and G. E. Scuseria, J. Chem. Phys. **121**, 1187 (2004).

[138] J. Paier, M. Marsman, K. Hummer, G. Kresse, I. C. Gerber, and J. G. Ángyán, J. Chem. Phys. **124**, 154709 (2006).

[139] D. M. Ramo, A. L. Shluger, J. L. Gavartin, and G. Bersuker, Phys. Rev. Lett. **99**, 155504 (2007).

[140] A. Alkauskas and A. Pasquarello, Physica B **401**, 546 (2007).

[141] A. Alkauskas and A. Pasquarello, Physica B **401**, 670 (2007).

[142] P. Broqvist and A. Pasquarello, Appl. Phys. Lett. **89**, 262904 (2007).

[143] P. Broqvist and A. Pasquarello, Microelectron. Eng. **89**, 2022 (2007).

[144] J. Heyd, G. E. Scuseria, and M. Ernzerhof, J. Chem. Phys. **118**, 8207 (2003).

[145] J. Heyd and G. E. Scuseria, J. Chem. Phys. **120**, 7274 (2004).

[146] M. Ernzerhof, J. Chem. Phys. **109**, 3313 (1998).

[147] P. Pulay, Molec. Phys. **19**, 197 (1969).

[148] D. R. Hamann, M. Schlüter, and C. Chiang, Phys. Rev. B **43**, 1494 (1979).

[149] L. Kleinman and D. M. Bylander, Phys. Rev. Lett. **48**, 1425 (1982).

[150] N. Troullier and J. L. Martins, Phys. Rev. B **43**, 1993 (1991).

[151] F. Gygi and A. Baldesreschi, Phys. Rev. B **34**, 4405 (1986).

[152] CPMD v3.11.1, Copyright IBM Corp 1990-2006, Copyright MPI für Festkörperforschung Stuttgart 1997-2001.

[153] D. Marx and J. Hutter, *Ab initio molecular dynamics: Theory and Implementation*, published in: *Modern Methods and Algorithms of Quantum Chemistry*, edited by J. Grotendorst, NIC Series, Vol. 1, (John von Neumann Institute for Computing, Jülich, 2000); G. Galli and A. Pasquarello, *First-principles Molecular Dynamics* in *Computer Simulation in Chemical Physics*, edited by M. P. Allen and D. J. Tildesley (Kluwer, Dordrecht, 1993), pp. 261-313; G. Pastore, E. Smargiassi, and F. Buda, Phys. Rev. A **44**, 6334 (1991).

[154] R. Buczko, S. J. Pennycook, and S. T. Pantelides, Phys. Rev. Lett. **84**, 943 (2000).

[155] T. Todorova, A. P. Seitsonen, J. Hutter, I-Feng W. Kuo, and C. J. Mundy, J. Chem. Phys. B **110**, 3685 (2006).

[156] J. Heyd, J. E. Peralta, G. E. Scuseria, and R. L. Martin, J. Chem. Phys. **123**, 174101 (2005).

[157] J. Sarnthein, A. Pasquarello, and R. Car, Phys. Rev. Lett. **74**, 4682 (1995).

[158] B. W. H. van Beest, G. J. Kramer, and R. A. van Santen, Phys. Rev. Lett. **64**, 1955 (1990).

[159] R. Car and M. Parrinello, Phys. Rev. Lett. **55**, 2471 (1985).

[160] S. Massidda, M. Posternak, and A. Baldereschi, Phys. Rev. B **48**, 5058 (1993).

[161] C. Önneby and C. G. Pantano, J. Vac. Sci. Technol. A **15**, 1597 (1997).

[162] C. Radtke, I. J. R. Baumvol, J. Morais, and F. S. Stedile, Appl. Phys. Lett. **78**, 3601 (2001); C. Radtke, R. V. Brand ao, R. P. Pezzi, J. Morais, I. J. R. Baumvol, and F. C. Stedile, Nucl. Instrum. Meth. B **190**, 579 (2002).

[163] F. Amy, P. Soukiassian, Y.-K. Hwu, and C. Brylinski, Appl. Phys. Lett. **75**, 3360 (1999); F. Amy, H. Enriquez, P. Soukiassian, P.-F. Storino, Y. J. Chabal, A. J. Mayne, G. Dujardin, Y.-K. Hwu, and C. Brylinski, Phys. Rev. Lett. **86**,

4342 (2001); F. Amy, P. Soukiassian, Y.-K. Hwu, and C. Brylinski, Phys. Rev. B **65**, 165323 (2002).

[164] L. Simon, L. Kubler, A. Ermolieff, and T. Billon, Phys. Rev. B **60**, 5673 (1999).

[165] Y. Hoshino, T. Nishiruma, T. Yoneda, K. Ogawa, H. Namba, and Y. Kido, Surf. Sci. **234**, 505 (2002).

[166] A. Pasquarello, M. S. Hybertsen, and R. Car, Phys. Rev. Lett. **74**, 1024 (1995); Phys. Rev. B **53**, 10942 (1996); Appl. Phys. Lett. **68**, 625 (1996); Appl. Surf. Sci. **104-105**, 317 (1996).

[167] A. Bongiorno, and A. Pasquarello, Appl. Phys. Lett. **83**, 1417 (2003); A. Bongiorno, A.Pasquarello, M. S. Hybertsen, and L. C. Feldman, Phys. Rev. Lett. **90** 186101 (2003).

[168] A. Bongiorno and A. Pasquarello, Phys. Rev. B **62**, R16326 (2000).

[169] F. Giustino and A. Pasquarello, Phys. Rev. Lett. **96**, 216403 (2006).

[170] B. R. Tuttle, Phys. Rev. B **67**, 155324 (2003).

[171] F. Giustino, A. Bongiorno, and A. Pasquarello, Jpn. J. Appl. Phys. **43**, 7895 (2004); J. Phys.: Condens. Matter **17**, S2065 (2005); Appl. Phys. Lett. **86**, 192901 (2005); F. Giustino and A. Pasquarello, Surf. Sci. **586**, 183 (2005).

[172] T. Yamasaki, C. Kaneta, T. Uchiyama, T. Uda, and K. Terakura, Phys. Rev. B **63**, 115314 (2001).

[173] F. Giustino and A. Pasquarello, Phys. Rev. B **71**, 144104 (2005).

[174] For Si slabs, the band gap increase was also partially assigned to the limited k point sampling [173]. For SiC slabs, this effect is less important because of the larger SiC band gap.

[175] V. V. Afanas'ev, M. Bassler, G. Pensl, and M. J. Schulz, J. Appl. Phys. **79**, 3108 (1996).

[176] C. G. Van de Walle and R. M. Martin, Phys. Rev. B **34**, 5621 (1986).

[177] G. Makov and M. C. Payne, Phys. Rev. B **51**, 4014 (1995).

[178] A. Alkauskas, private communication.

[179] S. Ögüt, J. R. Chelikowsky, and S. G. Louie, Phys. Rev. Lett. **80**, 3162 (1998).

[180] J. P. Perdew and M. Levy, Phys. Rev. B **56**, 16021 (1997).

[181] L. A. Curtis, K. Raghavachari, and P. C. Redfern, J. Chem. Phys. **106**, 1063 (1997); L. A. Curtis, P. C. Redfern, K. Raghavachari, and J. A. Pople, J. Chem. Phys. **109**, 42 (1998).

[182] J. Tersoff and D. R. Hamann, Phys. Rev. B **31**, 805 (1985).

[183] B. Hammer, L. B. Hansen, and J. K. Norskøv, Phys. Rev. B **59**, 7413 (1999).

[184] For the STM images, we used ultrasoft pseudopotentials and energy cutoffs of 25 and 140 Ry for the wave functions and electron density, respectively. Electronic structure calculations based on ultrasoft pseudopotentials are described in A. Pasquarello, K. Laasonen , R. Car, C. Y. Lee, and D. Vanderbilt, Phys. Rev. Lett. **69**, 1982 (1992), and K. Laasonen, A. Pasquarello, R. Car, C. Y. Lee, and D. Vanderbilt, Phys. Rev. B **47**, 10142 (1993).

Acknowledgments

Curriculum vitae

Name: Fabien Devynck
Date and place of birth: 13.11.1980, Bourges (18), France
Nationality: French

Education:

- 2004-2008: Ph.D. in Physics, Swiss Federal Institute of Technology (EPFL), Lausanne, Switzerland.
  "First-principles study of defects at the SiC/SiO_2 interface through hybrid functionals"
  Advisor: Prof. A. Pasquarello.

- 2003: Master thesis in Nanomaterials, Imperial College, London, UK.
  "Electrostatic imaging at molecular resolution via Atomic Force Microscopy"
  Supervisor: Dr. S. Yaliraki

- 1998-2002: Undergraduate studies in Physical Chemistry, Université Bordeaux I, France

List of Publications:

- F. Devynck and A. Pasquarello,
  Semiconductor defects at the $4H$-SiC(0001)/SiO$_2$ interface
  Physica B - Condensed Matter **401**, 556 (2007).

- F. Devynck, F. Giustino, and A. Pasquarello,
  Atomistic model of the $4H$-(0001)SiC/SiO$_2$ interface: structural and electronic properties
  Physics of Semiconductors **893**, 307 (2007).

- F. Devynck, F. Giustino, P. Broqvist, and A. Pasquarello
  Structural and electronic properties of an abrupt $4H$-SiC(0001)/SiO$_2$ interface model: Classical molecular dynamics simulations and density functional calculations
  Physical Review B **76**, 075351 (2007).

- F. Devynck, Ž. Šljivančanin, and A. Pasquarello,
  Electronic properties of an epitaxial silicon oxynitride layer on a $6H$-SiC(0001) surface: A first-principles investigation
  Applied Physics Letters **91**, 061930 (2007).

- F. Devynck, F. Giustino, and A. Pasquarello,
  Abrupt model interface for the $4H$(0001)-SiC/SiO$_2$ interface
  Microelectronic Engineering **80**, 38 (2005).